A Measurement of the Radiation Environment Around Prompt J/ψ Events at ATLAS

by

David Bjergaard

Department of Physics
Duke University

Date: _____

Approved:

_____
Ayana T Arce, Supervisor

_____
Tom C. Mehen

_____
Mark C. Kruse

_____
Ashutosh V. Kotwal

_____
Glenn Edwards

Dissertation submitted in partial fulfillment of the requirements for the degree of
Doctor of Philosophy in the Department of Physics
in the Graduate School of Duke University
2017

Abstract

A Measurement of the Radiation Environment Around Prompt J/ψ Events at ATLAS

by

David Bjergaard

Department of Physics
Duke University

Date: _____

Approved:

_____
Ayana T Arce, Supervisor

_____
Tom C. Mehen

_____
Mark C. Kruse

_____
Ashutosh V. Kotwal

_____
Glenn Edwards

An abstract of a dissertation submitted in partial fulfillment of the requirements for the degree of Doctor of Philosophy in the Department of Physics in the Graduate School of Duke University
2017

Abstract

The J/ψ particle has been the source of much research since its discovery in 1974. It provides an important probe of quantum chromodynamics and has lead to many important insights into the interactions of quarks and gluons in bound states. The rate of production was found to be much higher than expected at hadron colliding experiments. Non-relativistic quantum chromodynamics was developed in order to address these issues. This theory predicts a strong spin-alignment not observed in data. All previous measurements of J/ψ production have overlooked the hadronic environment of the J/ψ. This work is the first exploration of the radiation surrounding J/ψ events measured at ATLAS at $\sqrt{s} = 8$ TeV. It represents the first measurement of the separation between the J/ψ and a matched jet and the second measurement of the momentum fraction shared between the jet and the J/ψ. These variables probe the radiation environment around the J/ψ, and provide a new ways to understand quarkonia production.

To my wife.

Contents

List of Tables

List of Figures

Acronyms

ATLAS A Toroidal LHC AparatuS. 5, 28

CSC Cathode Strip Chamber. vii, viii, 42–44, 46, 48, 49

ECAL Electromagnetic Calorimeter. vii, 38–42

EF Event Filter. 54

FJF Fragmenting Jet Function. 4, 92

HCAL Hadronic Calorimeter. vii, 38–40, 42

HEC Hadronic Endcap Calorimeter. 40, 41

LHC Large Hadron Collider. 5, 24–28, 52, 82

MDT Monitored Drift Tube. vii, 42, 43, 45–47

ML Maximum Likelihood. 66–68

NRQCD Non-relativistic Quantum Chromodynamics. 3, 15, 92

PDF Probability Distribution Function. 66–71, 78

QCD Quantum Chromodynamics. vi, 2–4, 6–11, 13–16, 19, 20, 22, 60

QED Quantum Electrodynamics. 8, 10, 13

RoI Region of Interest. 53, 54

RPC Resistive Plate Chamber. viii, 42, 46, 47, 50, 51, 53

SCT Silicon Strip Tracker. v–vii, 30, 32–37, 64

TGC Thin Gap Chamber. viii, 42, 46–48, 50, 52, 53

TRT Transition Radiation Tracker. vi–viii, 30, 32, 35, 36, 38, 43, 48, 50, 51, 54

Acknowledgements

This work is the realization of a goal that I've had since I was a sophomore in high school. My love of science started much earlier with a set of encyclopedia's for children given to me by my grandmother, Alice Ganksop. Without her and my parent's (Martin and Lisa Bjergaard) support, my love of science wouldn't have grown to give me the dedication required to complete a PhD. As a high school student, two educators stand out as having significant influence on my path to a PhD in physics: Don Haufschild, my physics teacher and David McDowell, my pre-calculus teacher. As an undergraduate, I was significantly influenced by Petar Maksimovic and Salvatore Rappoccio, both of which formed the foundation of research skills that I've continued to use and hone throughout my PhD. The constant support of my wife, Swarnali Sengupta Bjergaard (also a PhD student) has allowed me to grow in ways I did not know were possible. Both of our parents have given us countless hours of guidance in managing our work-life balance as well as problem solving many problems related to research and otherwise. Finally, Sean and Heather Finch have been a constant source of social support as we finish our degrees. They are always there for us when we want to decompress after a tough week, and understand the hard work it takes to complete a PhD.

Professionally I have benefited from many of my peers as well as people who have mentored me to become a better physicist. Chris Pollard and Ben Cerio were especially helpful in the early years of my PhD for helping me solve problems with

analysis. Ben always kept me on my toes and helped me see the possibility of moving beyond an academic career path. My sub-group conveners, Bruce Yabsly and Andrew Chisholm, in the B and Light States Group have constantly challenged me to approach my work rigorously and to communicate clearly. Every one of their suggestions has made my analysis stronger. I have become a physicist under the mentoring and guidance of Ayana Arce. She has encouraged me to follow non-standard research paths and think independently even prior to accepting my position at Duke. She encouraged me to teach and mentor students and provided me with ample professional development. She has always supported my choices and helped me make the tough decision to explore a career outside of academia. I owe everyone above a large drink of their choice, and am happy to provide it, you need only ask.

Preface

The following document is a comprehensive description of a measurement I (David Bjergaard) have performed in order to better understand J/ψ production in proton collisions at the LHC. It does not represent the sum total of the research and teaching experiences I have completed and contributed to in the years spanning my Graduate School education. Below is a brief summary of my teaching experiences followed by my research contributions not summarized in this thesis.

During my first two years in the physics graduate program, I taught introductory labs in mechanics and electricity and magnetism (E&M). I also served as the grading TA for advanced E&M where I provided weekly solutions to the homework problems. I have privately tutored students in mechanics and E&M for the past four years. In order to further my teaching and presentation skills, I enrolled in the Certificate in College Teaching (CCT) program. As part of that program, I served as a recitation instructor for "Introduction to Physics for Engineers." These experiences have given me the tools to learn how to teach.

Beginning chronologically, I started work at ATLAS by contributing analysis routines for a suite of substructure variables and their performance in Monte Carlo generators. The result of this work was a report presented at the BOOST2012 conference in Valencia [11]. The work has been cited 89 times at the time of this writing and provides an important guidepost for Monte Carlo generator authors, as well as experimental practitioners looking to apply jet substructure techniques to

their analysis.

The next major research contribution I made was to my qualification task for ATLAS. I restructured the job scheduling software that simulates pileup effects. These effects scale non-linearly with the amount of pileup being simulated and as a result, some jobs finished quickly and others finished slowly. My contribution was a scheme that ensured that the jobs finished at roughly the same time. I improved the uniformity of the time to complete the jobs by nearly two orders of magnitude.

My third research project at ATLAS was the work that allowed me to successfully complete my preliminary exam. This was the establishment of jet charge as a viable jet substructure variable. The work was extended and expanded by my ATLAS colleagues to include a measurement of jet charge in dijet events [3]. This measurement provided an important check on our understanding of how parton distribution functions contribute to QCD processes at the energy scale of the LHC.

The remaining original contributions that I have made stem from or are related to the work presented in this thesis. In order to prove the viability of this work, I performed a survey of substructure variables using RIVET, a software framework for studying and tuning the performance of Monte Carlo generators. This work lead to the identification of a suite of substructure variables which could discriminate between two J/ψ production mechanisms.

The application of jet substructure techniques to quarkonium production is completely novel and required the solution of a number of problems. The most important were the careful handling of the detector subsystems because of their differing methods of reconstructing particles. This lead to the choice to use jets reconstructed from charged particles only (i.e. track based jets). The use of these jets was established by the jet charge measurement [3]. In addition to the detector response, an unsolved problem is how the spin-alignment of the J/ψ and the reconstructed muons should

be handled. In order to avoid this issue, the jets were again modified to include the J/ψ candidate.

My final contribution to the field of high energy physics was a complete implementation of J/ψ production in Sherpa, another general purpose Monte Carlo generator. This work was performed as part of an MCnet fellowship at Durham University in the UK. The work is largely finished but remains unpublished due to the need to validate the simulation against Pythia's description of J/ψ production as well as existing measurements from ATLAS and CMS. If this work can be published, it will add an additional generator level description of J/ψ production and may help further our understanding of how these particles are produced in hadron collisions.

1

Introduction

1.1 A brief history

The history of particle physics spans over a century of experimental and theoretical development that has lead to some of the deepest insights into nature. The starting point for this work began during the post-war period of the early 1950s. A series of bubble chamber experiments led to the discovery of the Λ, Ξ and Σ baryons[1]. This coupled with the discoveries of the K, π and η mesons[2] lead to the proposal of the "eightfold way" [35]. The guiding principal of the eightfold way is to use the structure of a proposed $SU(3) \times SU(3)$ flavor symmetry to explain the mesons and baryons known to date and to make strong predictions about new states that should be observed [35]. This organization of the particles hints at the existence of fundamental particles called *quarks*.

While the eightfold way provided an organizational scheme and robust predictions of the relationships between the members of the baryon octet, experimental evidence for the existence of quarks came later. In 1971, Feynman published what is now

[1] Baryons are bound states of three quarks. The name is derived from the greek word "heavy" or "barus".

[2] Mesons are bound states of a quark and an anti-quark. The name is derived from the greek word "intermediate" or "mesos".

known as the parton[3] model of the hadron [33]. This model treated the components of the hadron as fundamental particles with physical properties. This is in contrast to the quark model of the eightfold way which did not describe quarks as physical particles. The parton model described many experimental results to a reasonable degree. There were some issues, namely a "fudge factor" to scale the numerical calculations close enough to their experimental values to be compared [33].

The eightfold way and the parton model provided two complementary views of the structure of the hadron. The eightfold way provided a computational framework that was successful in describing many observed patterns in the quantum numbers of the known hadrons. The parton model provided a physical picture of the structure of the hadron. Neither model provided a precise description of the underlying dynamics of the strong interaction.

In November 1973, Wilczek and Gross published their seminal paper on asymptotically free gauge theories[4] [38]. This paper laid the groundwork for what would become quantum chromodynamics (QCD) the theory underpinning the subject of this thesis. A year later in 1974 the discovery of a new particle was announced independently by a group at Brookhaven National Lab (named the J) and a group at the Stanford Linear Accelerator (named the ψ) [14][15]. The joint discovery of the J/ψ lead to what is known colloquially as the "November revolution." The new particle provided a new piece of experimental evidence that confirmed the picture of quarks and helped to unravel the mysteries of the strong interaction.

We now understand that hadrons are made up of quarks and gluons (partons in Feynman's parlance). In addition, the bound state of a heavy quark and anti-quark of the same flavor are referred to as quarkonium. This name is reminiscent of

[3] Parton so called for being a "part" of the hadron. Also rumored to be named after Dolly Parton, the country singer [22].

[4] H. David Politzer published a similar result in May of that year [51], the three authors shared the Nobel Prize in Physics in 2004.

positronium, the electromagnetically bound state of a positron and electron. Many of the salient features of the quarkonium mass spectrum can be understood with non-relativistic quantum mechanics and empirical models of the QCD potential. Even with this deep understanding of nature's fundamental interactions, the J/ψ particle continues to perplex and confuse our understanding of QCD. In 1992, the CDF collaboration at the Tevatron reported the first measurement of direct J/ψ and ψ(2S) production. They found the rate of production to be an order of magnitude more than the expectation from theory [8]. Two years later, Bodwin, Braaten and Lepage worked out many of the details of quarkonium production in QCD using effective field theory [21].

In 1997, the Tevatron updated its observation of the ψ system with more data. It reported the differential cross section of the J/ψ to be much higher than anticipated by the leading order theory calculation for singlet production [7]. The details worked out by Bodwin et al positioned the theory community to quickly calculate the needed contributions from the non-relativistic expansion of QCD (NRQCD) in order to describe the data [20].

The extra NRQCD components that describe the observed transverse momentum spectrum predicted that the spin alignment between the J/ψ and the decaying muons should be strongly polarized. Subsequent measurements of the polarization at CDF found no evidence of polarized spin-alignment in the J/ψ system [9]. This problem has been dubbed the "polarization puzzle" in literature and has no satisfying explanation nearly two decades after its first observation.

The production of charm quark pairs which transition to the J/ψ state probes two complementary energy scales. The origination of the pair happens during the primary interaction of two partons. This is a high energy interaction and can be calculated using perturbation theory. After the pair of quarks is produced, their relative motion determines the dynamics of the bound state. This is at a much lower energy scale

and is non-perturbative. Handling these two scales is the major theoretical challenge to calculating a quantitative cross section for quarkonium production.

While there has been much theoretical work to understand J/ψ production, experimental approaches have mainly focused on measuring the differential production cross section of isolated, directly produced J/ψ particles. Little to no attention has been paid to the hadronic environment surrounding the charmonium system. If the charmonium is produced in a color singlet state, the surrounding radiation should be less than a $c\overline{c}$ pair in a color octet state.

A useful phenomenological model employed by Pythia[5] is to consider the charmonium system as a color-charged particle which can couple to gluons using rules of QCD [58]. As this particle propagates it emits collinear gluon radiation according to a splitting function for the process $q \to qg$. When the composite particle falls below a certain threshold, it transitions to a color singlet J/ψ hadron and emits the remaining color charge as a soft gluon which is incorporated into the underlying event. This is in contrast to color singlet production which has the J/ψ produced directly and no net color charge.

An alternative view of charmonium production is the production of the charm quark pair during the fragmentation of partons into individual hadrons. In the fragmenting jet[6] function (FJF) framework [52], the total cross section is a product of the short distance partonic cross section with universal fragmentation functions which determine the evolution of individual partons to hadrons.

The FJF framework differs from the Pythia model in how it treats the distribution of radiation around the charmonium system. In the FJF approach, a high energy gluon splits according to a splitting function for $g \to gg$, which is very different from Pythia's model which allows the charmonium system to radiate according to a

[5] A generic Monte Carlo simulation program used in High Energy Physics.

[6] A jet is a collimated spray of particles resulting from high energy QCD processes.

splitting function for $q \to qg$. This leads to fundamentally different distributions of momentum between the surrounding radiation and the charmonium system [17].

The following is a birds-eye view of the remainder of the thesis. Chapter 2 presents an overview of Quantum Chromodynamics, and the phenomena relevant for this work. Following that Chapter 3 describes the LHC and the ATLAS detector in detail. After describing the detecting apparatus, the methods of reconstructing jets and J/ψ candidates are described in Chapter 4. With a firm grasp of the theory and physical measurement of the particles, the next step is a description of the data analysis methods used in Chapter 5. In Chapter 6 the selection criteria, systematic errors, and final results are presented. A discussion of consequences and future work follows in Chapter 7.

2

Theory

2.1 Quantum Chromodynamics

Quantum chromodynamics describes the interactions between quarks and gluons. It is one of the fundamental pieces of the Standard Model of Physics, and has provided fertile ground for experimental and theoretical work. The interactions of QCD are determined by the SU(3) symmetry group. Under this symmetry, quarks have a color charge ($a = 1, 2, 3$). While quarks carry a color charge, they must form color neutral particles. Therefore, it is useful to assign the colors red, green, and blue to the color index in order to provide intuition for which states are allowed. Quarks paired with color conjugated quarks (green with anti-green, red with anti-red etc) form the mesons. Triplet pairs of quarks with an anti-symmetric combination of red, green, and blue form color neutral baryons. Other more exotic combinations are allowed but they must follow the constraint that the state is color neutral.

2.1.1 Quark Flavor

In addition to carrying color charge, quarks carry a flavor. The Standard Model consists of three generations of quarks. Each generation consists of a flavor doublet

with charge 2/3 and charge -1/3. Quarks with charge 2/3(-1/3) are referred to as up(down)-type quarks. In each generation, the mass of the quarks is successively larger. In the first generation, the up and down quarks are a few MeV. The strange and charm quark masses differ by a factor of 10. The strange quark mass is approximately 100 MeV, while the charm quark mass is near 1 GeV. In the third and final generation, the bottom quark is 4 GeV, and the top quark is forty times larger at 173 GeV [47]. The quantum numbers of the individual quarks determine the properties of the composite baryons and mesons.

2.1.2 Lagrangian

The formulation of a quantum theory of quark interactions requires a Lagrangian which contains interaction terms which invariant under the SU(3) symmetry group. The following summarizes the results in chapter 1 of "QCD and Collider Physics" [30], for further details the reader is referred to that text.

In order to derive a quantum theory, begin by writing the QCD Lagrangian in terms of a classical field plus a gauge fixing term, and a ghost term:

$$\mathcal{L}_{\mathrm{QCD}} = \mathcal{L}_{\mathrm{Classical}} + \mathcal{L}_{\mathrm{Gauge}} + \mathcal{L}_{\mathrm{Ghost}}.$$

In natural units ($\hbar = c = 1$), the classical field Lagrangian is

$$\mathcal{L}_{\mathrm{Classical}} = -\frac{1}{4} F^A_{\alpha\beta} F^{\alpha\beta}_A + \sum_{\text{flavors}} \overline{q}_a (i \not{D} - m)_{ab} q_b. \tag{2.1}$$

Here $\not{D} \equiv \gamma_\mu D^\mu$, and $F^A_{\alpha\beta}$ is the gluon field strength tensor,

$$F^A_{\alpha\beta} = \partial_\alpha \mathcal{A}^A_\beta - \partial_\beta \mathcal{A}^A_\alpha - g f^{ABC} \mathcal{A}^B_\alpha \mathcal{A}^C_\beta. \tag{2.2}$$

The color indices A, B, C run over the eight generators of the SU(3) group. The constant g represents the coupling strength, and the constants f^{ABC} are the structure constants of SU(3). It is this term which distinguishes QCD from quantum

electrodynamics (QED). In order to derive the Feynman rules for QCD, the path integral of the action must be evaluated. In the standard formulation of the action, the resulting integral is badly divergent because of the gauge invariance of the theory [48] [1]. Following the Faddeev-Popov method of gauge fixing used in [30] the following two terms are added to the Lagrangian:

$$\mathcal{L}_{\text{Gauge}} = -\frac{1}{2\lambda}(\partial^\alpha \mathcal{A}^A_\alpha)^2 \tag{2.3}$$

$$\mathcal{L}_{\text{Ghost}} = \partial_\alpha \eta^{A\dagger}(D^\alpha_{AB}\eta^B) \tag{2.4}$$

These terms serve to constrain the integral over the action to physical configurations exactly once [48].

2.1.3 Feyman Rules

The Feynman rules for QCD can be determined from the Lagrangian by finding the action ($S = \int \mathcal{L} d^4x$)and writing it in terms of a free field Lagrangian S_0 and an interacting term S_I,

$$S = S_0 + S_I.$$

Further by identifying $\partial^\alpha = -ip^\alpha$ as the momentum it is possible to write down the two point function for the quarks and gluons. This results in the Feynman rules shown in Figure 2.1.

Combined, these rules allow the creation of any relativistic quark interactions allowed by the theory of QCD. There are two aspects of QCD which distinguish it from QED.

The first is the running of the coupling constant, α_S. In QED, the coupling constant is higher at high energies. This running of the coupling constant can be understood by examining the state of the vacuum around the electric charge. At high energies, and short distances, there is less screening of the true charge of the

[1] See 9.4 Quantization of the Electromagnetic Field.

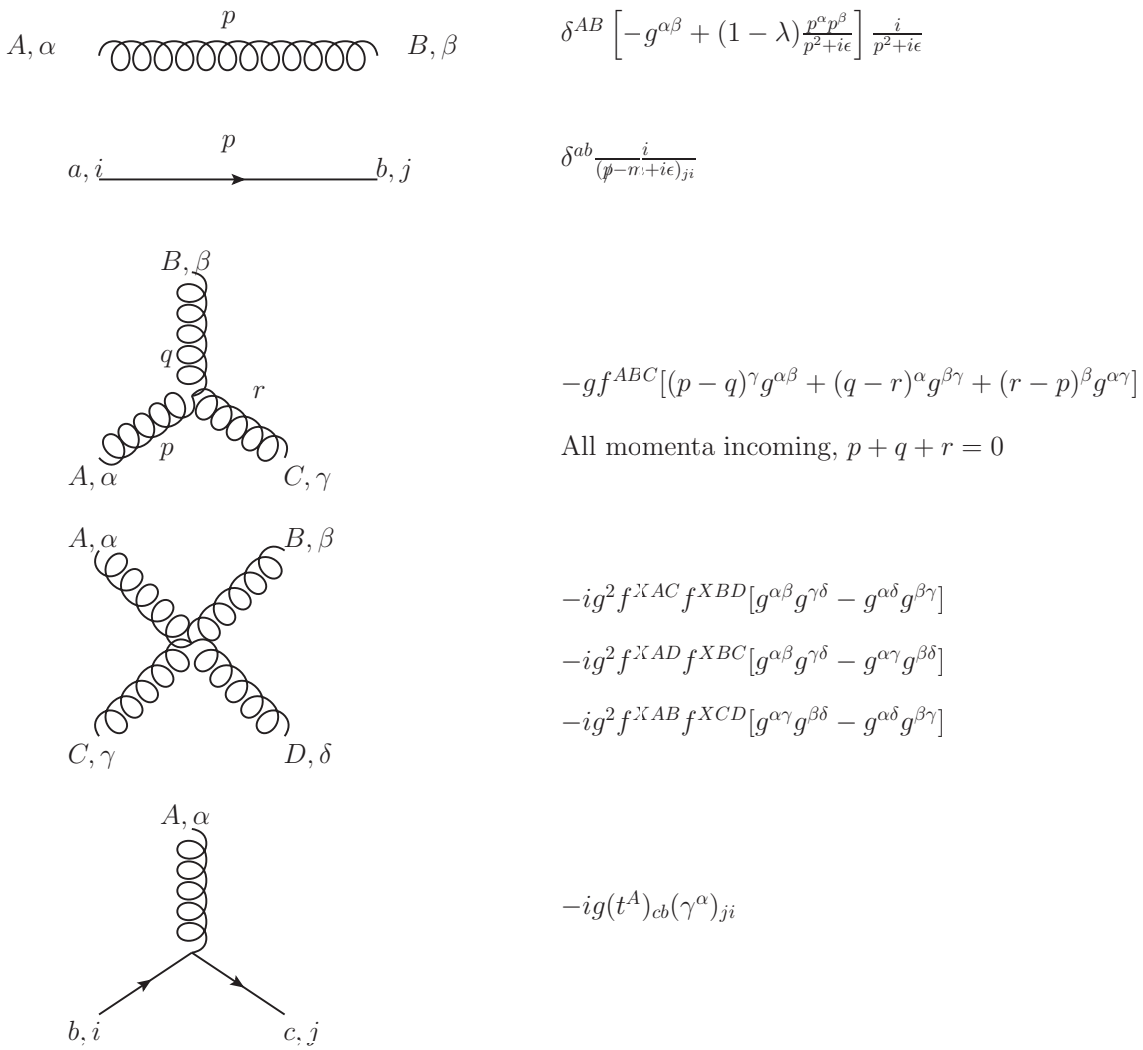

FIGURE 2.1: Feynman rules for QCD. The ghost terms have been excluded, see [30] for more details.

electron due to vacuum polarization. This polarization arises due to dipole pairs of virtual electrons and positrons which screen the charge of the electron. This leads to a coupling constant which is larger than at low energies. In QCD, the coupling constant decreases at high energy. This phenomenon is known as asymptotic freedom. At very high energies, the coupling between quarks becomes so low that they become free particles. It is difficult to understand this from the vacuum of QCD, but it is possible to make analogies to the paramagnetic properties of the vacuum [30].

The second feature is the self-interaction of the gluon. In QED, the mediating photon has no electric charge and thus does not couple to itself. In QCD, the gluon carries color charge. This means that the field doesn't spread uniformly out from the quark. Instead, it forms tube-like structures. At some point, the potential energy stored in the self-interacting gluon tubes becomes so high that it is energetically favorable to create a quark anti-quark pair from the vacuum rather than to increase the distance between two quarks further. This property of QCD is referred to as confinement. The energy scale that determines which regime in which QCD is confining versus being asymptotically free is the cutoff energy scale $\Lambda_{\mathrm{QCD}} \simeq 450$ MeV.

2.2 Quarkonium

The bound states and their properties are important to any theory of interactions. In QCD, bound states consist of mesons and baryons in accordance with the rules outlined in Section 2.1.3. Quarkonium have a number of unique properties that make it an ideal system to study properties of QCD. The bound state consists of a quark and its charge-conjugate. This provides a degree of symmetry not present in other meson systems. In heavy quarkonium systems (charmonium and bottomonium), the mass scale is high enough that perturbation theory can provide useful answers relative to the cutoff energy scale Λ_{QCD}. The strength of the coupling strength of QCD in the charmonium system is $\alpha_s(m_c) \approx 0.24$ [21]. This is large enough that the perturbation series converges more slowly than one would hope. The higher mass of the bottom quark allows the bottomonium system a faster rate of convergence. At the bottom mass scale, $\alpha_s(m_b) \approx 0.18$ [21].

Before examining the consequences of a larger α_s in the charmonium system, it is useful to reproduce as much of the charmonium spectrum as possible using quantum mechanics. An important aspect of quarkonium production at high energies in hadronic collisions is the interplay of multiple energy scales. At very high energies,

direct production is predicted to be dominated by the fragmentation of gluons into pairs of charm quarks. The gluon recoils from a primary interaction with a gluon or quark in the proton-proton collision. The energy scale which determines the production of the quark pair is the mass of the heavy quark M.

In the rest frame of the quarkonia's constituent quarks, the relative velocity (v) of the quarks is the important scale. This means their relative momentum (Mv) is important for the dynamics of the quarkonium's propagation and subsequent decay. The final quantity which determines the dynamics of the system is the kinetic energy (Mv^2) of the quarks. The kinetic energy determines the size of the radial excitations in the system [21]. It is assumed that these scales are well separated in the sense that $(Mv^2)^2 << (Mv)^2 << M^2$ [21].

2.2.1 Positronium System

A treatment of the positronium system can be found in any undergraduate treatment of bound states allowed by the Coulomb potential [62] [37]. A brief review of the important results is presented. The content of this section follows that of [30] and uses a notation that makes the analogies between the Coulomb potential and the QCD potential manifest. The existence of a solution is due to the spherical symmetry of the Coulomb potential. This allows the system to be solved by separation of variables and reduces the degrees of freedom to finding the one-dimensional bound states due to the Coulomb potential,

$$U(r) = -\alpha/r.$$

Here α is the dimensionless fine structure constant, and takes a value of $1/137$. The wavefunction is then written as

$$\psi(r, \theta, \phi) = R_{l,n}(r) Y_l^m(\theta, \phi), \tag{2.5}$$

here $R_{l,n}(r)$ is the radial solution, and $Y_l^m(\theta, \phi)$ are the spherical harmonic functions. The spherical harmonics Y_l^m arise from requiring angular momentum conservation. The radial functions are determined by finding the solutions to the time-independent Shroedinger equation. The energy eigenvalues are the well known Bohr energy levels,

$$E_n = -\frac{\mu\alpha^2}{2n^2}. \tag{2.6}$$

Here μ is the reduced mass of the system[2]. The characteristic length scale of the system is the Bohr radius,

$$a_0 = \frac{1}{\mu\alpha}. \tag{2.7}$$

The ground state wave function is $(n = 1, l = 0, m = 0)$ [62]:

$$\psi_{100}(r, \theta, \phi) = \frac{1}{\sqrt{\pi a_0^3}} e^{-r/a_0}. \tag{2.8}$$

The first radial excited state is $(n = 2, l = 1, m = 0)$ [62]:

$$\psi_{210}(r, \theta, \phi) = \frac{1}{4\sqrt{2\pi a_0^3}} \frac{r}{a_0} e^{-r/(2a_0)} \cos\theta. \tag{2.9}$$

These two states are important because they correspond to the first two excitations in the charmonium spectrum. At this point it is useful to introduce the spectroscopic notation used in quarkonia literature. The notation follows that of atomic spectroscopy: $^{2S+1}L_J$. Here S is the total spin of the system, L is the orbital quantum number, and J is total angular momentum. In the case of positronium, and quarkonium, the constituent particles are spin-1/2. Therefore when they are combined S can take the values of 0 or 1. The orbital angular quantum number L follows the time-honored notation where $L = 0, 1, 2, 3, \ldots$ corresponds to the letters $S, P, D, F, \ldots$. Finally, J takes the values $J = |L - S|, \ldots, L + S$.

[2] $\mu \equiv \frac{m_1 m_2}{m_1 + m_2}$, in the case of positronium this is $m_e/2$.

Up to this point, the positronium system and the quarkonium system have been treated as interchangeable. In fact, if gluons did not self-interact, the QED potential and the QCD potential would be the same modulo coupling constants and a numerical factor for color. This similarity suggests that using the hydrogen-like wavefunctions as a basis and applying perturbation theory may prove fruitful.

2.2.2 Potential Models of QCD

It is not an accident that the potential model of QCD works well to describe the distribution of bound states observed in quarkonium systems. First, the gluon interaction times are much shorter than the movement time scale of the quarks. This is due to the assumption that the kinetic energy, Mv^2 is much smaller than the momentum of the quarks, Mv [21]. This means that treating the quarks as though they exist in an instantaneous potential is a good approximation. The second reason potential models are successful is the fact that the probability of another gluon existing in the bound state is small [21].

Using the Coulomb eigenfunctions as a set of basis states and applying a perturbative potential provides a good description of the quarkonium spectrum. The perturbation used is due to the self-interaction of the gluons,

$$V(r) = Kr,$$

here K is the "string constant". This term combined with the Coulomb-like potential,

$$U(r) = -\frac{4}{3}\frac{\alpha_s}{r},$$

completes the model. The perturbation is confining at large distances and presents a constant force. The string analogy is apt, as the tension in a string is constant. When the force applied exceeds the tensile strength of the string, the string snaps. This analogy suggests the string model of fragmentation in which the gluon "strings" snap and quark-anti-quark pairs form at the ends of the strings.

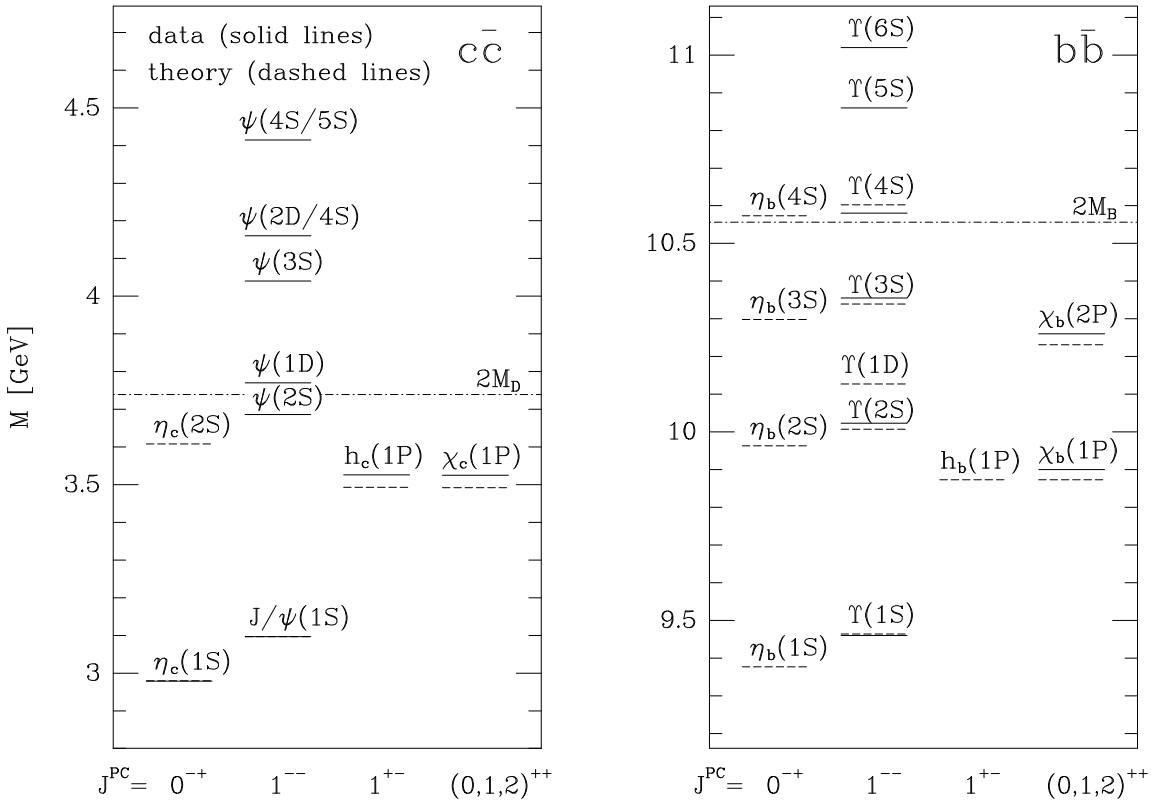

FIGURE 2.2: Spectrum of charmonium and bottomonium bound states compared to potential theory [30].

Figure 2.2 shows the result of applying a more sophisticated potential model as a perturbation on the Coulomb-like eigenfunctions. This model has the asymptotic features of the string model and describes the data well [30]. The dashed lines are the theory prediction and the solid lines are the data. The bottomonium spectrum is better described because the mass is higher, and hence the coupling constant is weaker making the assumptions behind the potential model stronger.

2.3 Non-relativistic QCD

While the potential model of QCD bound states does a good job of capturing the features of the spectrum it is not a complete description. Figure 2.2 shows some disagreement in the numerical values for the mass eigenstates. Further, the potential

model offers no way of calculating the differential cross section for production. This can be done using perturbation theory with the relativistic QCD Lagrangian. The leading order cross sections for J/ψ production were calculated in the early 80s [16]. After the measurement of the J/ψ and ψ(2S) by the Tevatron in the early 90s, the disparity between the leading order prediction and the measured data was large. This lead to the exploration of effective field theory descriptions of QCD in an attempt to bridge the gap between the non-perturbative parts of quarkonia processes which are difficult to calculate and the parts of quarkonia production amenable to perturbation theory [21].

2.3.1 Lagrangian

Rather than take an explicit expansion of the QCD Lagrangian (equation 2.1), it is informative to build a Lagrangian which is equivalent to the fully relativistic version. In this case recall that the non-relativistic expansion for the energy of a particle is the classical kinetic energy,

$$E = \sqrt{M^2 + p^2} \simeq M + \frac{p^2}{2M}. \tag{2.10}$$

The separation of short distance interactions of the light quarks and the long distance interactions of the heavy quarks suggest the following terms in the NRQCD Lagrangian [21]:

$$\mathcal{L}_{\text{NRQCD}} = \mathcal{L}_{\text{light}} + \mathcal{L}_{\text{heavy}} + \delta\mathcal{L} \tag{2.11}$$

The light quarks are expected to be adequately described by the QCD Lagrangian, and so those terms are retained

$$\mathcal{L}_{\text{light}} = -\frac{1}{2}F^A_{\alpha\beta}F_A^{\alpha\beta} + \sum_{\text{light flavors}} \bar{q}_a(i\not{D} - m)_{ab}q_b. \tag{2.12}$$

The heavy quarks are explicitly inserted using the non-relativistic expansion of the gauge-covariant derivative,

$$i\not{D} - m \simeq iD_t + \frac{\mathbf{D}^2}{2M}. \tag{2.13}$$

This gives

$$\mathcal{L}_{\text{heavy}} = \psi^\dagger \left(iD_t + \frac{\mathbf{D}^2}{2M} \right) \psi + \chi^\dagger \left(iD_t - \frac{\mathbf{D}^2}{2M} \right) \chi \tag{2.14}$$

where the color and spin indices have now been supressed and ψ is the Pauli spinor field responsible for annihilating a heavy quark. Conversely χ is the Pauli spinor field for creating a heavy anti-quark. The terms D_t and $\mathbf{D}$ are the space-time components of the gauge covariant derivative D^μ.

These two terms together describe QCD coupled with a Schrödinger theory for the heavy quarks [21]. Since the Schrödinger terms were added as a non-relativistic expansion of the gauge covariant derivative additional terms in the expansion must be included in order to fully describe the relativistic effects of QCD. These terms are explained in detail in [21] and are contained in the $\delta\mathcal{L}$ term above.

Organizing the Lagrangian in this way allows cross section formulas to be written as a dual expansion in the relative velocities of the heavy quarks and the QCD coupling constant α_s. This gives insight into which effects dominate at what scale in the short and long distance interactions.

2.3.2 Factorization Theorem

Because this formulation of the Lagrangian makes the Schrödinger states explicit, the quarkonium state can be interpreted as a sum of all possible Fock state configurations.

This can be written as [30],

$$
\begin{aligned}
|\psi_Q\rangle = & O(1)|Q\overline{Q}[^3S_1^{(1)}]\rangle + O(v)|Q\overline{Q}[^3P_J^{(8)}]g\rangle \\
& + O(v^2)|Q\overline{Q}[^1S_0^{(8)}]g\rangle + O(v^2)|Q\overline{Q}[^3S_1^{(1,8)}]gg\rangle \\
& + O(v^2)|Q\overline{Q}[^3D_J^{(1,8)}]gg\rangle + \ldots \\
& ,
\end{aligned}
\tag{2.15}
$$

here ψ_Q is the quarkonium bound state. The angular momentum quantum numbers of the Fock state are given in standard spectroscopic notation:[3] ${}^{2S+1}L_J^{(1,8)}$ with an additional index to indicate singlet (1) or octet (8) color states. In this notation, S is the spin of the $Q\bar{Q}$ pair, L is the orbital quantum number and J is the total angular momentum. This formula also makes explicit the relative probability of finding a gluon in a $Q\overline{Q}$ state, which was one of the conditions necessary for the potential model of quarkonium.

The leading order term corresponds to the wavefunction from the Schrödinger picture. Higher order terms correspond to Fock states which provide a soft gluon. The presence of this gluon in the state allows the $Q\bar{Q}$ pair to be in a color octet state. The inclusion of these terms in the expression for the overall cross section provides important contributions to the production of quarkonia in hadronic collisions.

The explicit formulation for the partonic cross section can be written as

$$
\frac{d\sigma}{d\hat{t}}(ab \to Q\overline{Q}[n]c \to \psi_Q) = \frac{1}{16\pi\hat{s}^2}\overline{\sum}\left|\mathcal{A}(ab \to Q\overline{Q}[n]c)_{\text{short}}\right|^2 \langle 0|O_{8,1}^{\psi_Q}(n)|0\rangle \tag{2.16}
$$

here a, b and c represent initial and final state partons, n is shorthand for the spectroscopic term symbol introduced above, and ψ_Q is the final state quarkonium. The sum is understood to be the average over initial spin and color states of the scattering

[3] In spectroscopy this is referred to as a term symbol.

amplitudes[4] and the $\langle 0|O_{8,1}^{\psi_Q}(n)|0\rangle$ term (abbreviated as $\mathcal{O}_{8,1}^{H}(n)$) is the long distance matrix element (LDME).

Equation 2.16 explicitly separates the energy scales involved in the production. Figure 2.3 shows a pictorial representation of this factorization. The short distance amplitude is calculated by evaluating the relevant Feynman diagrams required to produce a $Q\overline{Q}$ pair with quantum numbers n. The LDME (represented by the gray blob) on the other hand represents the low energy, non-perturbative part of the calculation.

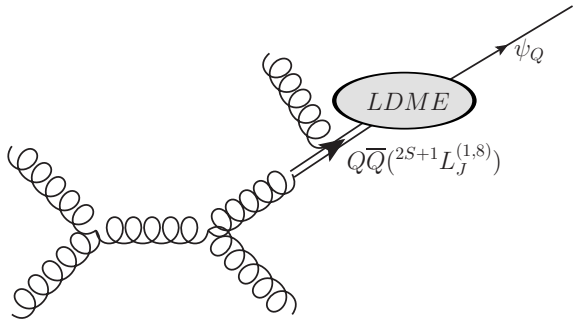

FIGURE 2.3: Schematic representation of production of quarkonium in NRQCD, $a, b, c = g$ as in equation 2.16.

This value cannot be calculated directly and must be inferred from experimental measurements. The extraction of LDMEs from globally measured data has been done many times [36] [23] [32], but the methodology is fraught with pitfalls and there is no definitive set available. The LDMEs represent a large number of degrees of freedom. Some components have different momentum dependence, and thus it is possible to re-weight them to fit the subset of data judged valid by the person fitting the parameters.

The LDME values extracted are validated using the only degree of freedom remaining in the quarkonium system: the spin alignment between the quarkonium and the measured decay products. Historically the disagreement between the measured

[4] The square of the amplitude is proportional to the probability of a process occuring.

spin-alignment and the amount required by the extracted LDMEs has been referred to as the "polarization puzzle[5]." There have been many attempts at explaining the effect [39] [44] [25] [42], but none are completely satisfactory.

2.4 Jet fragmentation

Having examined the bound states QCD is capable of producing, it is now useful examine another aspect of QCD at a different energy scale: the fate of a recoiling parton in a hard[6] interaction. Confinement makes it impossible for a parton to propagate through space without forming a color singlet state. What is needed is a framework for discussing the transition between a single hard parton and the shower of hadrons ultimately measured in the detector as a jet.

As in the production of quarkonium states, there are two energy scales which must be separated to make progress with the QCD processes. The scale where perturbation theory can be applied is separated into what is called the parton shower. The non-perturbative part of the process is the transition from partons into hadrons referred to as hadronization.

2.4.1 Parton Shower

Figure 2.4 shows the various initial and final state parton configurations which contribute to a parton shower. An entire shower consists of a series of splittings following different probability distributions depending on the outgoing partons at each splitting. The process is dissipative, in the sense that the energy is shared between the final state partons, and at each branching the energy of a given parton is less than the previous branching's daughters. When the final state partons fall below a certain

[5] The alliteration seems to have contributed to the persistence of this name versus the "spin-alignment inconsistency." It appears that LHCb uses J/ψ polarization, while other experiments use "spin-alignment." Theory papers use each interchangeably.

[6] Hard here refers to high energy, conversely soft refers to low energy.

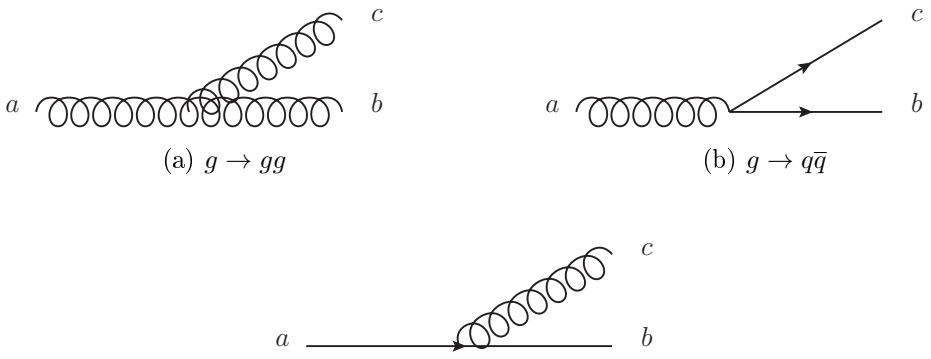

(a) $g \to gg$ (b) $g \to q\bar{q}$ (c) $q \to qg$

FIGURE 2.4: Feynman vertices that contribute to a parton shower.

threshold the non-perturbative effects of hadronization take over and the partons form hadrons which are ultimately detected by the experimental apparatus.

The parton splitting functions have characteristic differences that affect the outcome of the shower. Following Chapter 5 of [30], the shower is assumed to follow timelike branching. The energy fraction z of branching is defined as:

$$z = E_c/E_a = 1 - E_b/E_a. \tag{2.17}$$

After averaging over the possible polarization states of the incoming and outgoing gluons the amplitude for splitting from n partons to $n+1$ partons is given by

$$|\mathcal{M}_{n+1}|^2 \sim \frac{4g^2}{t}\hat{P}_{bc}(z)|\mathcal{M}_n|^2. \tag{2.18}$$

Here g is the QCD coupling constant, $t \equiv p_a^2$ and $\hat{P}_{bc}$ is the unregularized splitting function for the final state partons. The gluon splitting function corresponding to Figure 2.4a is

$$\hat{P}_{gg}(z) = C_A\left[\frac{1-z}{z} + \frac{z}{1-z} + z(1-z)\right]. \tag{2.19}$$

Here the color factor is $C_A = 3$. It is useful to take the various limits. Notice that when one of the partons is soft either (c soft) $z \to 0$ or (b soft) $z \to 1$. The first

term of equation 2.19 is divergent for $z \to 0$. The same is true for the second term as $z \to 1$. These divergences favor soft emission of gluons.

Following the same prescription, the splitting function for gluon emission from a quark (see Figure 2.4c) is

$$\hat{P}_{qg}(z) = T_R[z^2 + (1-z)^2] \tag{2.20}$$

in this case the color factor is $T_R = 1/2$. Taking $z \to 0$ favors soft gluon emission whereas the $z \to 1$ limit favors hard emission of the gluon. The parabolic nature of the function favors one extreme or the other.

The remaining case corresponds to Figure 2.4b and is for a gluon splitting into a quark anti-quark pair. The spin-averaged splitting function is

$$\hat{P}_{qq}(z) = C_F \frac{1+z^2}{1-z}. \tag{2.21}$$

This function is unique among the splitting functions in that it favors one of the outgoing partons to be harder than the other. Figure 2.5 shows the three splitting functions defined above. An arbitrary normalization is applied to the P_{qq} and P_{gg} functions in order to better compare the behavior of the shapes.

The contributions from these individual diagrams and splitting functions can be used to simulate a parton shower. An example parton shower from an e^+e^- annihilation event taken from [30] is shown in Figure 2.6.

2.4.2 Hadronization

The partons produced during the shower must form hadrons; an inherently non-perturbative process. The phenomenological model used by Pythia is the Lund string model [58]. This model extends the string analogy developed in Section 2.2.2. The idea is that hadrons in the shower are connected via color-strings. If the energy stored in the string rises above the threshold to produce a $q\overline{q}$ pair, the string snaps

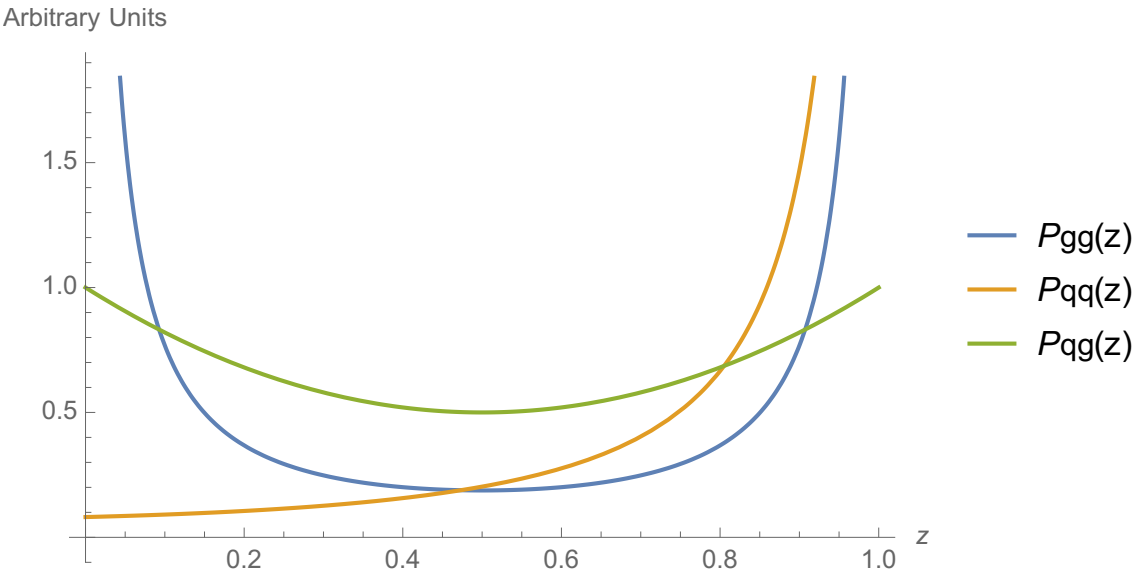

FIGURE 2.5: The splitting functions required for a parton shower. An arbitrary normalization is applied to P_{qq} and P_{gg} in order to allow better comparison of the shapes.

and the process is repeated until the energies of the remaining string segments fall below a threshold value. Below this threshold, the string fragments form the final state hadrons.

If there are gluons present in the final state of the parton shower, they are connected to the color strings as dynamical kinks in the string (see the upper part of the shower in Figure 2.7). Figure 2.7 shows an example of this process in an e^+e^- event [30]. When a gluon splits perturbatively into a pair of quarks it creates another string segment [30]. The lines outgoing from the gray string segments represent the subsequent fragmentation of the string as described above. With a complete description of QCD, the allowed bound states, and the transition from a high energy parton to the hadrons ultimately measured by the detector it is time to discuss the actual measurement of particles at the Large Hadron Collider.

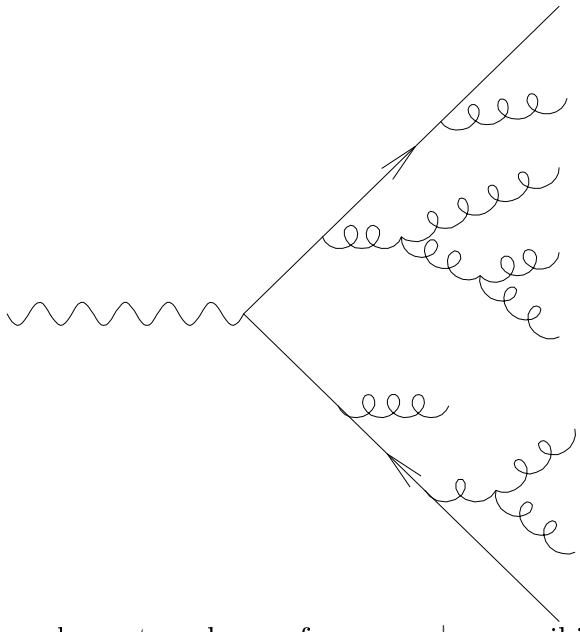

FIGURE 2.6: An example parton shower from an e^+e^- annihilation event. Figure taken from [30].

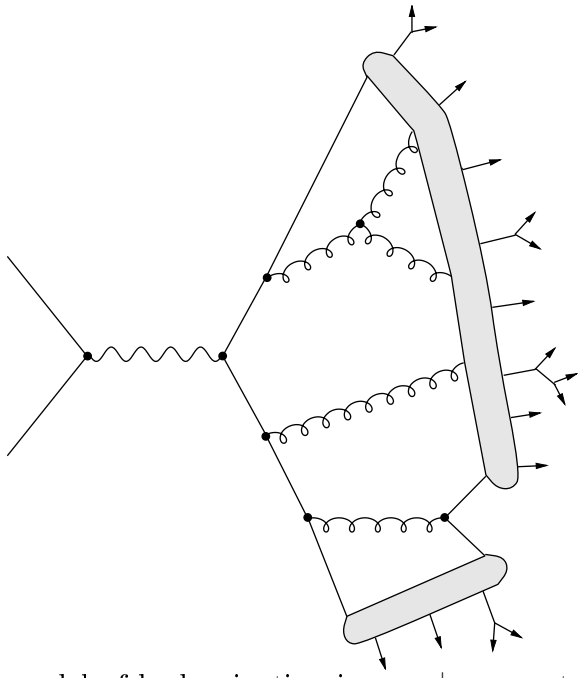

FIGURE 2.7: String model of hadronization in an e^+e^- event. Grey shaded region is the string. Figure taken from [30]

3

The ATLAS experiment

3.1 The Large Hadron Collider

The Large Hadron Collider (LHC) is the largest (in size and energy) circular hadron collider in existence. The circumference of the colliding rings is 26.7 km and is buried between 45 m and 170 m below parts of Switzerland and France [31]. The LHC was built based on infrastructure developed for the Large Electron Positron collider and utilizes the CERN accelerator complex in order to boost protons to the high energies required for circulating in the LHC tunnel. The LHC circulates beams of protons in opposite directions and steers them into each other at four points around the accelerator ring. These four points are the sites of the major LHC experiments, CMS, ATLAS, LHCb, and ALICE [31]. The data for this work was recorded in 2012 when the machine was configured to run each beam of protons at 4 TeV for a center of mass energy $\sqrt{s} = 8$ TeV.

In order to collide protons, the LHC accelerates them through a series of booster rings until they are injected into the main accelerator complex. Protons injected into the LHC are organized into bunches of 10^{11} protons. The bunches are spaced

according to the frequency (400 MHz) of the RF cavities which accelerate the particles. During the first run of the LHC, the bunches were spaced 50 ns apart which is twice the designed bunch spacing of 25 ns.

In order to achieve this configuration of bunch crossings as well as precise control of the proton beams, a number of problems must be addressed. Foremost is the bending the protons around the ring. This is achieved using 1,232 superconducting magnetic dipoles [31]. Each of these dipoles is operated at 1.9 K and produce a field strength of 8 T. The operating temperature of the magnets has a tight margin above which the superconductivity is lost and the magnet ceases to superconduct [31]. This transition is known as quenching, and when it occurs all of the energy stored in the field is released. An unintended quench in 2008 led to a massive helium explosion and delayed the experiments by a year [43].

Another aspect that is important to the smooth operation of the LHC is the vacuum in the beam pipe. In order to maximize beam lifetime and minimize experimental backgrounds, the beam pipe must be kept as pristine as possible. This equates to a vacuum pressure of 10^{-10} mbar. In the regions around the experiments, the vacuum is designed to keep the density of hydrogen below 10^{13} H_2 m^{-3}. As a point of reference, the volume of beampipe contained by the ATLAS detector is roughly 0.008 m^3. This means that there is roughly 8×10^{10} hydrogen atoms in the ATLAS beampipe at any given time. The same volume of hydrogen gas at STP results in 2.15×10^{24} atoms. This is a difference in concentration of roughly 30 parts per quadrillion.

3.1.1 Luminosity

Many of the measurements made at the LHC boil down to counting experiments answering the question: "How many particles with properties x, y, and z do I see?" These properties may be the transverse momentum (p_T), invariant mass (m), or

rapidity (y). The experimental physicist reconstructs events, selects those matching the required criteria and compares the number counted to a theoretical calculation.

Conversely, a theoretical physicist calculates the number of observed particles with given properties x, y and z by starting with incoming protons and working out the probability of observing the expected particles. The proton beams are characterized by a parameter called the luminosity L of the beam which is the number of particles passing per second per unit area. When a theoretical physicist calculates the cross section[1] of a process ($\sigma(pp \to AB)$ where A and B are outgoing particle species), the rate of particles produced is given by the product of the luminosity and the cross section,

$$dN/dt = L(t)\sigma(pp \to AB).$$

In order to predict the absolute number of events, this expression must be integrated over the time that data was collected

$$N = \sigma \int L(t)dt.$$

The amount of data collected by the experiment is measured in the integrated luminosity. It has units of inverse barns which are convenient for back-of-the-envelope calculations of the expected number of events for a process: take the product of the luminosity collected and the expected cross section to get the number of events.

The instantaneous luminosity L of the LHC is given by the following formula:

$$L = \frac{N_b^2 n_b f_{\text{rev}} \gamma_r}{4\pi \epsilon_n \beta^*} F. \tag{3.1}$$

The denominator of this equation is fairly straightforward. The N_b term is the number of protons per bunch (typically $N_b \sim 10^{11}$), n_b is the number of bunches per

[1] This quantity has SI units of cm^2 but barns are most commonly used in the field. The name comes from the saying "you couldn't hit the broadside of a barn" and originated during research into the atomic bomb [55]. Another unit from this era is the "shake" as in "two shakes of a lamb's tail" which is 10 ns, a convenient unit of measure in nuclear reactions [55].

beam, f_{rev} is the revolution frequency of the machine, γ_r is the relativistic gamma factor for the bunches and F is a geometric factor to account for the geometry of the crossing angle at the interaction point (IP). The denominator must be a unit of area from dimensional analysis. The transverse beam emittance is given by ϵ_n and β^* is the value of the β function at the IP. The two parameters ϵ_n and β describe the major and semi-major axes of an ellipse which describes the transverse phase-space profile of the LHC beam. Together they describe the effective area of the beam at the IP [31].

The geometric factor F can be worked out from small angle approximations as well as the RMS length and transverse width of the beam,

$$F = \left(1 + \left(\frac{\theta_c \sigma_z}{2\sigma^*}\right)^2\right)^{-1/2}. \tag{3.2}$$

Here θ_c is the crossing angle, σ_z is the RMS length of a bunch crossing and σ^* is the transverse RMS beam size for a gaussian beam.

When the beams cross, there is a high probability that multiple high energy interactions take place. The interaction which is selected for study is referred to as the primary interaction. Secondary interactions contribute to the experimental background which are referred to as pileup. The degree of pileup can be measured by the average number of interactions per bunch crossing ($\langle\mu\rangle$). For the data used in this thesis, the pileup was 20 interactions per bunch crossing on average. Pileup presents an experimental challenge because the particles produced in association with the events can confuse the reconstruction algorithms used. This analysis makes use of reconstructed quantities that are largely insensitive to pileup effects.

3.2 The ATLAS experiment

A Toroidal LHC AparatuS (ATLAS[2]) is one of the general purpose detectors at the LHC. It is located at Point 1 on the LHC ring. Figure 3.1 shows a high-level drawing of the detector. The detector itself is 44m long and 25 m tall[3]. The ATLAS detector contains many subsystems which allow it to detect and reconstruct particles which are created by collisions at the IP. The detectors all work on the principle that when a charged particle moves through matter it can either radiate energy in the form of Bremsstrahlung, ionize the surrounding matter, or interact with the nucleus of the matter the particle traverses. In the first case, the radiation can be detected directly, or it can produce a positron and electron pair (pair production) which can be subsequently detected. Different parts of the detector exploit these three processes in different ways. The electromagnetic and hadronic calorimeters work to stop electrons and hadrons while accurately measuring the energy of the incident particle. Tracking elements aim to accurately detect the time and location where a charged particle passes and do so in different ways.

In order to accurately measure the charge and momentum of particles passing through the detector, a set of magnets is used to bend the charged particles. ATLAS uses a unique configuration of a 2.0 T solenoid covering the inner detector and a toroidal configuration of 8 superconducting yokes which provide a field between 0.5 T and 1.0 T [26]. The central solenoid ensures that charged particles bend in the transverse plane of the inner detector. The toroidal configuration of the outer magnets bend the muons which exit the hadronic calorimeter, allowing for a precise measurement of the three spatial components of their momentum. Together these systems allow the measurement of the particle's four-momentum and charge. This

[2] ATLHCA doesn't have the same ring or status as a greek titan.

[3] The detector weighs approximately 7000 tons. If the volume the detector contains were hermetically sealed, the density of the detector would allow it to float if it were put in fresh water.

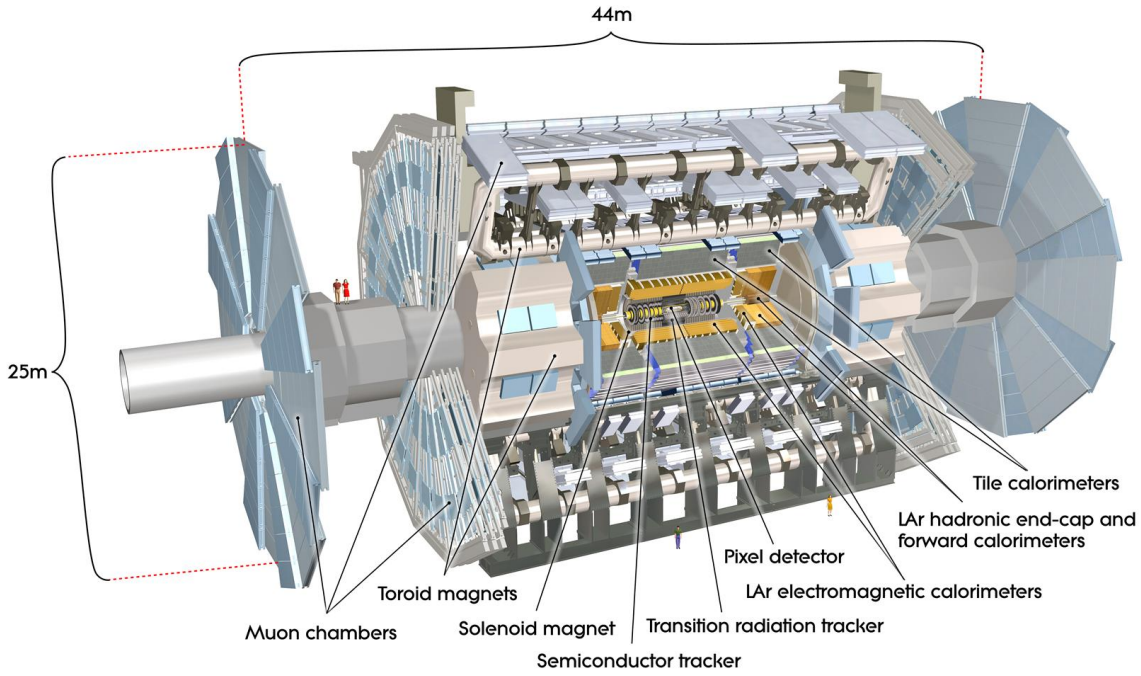

FIGURE 3.1: A cutaway of the ATLAS detector. Two small people are shown to scale.

analysis exclusively uses charged particle tracks in the form of muon identified tracks, and inner detector tracks. This was done in order to minimize various systematic effects that will be discussed.

ATLAS uses a right-handed cylindrical coordinate system with the z-axis oriented along the beam line; see Figure 3.2 for details. In cartesian coordinates, the x and y axes are in the plane transverse to the beamline. The x axis points to the center of the ring and the y axis points to the Earth's surface. A useful quantity for describing angles in the detector is pseudorapidity (η)[4] defined as $\eta \equiv -\log(\tan(\theta/2))$. In this variable, the beam line is $\eta \approx 5$, while the y axis corresponds to $\eta = 0$.

[4] Differences in pseudorapidity are invariant in relativistic boosts along the beam axis which is very useful experimentally.

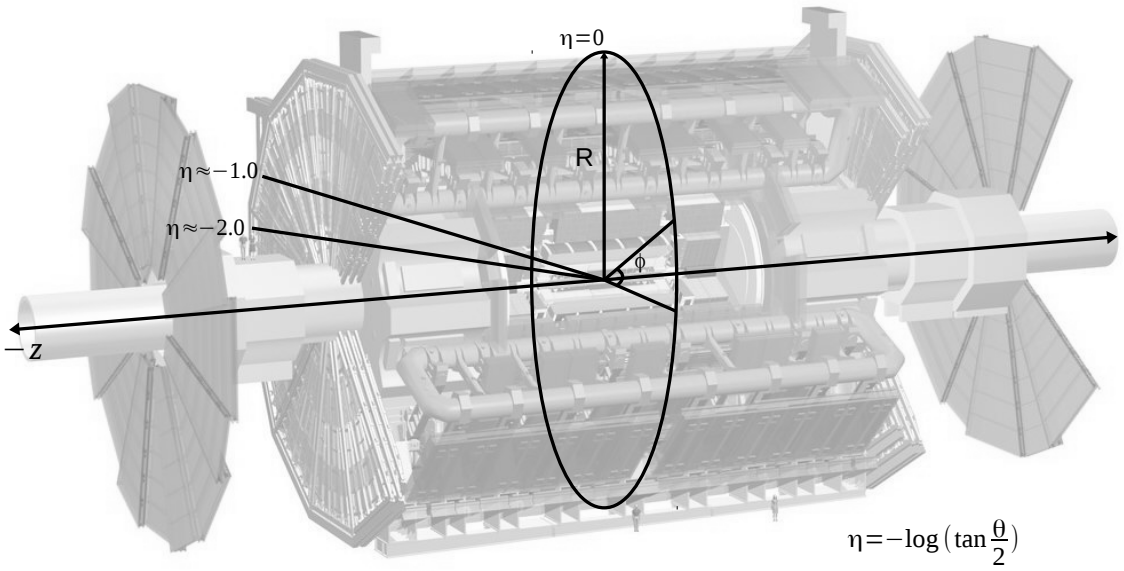

FIGURE 3.2: The ATLAS detector's coordinate system, see text for definition of pseudorapidity (η).

3.2.1 Inner Detector

Figure 3.3 shows the inner detector at ATLAS with each subsystem labeled. Figure 3.4 shows a view of the inner detector for a wedge of the detector. Working radially outward from the IP, the ATLAS inner detector is comprised of three main components: the pixel detector (extending 45.5 mm $< R <$ 242 mm), the silicon strip detector (SCT) (extending 255 mm $< R <$ 549 mm), and the transition radiation tracker (TRT) (extending 554 mm $< R <$ 1082 mm). The pixel detector and SCT function based on semiconductor technologies that allow them to measure the location of charged particles with high precision. The TRT operates based on transition radiation, a phenomenon that occurs when charged particles traverse different

materials. During the transition between materials, particles are very likely to emit radiation which is subsequently detected. Table 3.1 shows the intrinsic accuracy of the inner detector subsystems and their alignment tolerances.

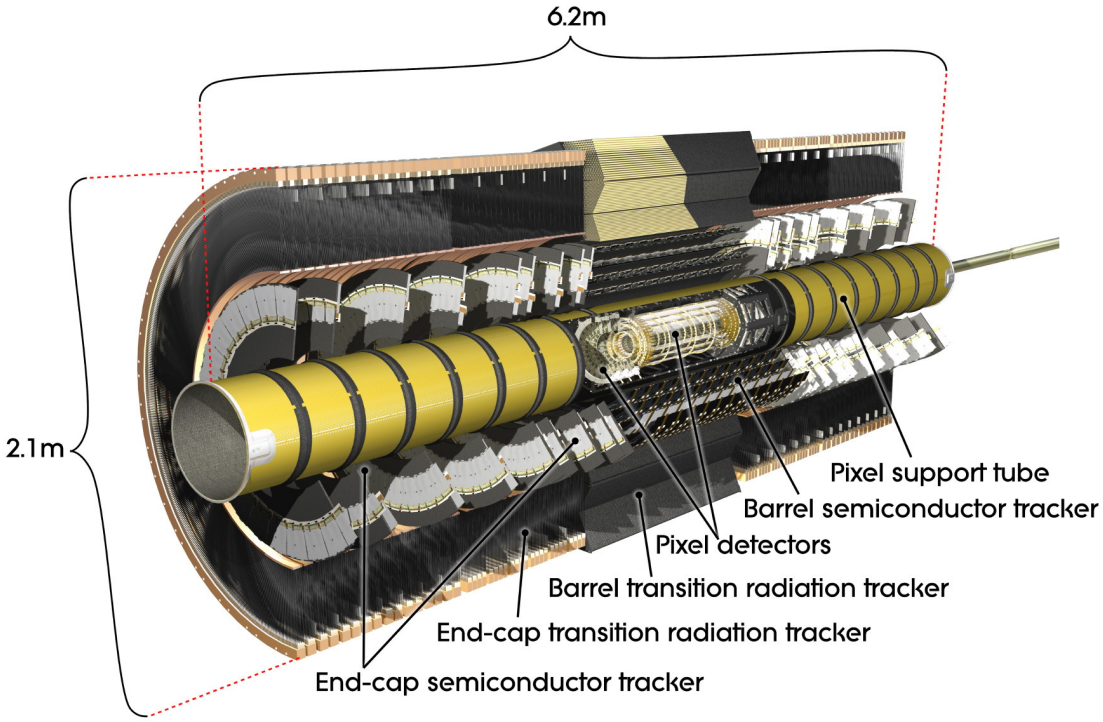

FIGURE 3.3: The ATLAS inner detector taken from [1].

Semiconductor based detectors

The pixel detector and the silicon strip tracker utilize the ionization of matter as charged particles pass through the active regions. The active region of the detectors is constructed by forming a layer of n-doped and p-doped semiconductor. These layers are held at a fixed voltage. When a charged particle traverses the active region, the ionized material becomes conducting allowing for the location of the particle to be determined. Figure 3.5 shows a schematic of a pixel. The bottom half of the schematic is the sensing region and the dark gray and lighter gray regions represent the doped semiconductor. The bump-bond indicates a fabrication technique

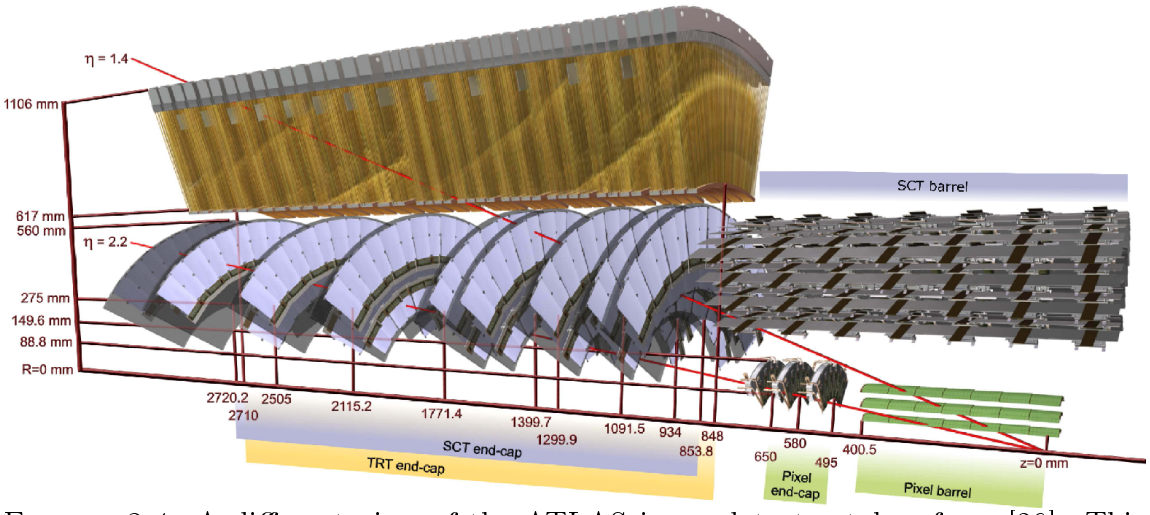

FIGURE 3.4: A different view of the ATLAS inner detector taken from [26]. This shows the geometry of the pixel and SCT detectors focusing on the end caps and the TRT end cap.

Subsystem	Intrinsic Accuracy (μm)	Alignment Tolerance (μm) Radial (R)	Axial (z)	Azimuth (R-ϕ)
Pixel				
Layer-0	10 $(R-\phi)$ 115 (z)	10	20	7
Layer-1 and 2	10 $(R-\phi)$ 115 (z)	20	20	7
End cap	10 $(R-\phi)$ 115 (R)	20	100	7
SCT				
Barrel	17 $(R-\phi)$ 580 (z)	100	50	12
End cap	17 $(R-\phi)$ 580 (R)	50	200	12
TRT	130			30

Table 3.1: Intrinsic accuracy and alignment tolerances of the inner detector. The lower accuracy of the axial dimension in the SCT is due to the intrinsic pitch of the SCT modules. The axial accuracy of the pixel detector is driven by fabrication constraints [26].

utilized to provide uniform attachment of each micro-fabricated pixel to the readout electronics.

Pixel Detector

The fundamental unit of the pixel detector is a module. Figure 3.6 shows the various layers that go into a pixel module. A module consists of readout electronics and active pixel sensors which detect the position of charged particles. Each module

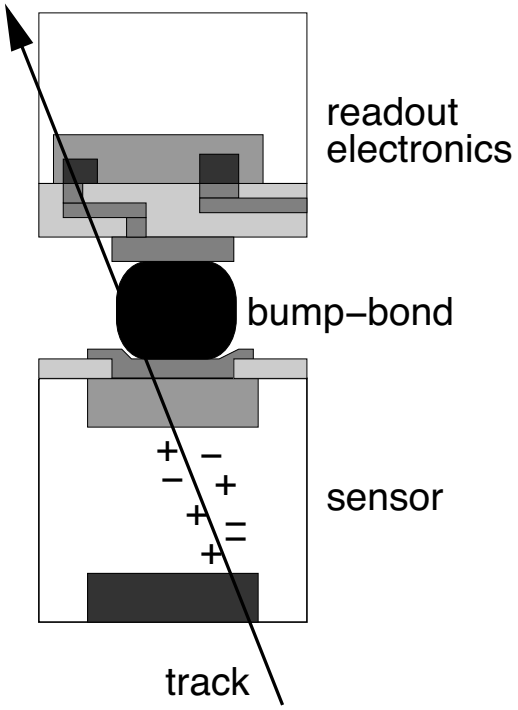

FIGURE 3.5: Conceptual diagram of the pixel assembly with a charged particle traversing it [1].

has a sensitive surface $6.08 \times 1.64\text{cm}^2$ [1]. Each module consists of 47232 pixels [1]. The entire pixel detector is constructed from 1744 modules [1]. These modules are arranged in three concentric cylinders. The forward region of the detector is covered by three rings of end-cap modules on either end of the pixel barrel region. The geometric arrangement of the modules can be seen the green components in Figure 3.4. Each module has three spatial degrees of freedom and two angles which determine its precise location in space. Aligning these modules is critical to achieving an accurate measurement of the particles' momentum when they pass through the inner detector. Table 3.1 shows the alignment tolerances of the pixel detector.

Silicon Strip Detector

Continuing radially outward is the Silicon Strip Detector (SCT). The SCT follows the modular design of the pixel detector but with less axial resolution than the pixel

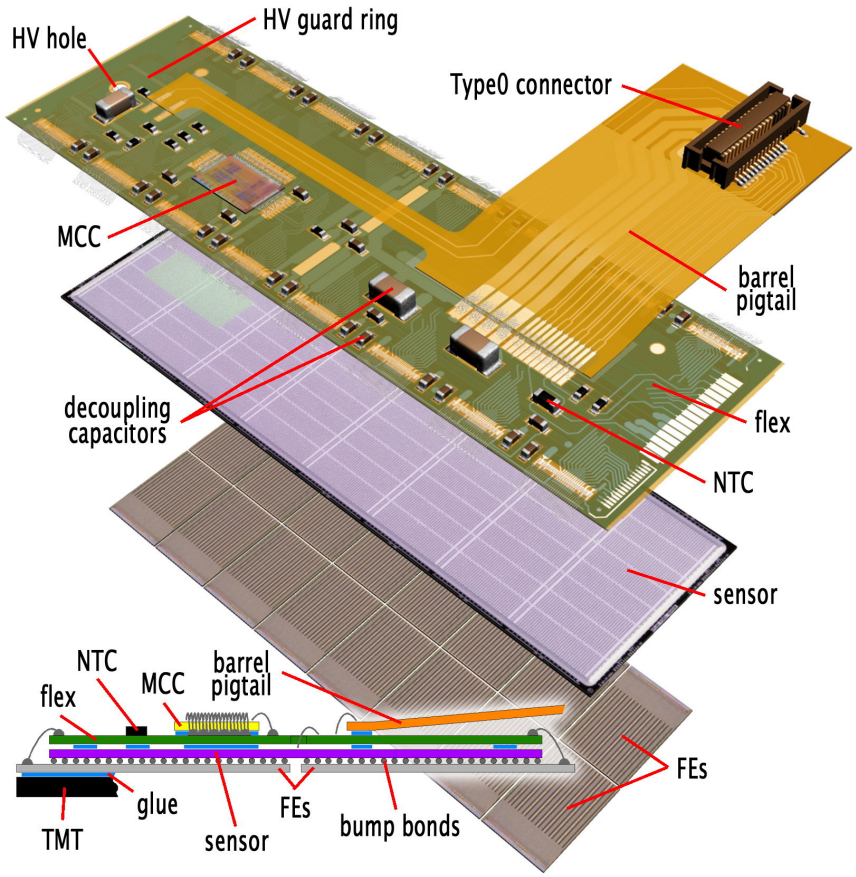

FIGURE 3.6: Schematic of the module assembly. 47232 pixels are read out from the sensor layer and each one is bump-bonded to the readout electronics [1].

detector. Table 3.1 shows the nominal resolution and alignment tolerances of the SCT. Each SCT module has five degrees of freedom which must be corrected for during alignment and calibration. The SCT barrel module layout is shown in Figure 3.7. One barrel module has two layers of strips set at an 80 μm pitch over 6cm in order to give a trapezoidal geometry [26]. The end cap modules follow a similar construction but a slightly different geometry in how the strips are arranged. The strips in the end cap modules are set at various pitches but have an inter-strip angle in order to cover the radial plane better [26].

When charged particles pass through the SCT, they trigger the readout of various strips within the SCT. If only two strips are read out, then the approximate

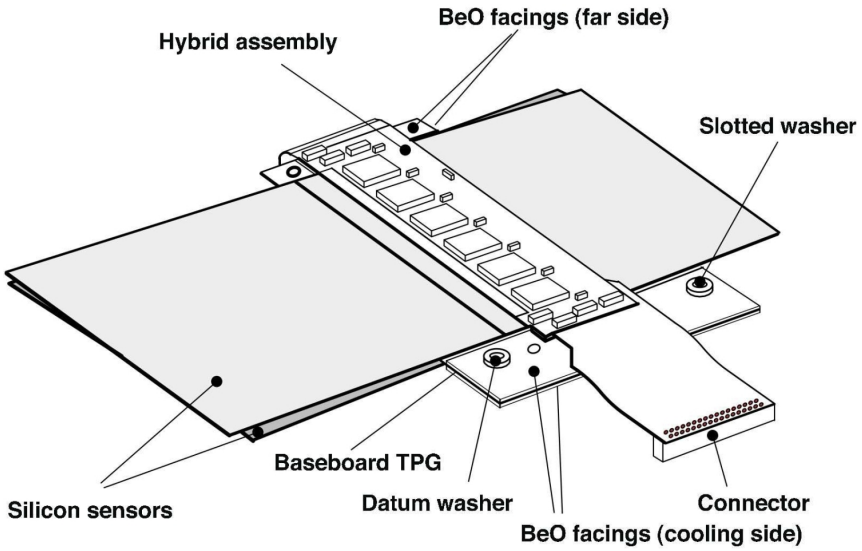

FIGURE 3.7: Illustration of an SCT barrel module, note the two layers of silicon sensors and their relative pitch. Each module is 6cm long. Figure taken from [26].

location of the particle can be inferred from the closest crossing of the two strips. If the charged particle passes the SCT module while another strip is active (which is possible in the high occupancy environment of ATLAS) an ambiguity arises as to where the charged particle passed. Figure 3.8 shows this situation. The trapezoidal geometry creates a large enough separation between the ambiguous hits that one can be rejected in favor of the other when information from the other SCT and pixel layers are taken into account.

Transition Radiation Tracker

The final inner detector subsystem is the transition radiation tracker (TRT). While the pixel and SCT detectors rely on semiconductor technology, the TRT utilizes ionization that occurs when a charged particle traverses material of differing dielectric constants. This process depends on the species of the charged particle and can be used in particle identification [54]. For a thorough review of the physics of transition radiation, see [13]. Figure 3.3 shows the barrel and end cap TRT. The TRT is constructed from a series of densely packed 298,304 straw tubes, 4mm in diameter,

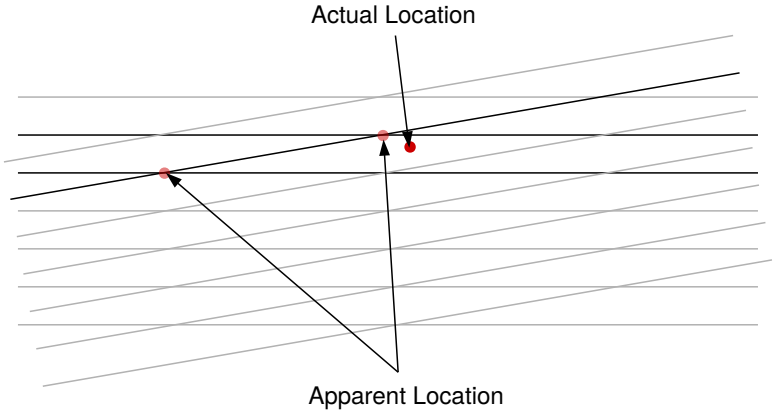

FIGURE 3.8: Illustration of a charged particle interacting with the SCT strips. Black strips indicate they have been read out, grey are inactive. When three or more strips are active, an ambiguity in the location of the charged particle arises.

which each contain an anode wire at the center [10][27]. The anode is a gold-plated tungsten wire. The gas circulated in the straw tubes is a gas consisting mostly of xenon. A noble gas is used in order to reduce the time that ionized particles recombine into neutral atoms [10]. This maximizes the ability to read out when a charged particle passes through the tube. The interstitial space between the straw tubes is a polypropylene foam which encourages charged particles to emit transition radiation when they pass through the TRT volume allowing for the identification of electrons. In the end caps, the interstitial volume contains foil for the same purpose [10].

Figure 3.9 shows the geometric lengths involved in detecting the location of a charged particle [53]. As the charged particle ionizes the gas the free charge flows to the anode creating a characteristic curve depending on the distance to the anode. When the collected charge rises above a threshold it is considered a hit and the time-over-threshold allows the determination of the radius R in Figure 3.9. This

information is then used for the overall reconstruction of charged particle tracks in conjunction with the information from the SCT and pixel detectors.

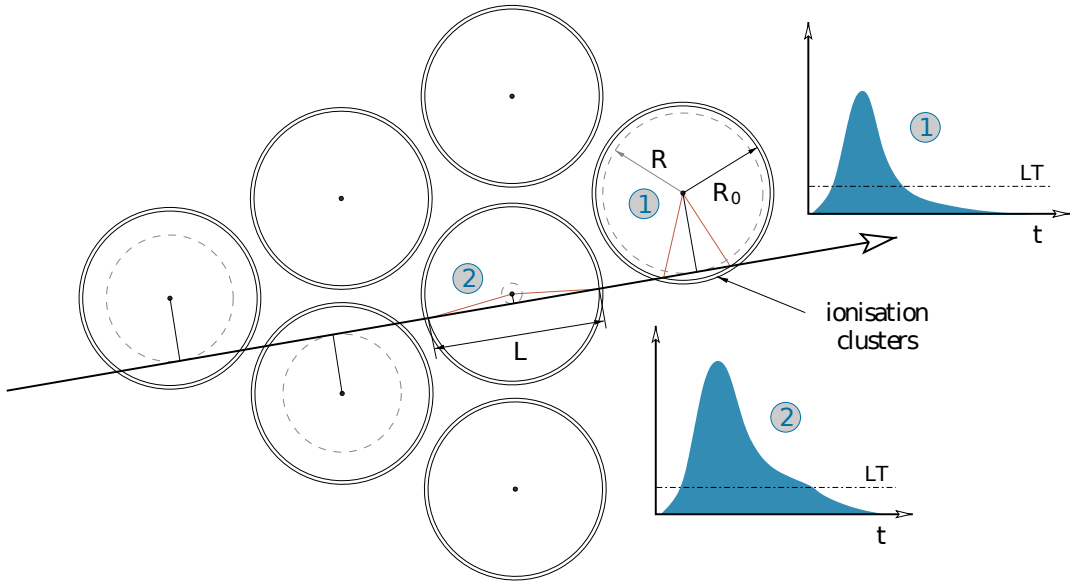

FIGURE 3.9: As a charged particle ionizes the gas inside the straw tube, charge is collected over time as shown in the blue profiles indicated by the numbers in the straw tubes. When the particle passes closer to the anode the profile of the deposited charge changes [53]. Low Threshold (LT) indicates the transition between signal and noise in the event readout.

During reconstruction, the quality of the hits extracted from the time-over-threshold measurement of the radius must be assessed. Figure 3.10 shows the definition of these hits. When the estimated drift radius corresponds to where a charged particle passed it is referred to as a precision hit. When the charged particle passes through the tube, but the estimated radius is incorrect it is called a tube hit. When the particle's extrapolated path passes outside the tube that registered the hit altogether it is an outlier and when the tube doesn't register an expected hit at all it is a hole [45].

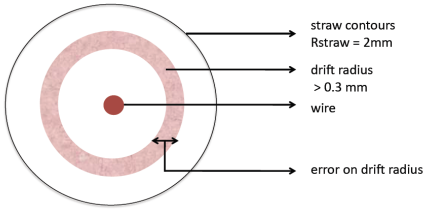

(a)

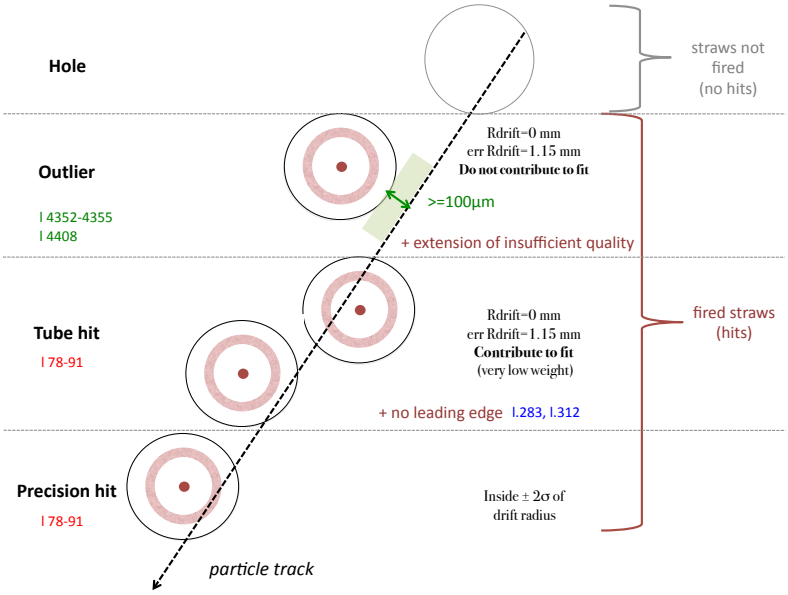

(b)

FIGURE 3.10: Definition of hit qualities used by TRT reconstruction [45]

3.2.2 Calorimeter systems

The calorimeter systems used at ATLAS are shown in Figure 3.11. ATLAS utilizes various calorimeter technologies based on stopping particles and measuring the deposited energy. Calorimeters at ATLAS use an interleaved geometry of scintillation material and a dense absorbing material for stopping impinging particles. Scintillation light is collected along fiber optic cables and read out using photomultipliers. There are two main calorimeter systems, the electronic calorimeter (ECAL) and the hadronic calorimeter (HCAL). The ECAL is designed to fully stop and measure electrons and photons. Hadrons deposit some energy in the ECAL, but typically make

it to the HCAL before fully stopping and depositing their entire energy.

It is important to note the contrast between how the inner detector and the calorimeter measure the momentum of particles. The location charged particles pass are precisely measured in the inner detector. This information coupled with the knowledge of the magnetic field the inner detector is immersed in allows for the measurement of the particle's three-momentum. In order to fully extract the relativistic four-momentum a mass hypothesis is assumed[5]. The calorimeter works to measure the energy of the impinging particle by stopping it and measuring the deposited energy. For electrons, the associated inner detector track allows for the extraction of the four-momentum. For other particles, the energy and the location in the detector allow the measurement of the particle's three-momentum. The error on these two measurements is fundamentally different, and the calibration of the two detectors is performed in different ways. This leads to a difference in the energy measured by charged particles and is the motivation for only using the charged fraction of hadrons produced in events of interest to this analysis.

As with other subsystems in ATLAS, the ECAL consists of separate barrel and end-cap detectors with slightly different geometries. Figure 3.12 shows a segment of the ECAL system. The ECAL utilizes an accordion geometry to ensure that more than one layer is active when an electron or photon is depositing its energy in the calorimeter. This provides full coverage in the ϕ direction. The ECAL is finely segmented in η ($\Delta\eta = 0.0031$) close to the inner detector and less so in the bulk of the detector ($\Delta\eta = 0.025$). The end of the ECAL is covered with coarse "trigger towers" with a segmentation of $\Delta\eta = 0.1$ [26]. These towers are used to trigger on events where a coarse estimate of the event's energy is needed to decide if the event should be recorded or not. The ECAL's active material is liquid Argon (LAr),

[5] For charged particles not associated with electrons, the pion mass is assumed. For tracks with muon spectrometer information, the muon mass is assumed.

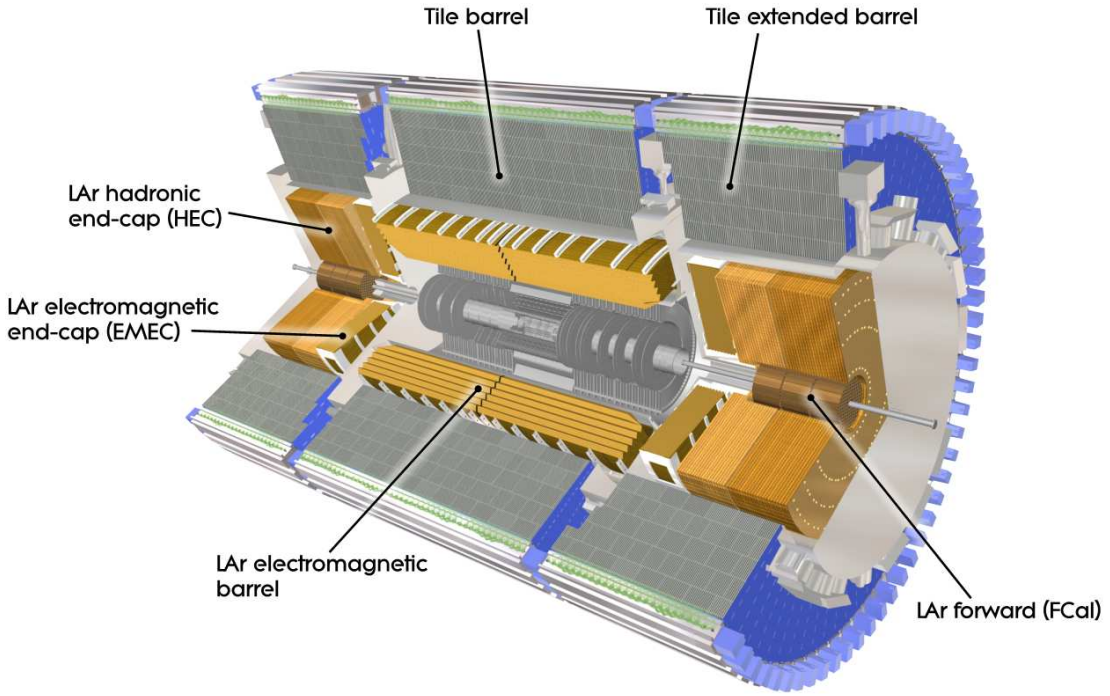

FIGURE 3.11: The ATLAS calorimeter systems

which is chosen for its intrinsic radiation hardness and its linear response to charged particles [26]. Lead is used as the absorber in the ECAL. Lead is an ideal choice due to its high density and the compact nature of the ECAL compared to the HCAL.

While the ECAL utilizes a accordion geometry, the HCAL utilizes a slightly different form. The absorption material in the HCAL is steel and the scintillation material is a plastic based on polystyrene doped with fluors [26]. The HCAL is separated into the barrel region, referred to as the tile calorimeter, and the forward region covered by the hadronic end-cap calorimeters (HEC). The calorimeter is segmented into regions of $\Delta\phi \times \Delta\eta = 0.1 \times 0.1$ for $|\eta| < 2.5$ and $\Delta\phi \times \Delta\eta = 0.2 \times 0.2$ for larger values of $|\eta|$ [26]. A tile module is shown in Figure 3.13. The scintillation light is guided out to fiber optic cables which are directed to photomultipliers at the top of the tile unit. The fiber optic cable is 3mm thick and has an emission peak at 476 nm [26]. This means the light that is optimally transmitted by the cables is a blue-cyan

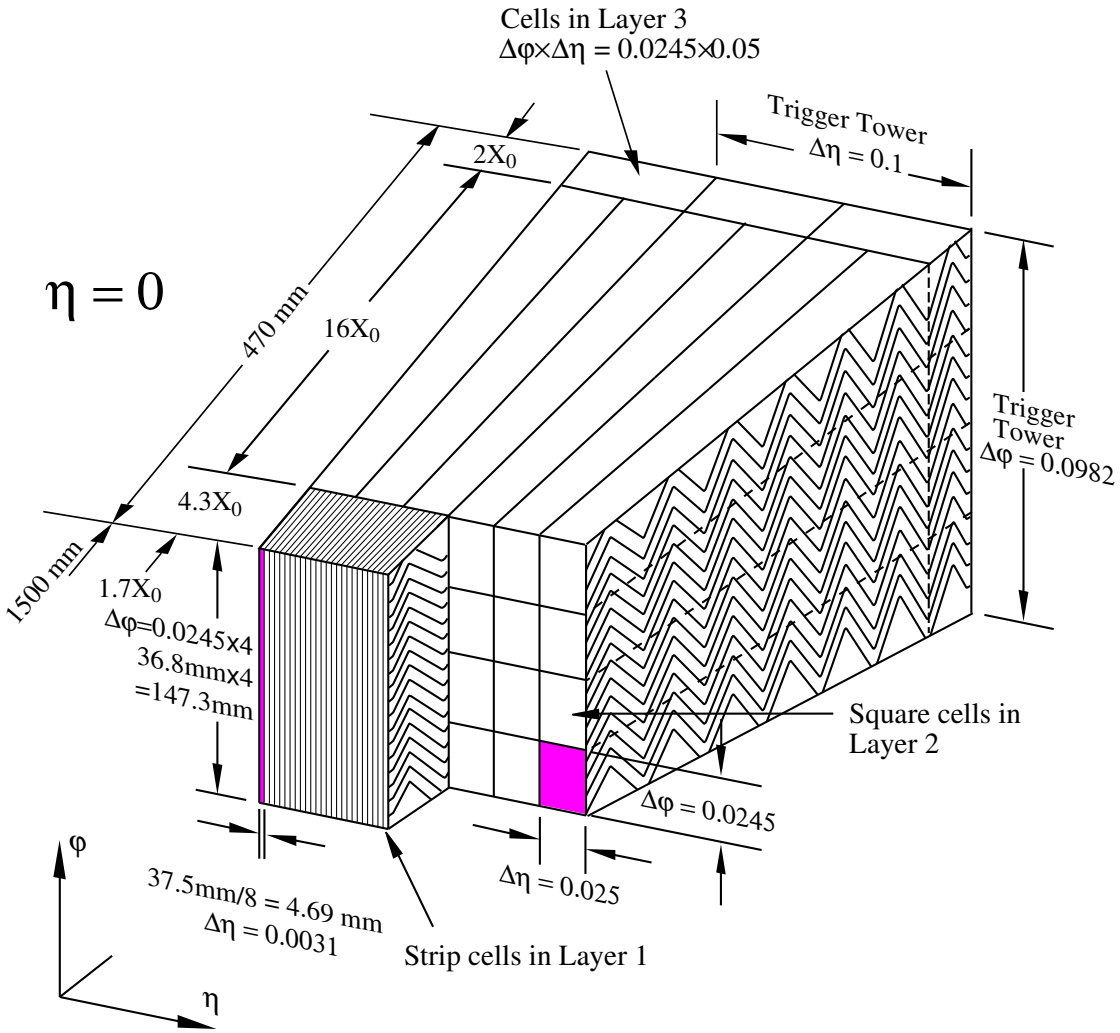

FIGURE 3.12: Illustration of the ECAL granularity and geometry of a module [26].

color. Figure 3.14 shows the geometry and segmentation of the a HEC module.

3.2.3 Muon Spectrometer

Many important Standard Model processes decay to two leptons. When these leptons are electrons, they are reconstructed in the ECAL and inner detector. When they are muons, they are detected and reconstructed using the Muon Spectrometer. These detector subsystems are the outermost portion of ATLAS. Portions of the spectrometer are immersed in ATLAS's signature toroid shaped magnetic field. The toroid causes the muons to bend along the z axis allowing for a more precise

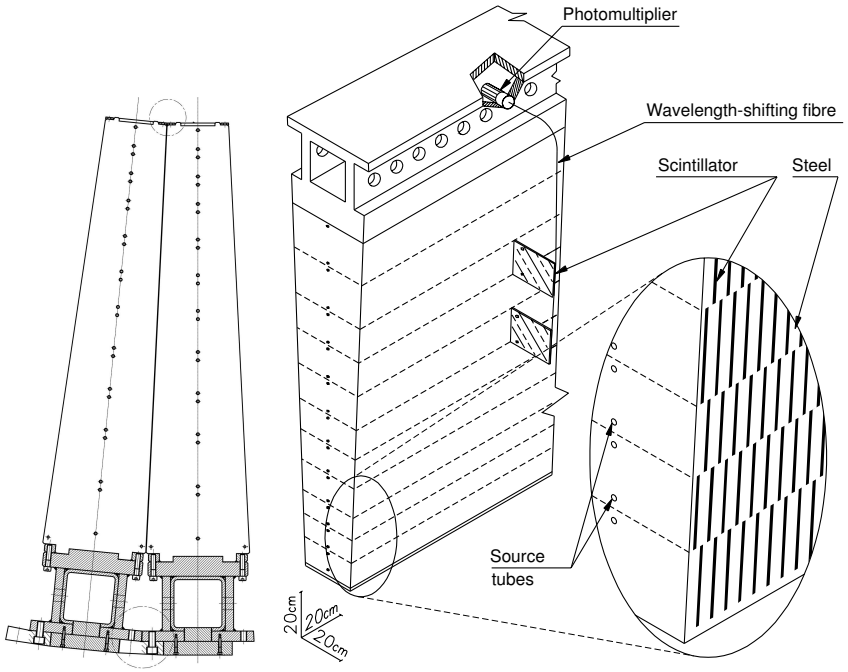

(a) (b)

FIGURE 3.13: Illustration of the HCAL module's scintillation and absorber geometry [26]. Figure 3.13a shows the layout of the tile calorimeter from the azimuthal view.

measurement of the three-momentum of the particle. The mass of the muon, relative to the electron, makes it much less likely to initiate a bremsstrahlung cascade as it passes through the ECAL and HCAL [47]. This allows it to reach the outer region of the detector where its location can be measured as precisely as possible.

ATLAS utilizes various detector technologies in order to measure the momentum of a 1 TeV muon within 10% of its nominal value [26]. To achieve this, the muon spectrometer consists of monitored drift tubes (MDTs), cathode strip chambers (CSCs), resistive plate chambers (RPCs) and thin gap chambers (TGCs). Each of these systems functions differently and serves slightly different purposes. Figure 3.15 shows the muon spectrometer. Table 3.2 lists the relevant numbers and coverage of the muon spectrometer [26].

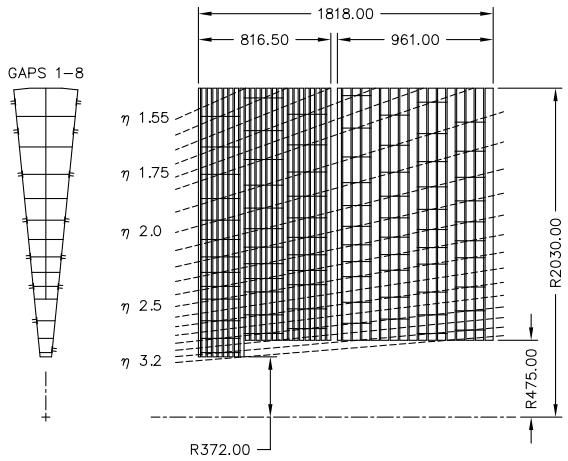

FIGURE 3.14: Schematic of a hadronic end cap calorimeter module [26].

Monitored Drift Tube

The underlying physics driving the function of the monitored drift tube is the same as the straw tubes in the TRT. The diameter of the drift tube is significantly larger (29.970mm) and the gas used is a mix of CO_2 (7%) and Ar (93%). The central anode is a tungsten-rhenium wire and is held at 3080V [26]. Figure 3.17 shows the front and side view of the MDT. Figure 3.18 shows how the MDTs fit together to form a module.

The green regions in Figure 3.16b show the MDT chambers for the barrel region which are also illustrated in Figure 3.18. MDTs are also utilized in the light-blue regions of Figure 3.16b as the end-cap chambers. They utlizes a trapezoidal geometry in order to better measure the radial location the muon traverses in the forward region [26].

Cathode Strip Chambers

Cathode Strip chambers (CSCs) are utilized in the very forward regions of the detector as illustrated in the yellow region of Figure 3.16b. This was done because of the CSC's higher rate capability and time resolution [26]. The geometry of the

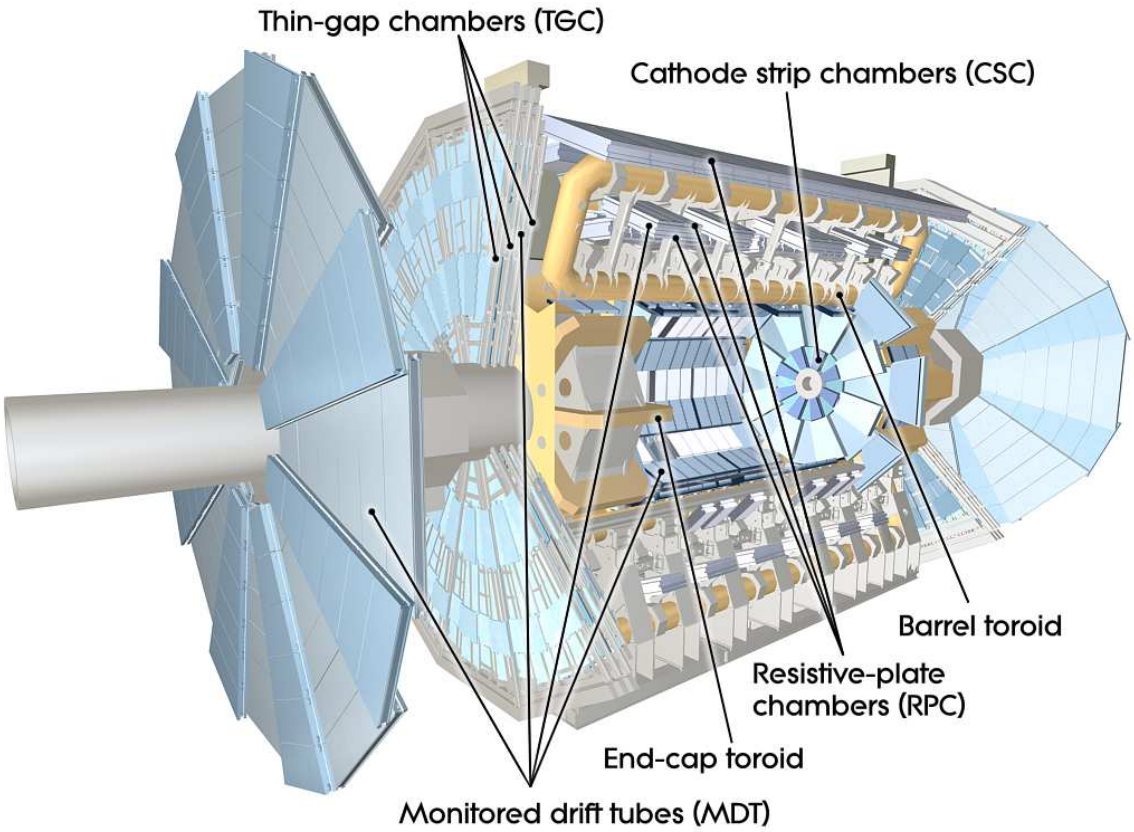

FIGURE 3.15: The muon spectrometer at ATLAS [26]

CSC is shown in Figure 3.19. The CSC is also required for tagging the time of the beam crossing. This requires that the time resolution of the detector be very precise. Integrating a measurement over the layers of the CSC allows the measurement of the time of arrival with an RMS of 3.6 ns [26].

The name Cathode Strip Chamber implies the detector type used. Cathode Strip Chambers are a series of cathode strips and anode wires oriented ninety degrees to each other. The cathodes are segmented to provide precision measurements of the transverse and longitudinal directions. The anode is held at 1900 V relative to the cathode. When a charged particle ionizes the Ar (80%) CO_2 (20%) mixture, it creates an avalanche of charge which is measured by the readout electronics. Figure 3.20a shows the geometric layout of the anode and cathode strips in a chamber. Figure

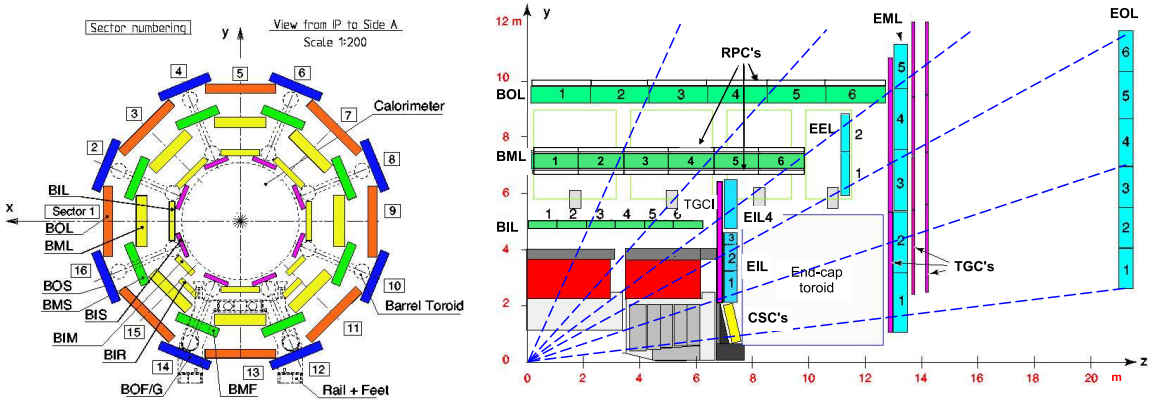

(a) (b)

FIGURE 3.16: Layout of the muon chambers in the muon spectrometer. See [26] for detailed description of the naming scheme, roughly "B" stands for Barrel, "E" for end cap, "L" for large, "S" for small, and "I", "M", and "O" stand for inner, middle, and outer respectively [26]. Infinite momentum muons would propagate along the blue dashed lines.

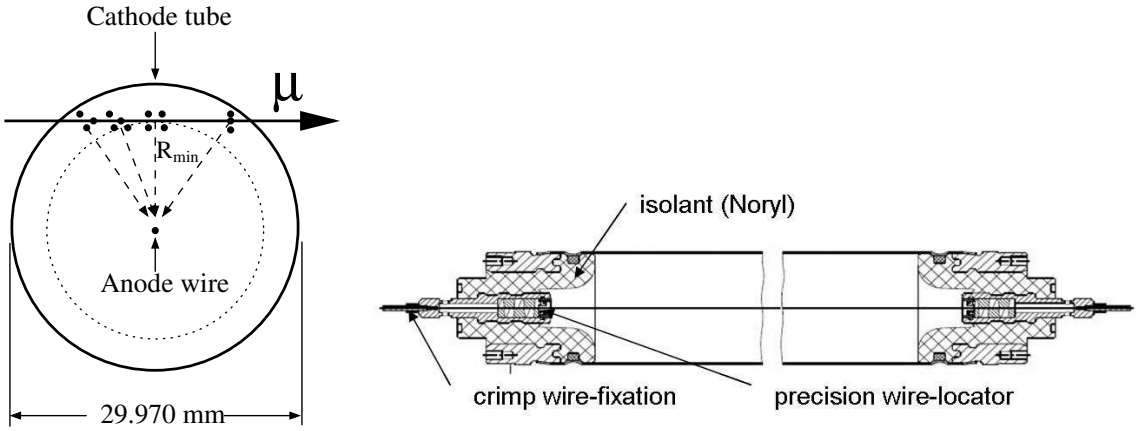

(a) (b)

FIGURE 3.17: Illustration of a MDT showing the cross section and longitudinal views [26].

Monitored Drift Tubes	
Coverage	$\|\eta\| < 2.7$ (innermost layer: $\|\eta\|$ 2.0)
Number of chambers	1088
Number of channels	354000
Function	Precision Tracking
Cathode Strip Chambers	
Coverage	$2.0 < \|\eta\| < 2.7$
Number of chambers	32
Number of channels	31000
Function	Precision Tracking
Resistive plate chambers	
Coverage	$\|\eta\| < 1.05$
Number of chambers	606
Number of channels	373000
Function	Triggering, second coordinate
Thin Gap Chambers	
Coverage	$1.05 < \|\eta\| < 2.7$ (2.4 for triggering)
Number of chambers	3588
Number of channels	318000
Function	Triggering, second coordinate

Table 3.2: Summary of channels and chambers utilized for each subsystem of the Muon Spectrometer at ATLAS [26]

3.20b is an illustration of the charge collected along the anode and subsequently measured by the readout electronics on the cathode strips.

Resistive Plate Chambers

While the CSC and MDT utilize technologies to precisely measure the location of muons passing in the muon spectrometer, resistive plate chambers (RPCs) and thin gap chambers (TGCs) are primarily used to trigger on muons by providing a coarse estimate of where and when a muon traversed the detector. The triggering system in ATLAS is covered in detail in Section 3.2.5. Figure 3.21 shows the RPC and TGC chambers that provide the readouts allowing fast triggering on muons. The RPC systems are able to trigger on muons with momentum between 9-35 GeV or 6-9 GeV depending on which system fires [26]. The RPC consists of two layers of dielectric

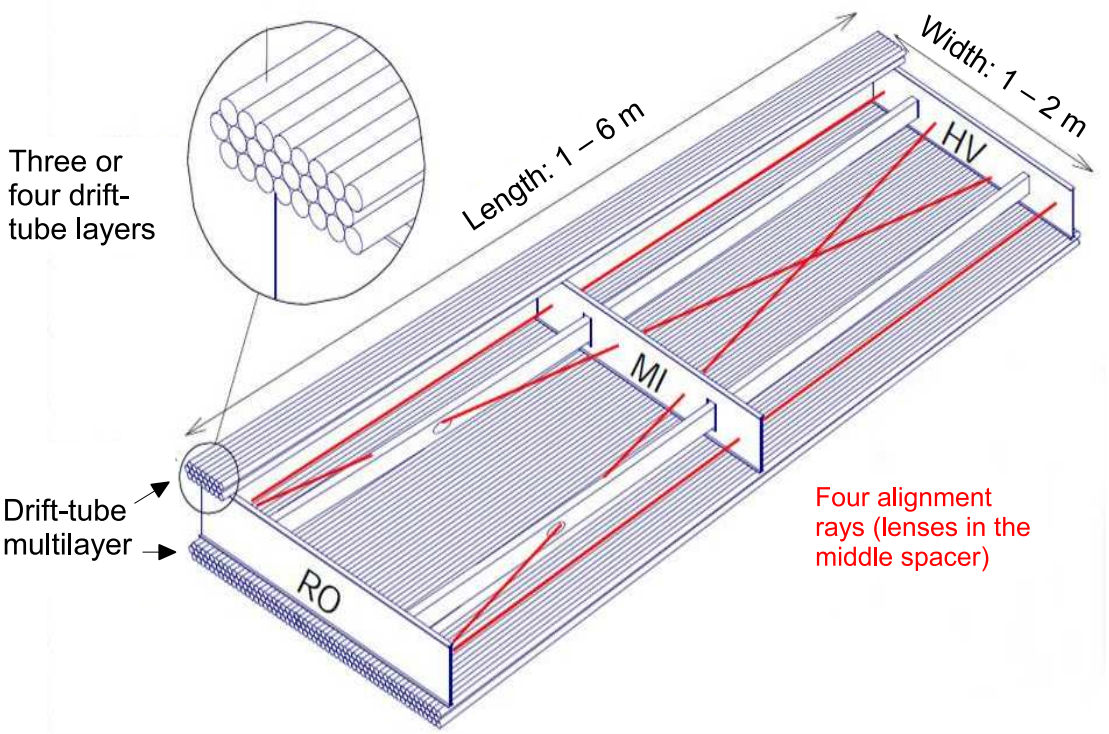

FIGURE 3.18: A schematic of an MDT chamber utilized at atlas. RO and HV correspond to read out and high voltage locations respectively [26]

separated by a 2mm gap filled with gas. When a particle impinges on the plates, the ionized charge flows between the dielectric plates which are subsequently read out by metal plates via capacitive coupling [26]. Figure 3.22 shows the layout of the RPC readout strips in relation to the dielectric inserted between the copper grounding plates. The RPCs also provide an additional measurement in the non-bending ϕ direction to complement the MDT measurement [26].

Thin Gap Chambers

The TGC serves a similar purpose to the RPCs. They are the magenta regions of Figure 3.21. TGCs and RPCs operate using similar physical processes but differ in the materials used [26]. The region of the TGC filled with gas is 2.8 mm wide. The gas mixture is CO_2 and n-pentane which results in a lower gas gain. The anodes are held at a potential of 2.9 kV. The operating parameters of the TGC allow it to

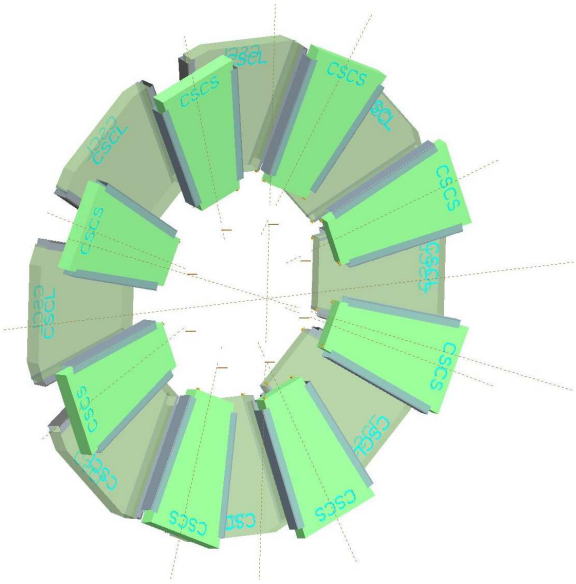

FIGURE 3.19: The geometry of CSC chambers at ATLAS [26].

read out signals within 25ns [26]. Figure 3.23 shows a schematic of a TGC module at ATLAS.

3.2.4 Track and Vertex Reconstruction

Track reconstruction at ATLAS relies on a variety of strategies to determine the best set of track parameters to describe the momentum of the charged particles passing through the inner detector and muon spectrometer [28]. Broadly speaking, track reconstruction starts using an "inside-out" approach beginning with information from the pixel detector, ambiguity resolution of silicon hit information, extension to the TRT, and finally an "outside-in" approach beginning from the TRT working backward [28]. This ensures that processes which leave tracks in the outer parts of the detector but not in the innermost silicon layers still get reconstructed. Such processes are long-lived decays (e.g. K_s decays) or photon conversions (a photon pair-produces leaving two tracks in the outer detector volume) [28]. Vertex reconstruction occurs by iteratively following high-quality tracks back to a common point and assigning these tracks to a primary vertex. A χ^2 is formed and remaining tracks that are

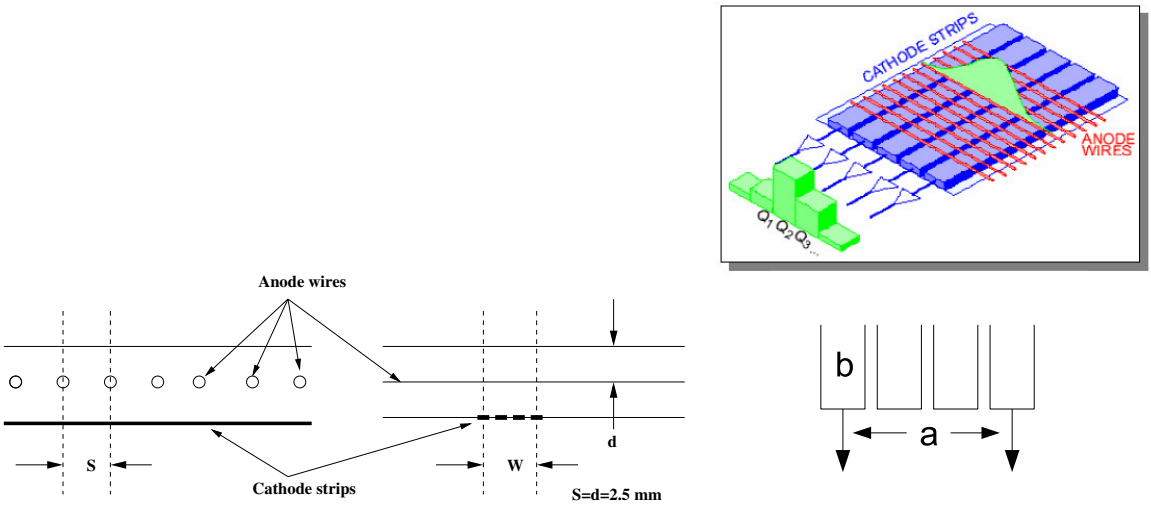

FIGURE 3.20: Left: Illustration of CSC cathode and anode wires, The anode width S is the same as the anode to cathode distance d. Right: Cathode strip width is $b = 1.519$ mm. The readout pitch $a = 5.308$ mm and 5.567 mm [26].

displaced more than 7σ from the primary vertex are considered for the next iteration of vertex searching. The process is repeated until no additional vertices can be found [59].

The actual estimation of track parameters is determined using a Kalman filter [28]. The Kalman filter works by iteratively updating the best estimate of the track parameters based on the addition of new measurements of the track parameters. It rapidly converges to the true result in the presence of noise and uncertainty in the measurement parameters [34]. These properties make it ideally suited for track reconstruction in the high-occupancy environment of ATLAS.

Inside-out sequence

The three-dimensional information of the silicon hits are used to seed the track reconstruction. Track seeds are created by applying a window search through the seed directions which are then fed to a simplified Kalman filter that creates an initial list of track candidates [28]. Figure 3.24 shows three tracks reconstructed during

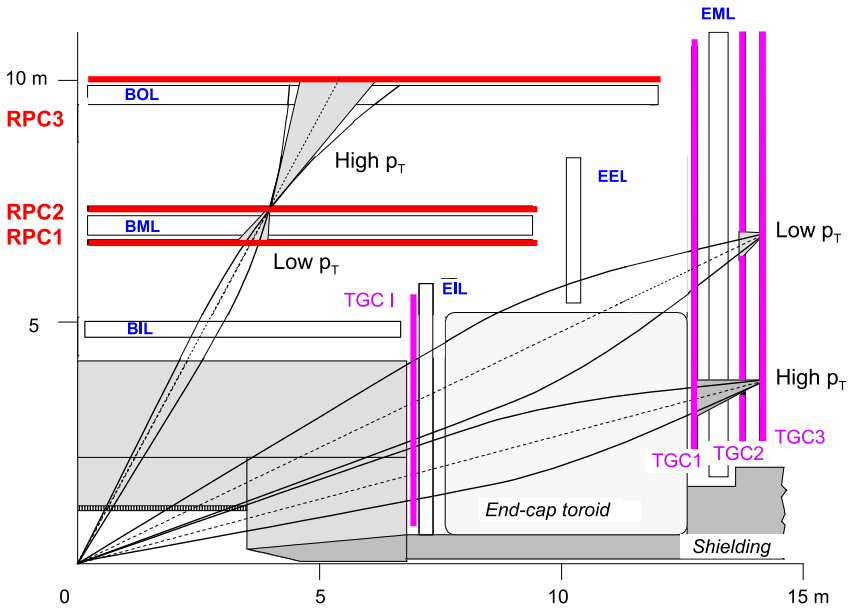

FIGURE 3.21: Layout of TGC and RPC chambers at ATLAS used to reconstruct muons [26].

track seeding. Hits associated to tracks that lead to better track quality are scored higher than those that do not. Similarly, poor quality hits are scored lower than high-quality ones. After resolving ambiguous hits the resulting tracks are extended into the TRT volume. TRT hits which lie along the reconstructed tracks are associated with each track. The software requires that adding TRT hits to the track does not modify the tracks extracted by the silicon hits of the previous steps [28]. Figure 3.25 shows the TRT extension procedure for a simulated $t\bar{t}$ event at ATLAS, red TRT hits are associated with the tracks reconstructed in the silicon layers. After TRT hits are associated with the tracks, the inside-out sequence is halted.

Outside-in sequence

There are a number of physical processes causing tracks that appear in the TRT to not be reconstructed during the inside-out reconstruction. These include long-lived decays as well as tracks that did not survive the ambiguity solving during the inside-out reconstruction. Hits not associated with tracks are considered in track

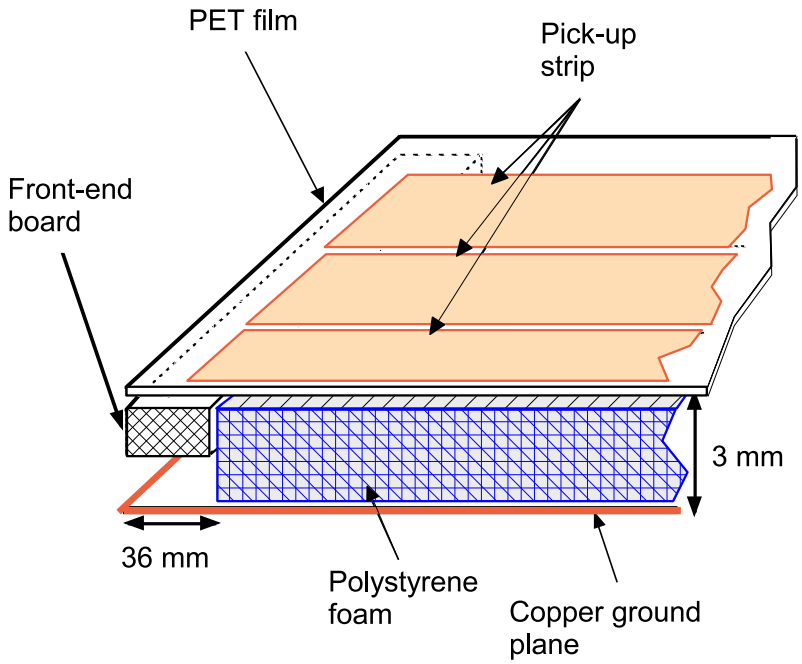

FIGURE 3.22: Schematic of the RPC readout strips [26].

finding and the resulting tracks are extended into the silicon to further associate hits to the tracks. Electrons lose significant amounts of energy in the TRT, which makes the gaussian assumption underlying the performance of the Kalman filter fail. Different pattern recognition techniques are used to reconstruct these tracks with a high efficiency [28].

Track Parameters

The track reconstruction algorithm as described does not make any reference to specific track parameters. The unique magnetic field that tracks traverse as they leave the detector makes a traditional helix parameterization difficult, therefore a generic set of parameters is defined at each measurement surface [57]

$$\mathbf{x} = (l_1, l_2, \phi, \theta, q/p). \tag{3.3}$$

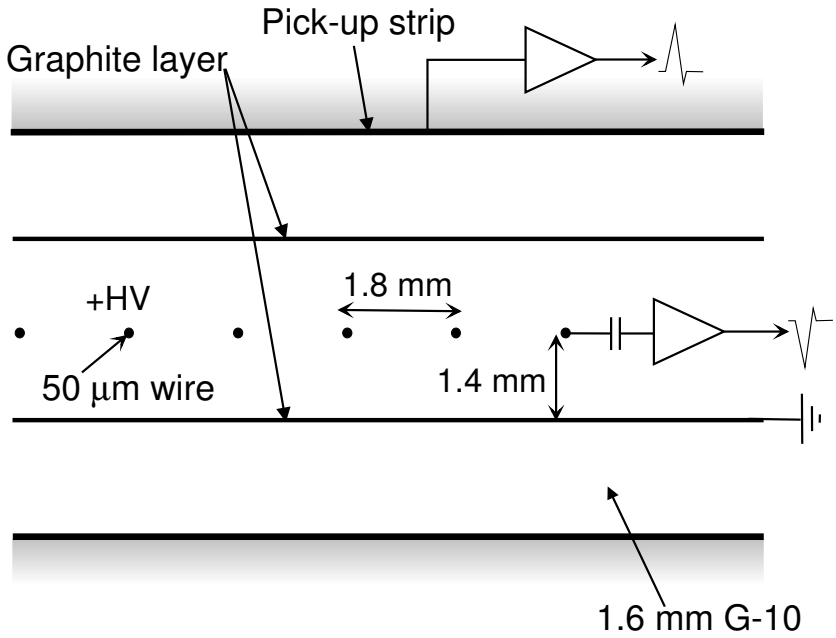

FIGURE 3.23: Schematic of the TGC layout. G-10 is a glass reinforced epoxy laminate [26].

The parameters l_1 and l_2 are local coordinates that depend on the surface in question. These local parameters are converted to the global kinematic parameters using ATLAS's definition of perigee parameters shown in Figure 3.26 [57]. The azimuthal angle ϕ and the polar angle θ are measured from the interaction point. The ratio q/p is measured based on the curvature of the track in the magnetic field. Figure 3.27 shows the magnetic field at ATLAS in the $r-z$ coordinates. The curvature of the track is determined by estimating the path a track takes as it traverses the field using finite element analysis of the field [57].

3.2.5 Trigger

At the design luminosity at the LHC, there are approximately 10^{18} interactions per second. The information describing each event takes 1.8 MB of disk space. The hardware available at the time of the construction of the LHC means that approximately 200 events could be written per second (i.e. a bandwidth of 2.6 GB/s)

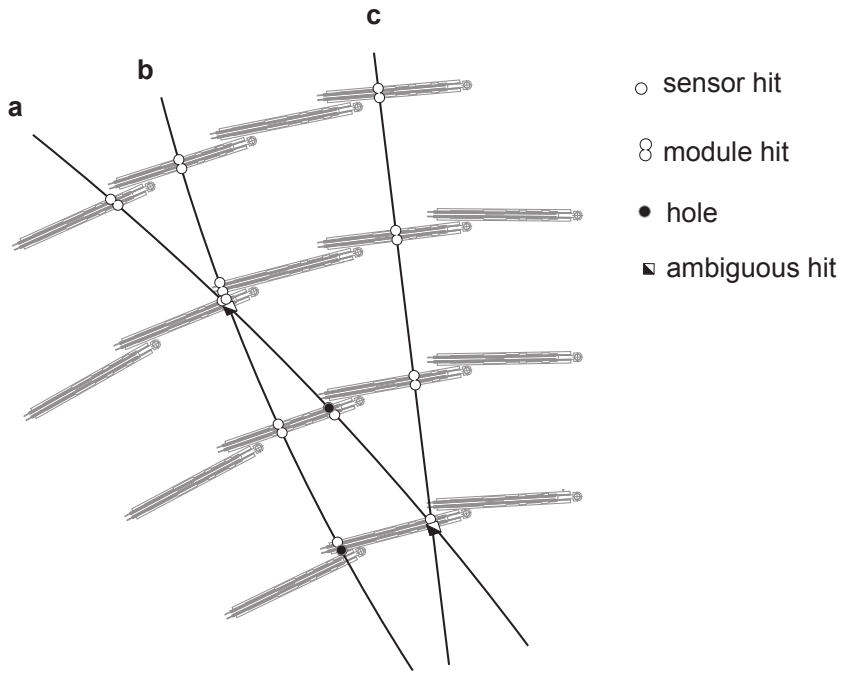

FIGURE 3.24: Example reconstruction of three tracks **a** **b** and **c**. Hits are scored to determine optimal association of hits to each track. [28].

[26]. A sophisticated system of hardware and software algorithms select events to be saved for further analysis. The entire system is referred to as the Trigger and Data Acquisition [26]. The trigger system drives the types of analyses that can be done as they are the first selection of which collision events are recorded.

The trigger is comprised of three levels, each considering more of the detector information than the last, and each refining the estimates of the physics objects in the event. The first level, (L1) is implemented at the hardware level. The L1 uses the RPC and TGC chambers of the muon spectrometer and coarse information from the calorimeters for identification of τ leptons, electrons, jets, and missing transverse energy. The L1 accept rate is 75 kHz and the decision must reach the front end electronics in 2.5 μs. The L1 trigger also creates regions of interest (RoI) which identify locations in $\eta - \phi$ space for further consideration by the level 2 (L2) trigger

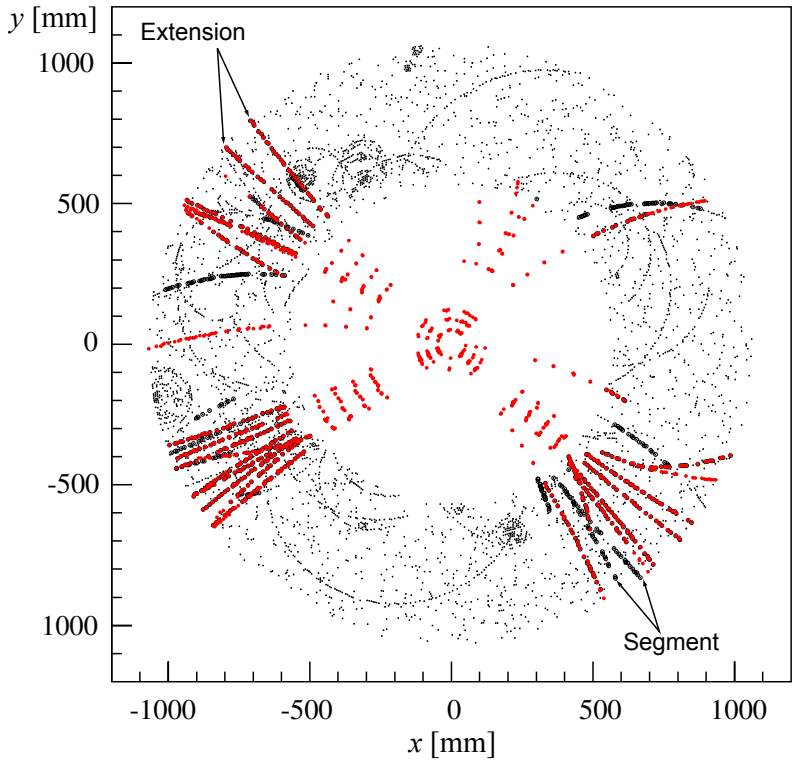

FIGURE 3.25: A simulated $t\bar{t}$ event illustrating the TRT extension procedure. Red TRT hits are associated with tracks represented by red hits in the silicon layers [28].

[26].

The L2 trigger and the event filter (EF) constitute the high-level trigger (HLT). The L2 trigger reduces the event rate to 2.5 kHz. The L2 trigger inspects the RoIs identified by the L1 trigger. The L2 trigger consists of a processing farm which runs partial event reconstruction in order to further refine the event rate. The output of the L2 trigger is passed onto the EF. The EF runs the full ATLAS reconstruction software on the event. A final decision is made on the reconstructed physics objects and these are written out to disk [26]. This analysis uses the following trigger chain: `L1_MU15` $\rightarrow$ `L2_mu36_tight` $\rightarrow$ `EF_mu36_tight`. The L1 trigger requires a roughly identified muon with $p_T > 15$ GeV. The L2 and EF triggers require a muon with $p_T > 36$ GeV. There are low p_T dimuon triggers available for J/ψ reconstruction but

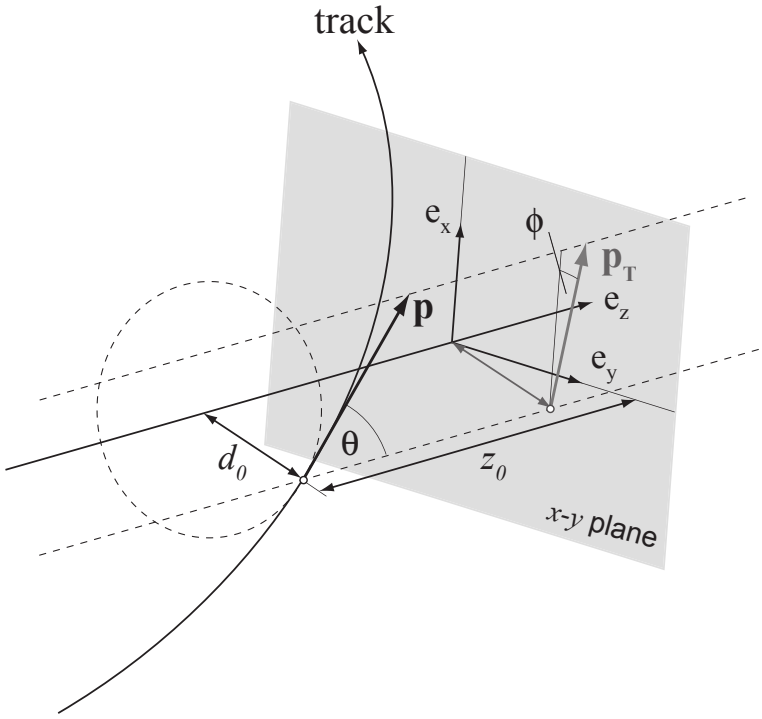

FIGURE 3.26: Perigee definition used by ATLAS [57].

they degrade in efficiency at the high p_T explored by this analysis [49].

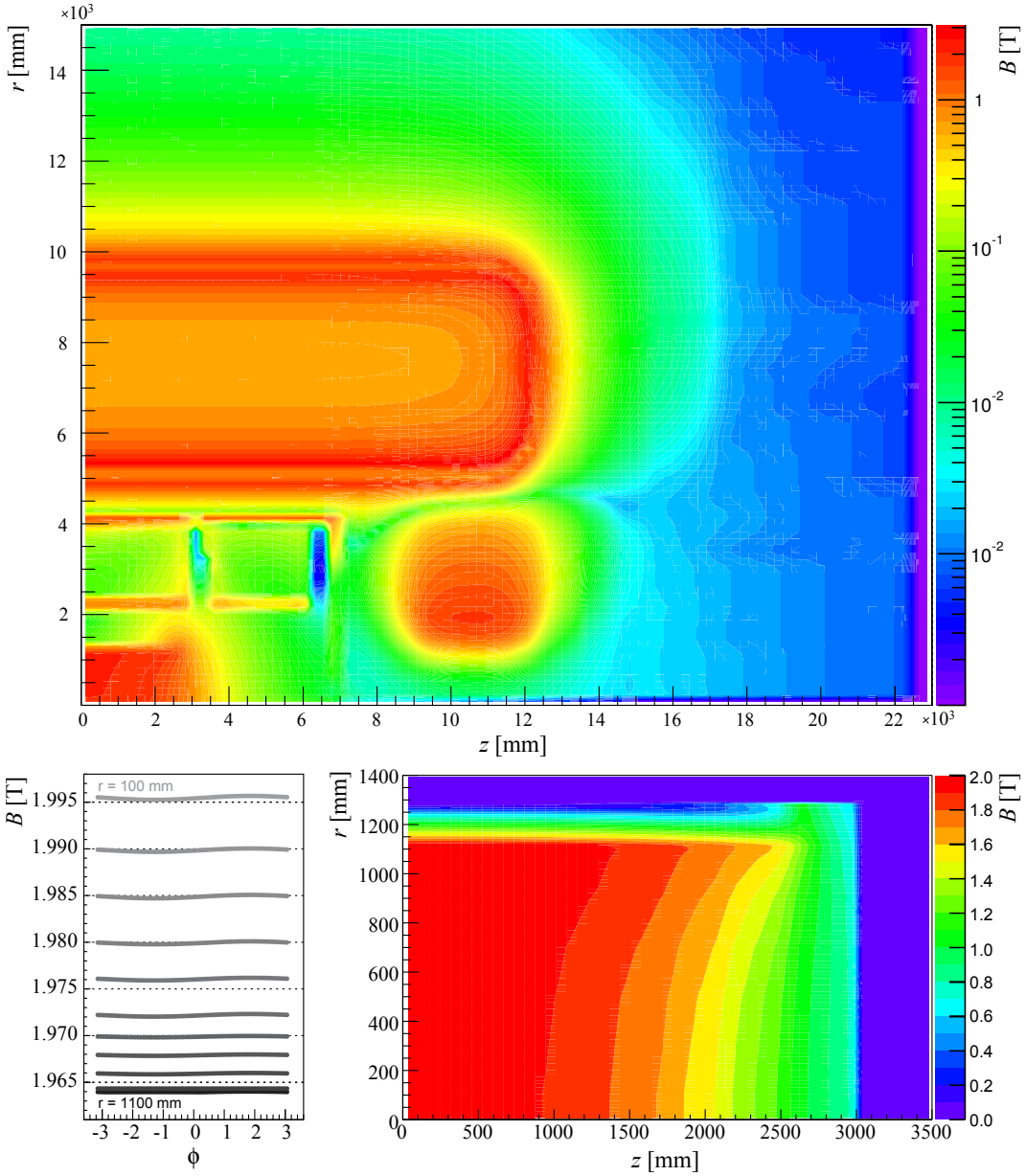

FIGURE 3.27: The magnetic field at ATLAS in the $r-z$ coordinate plane. The toroidal field is shown in the upper plot. The bottom left plot shows how uniform the field is in the azimuthal direction. The y axis shows the strength of the magnetic field while the shade of gray represents the radial coordinate. The bottom right plot shows a zoomed in view of the solenoidal field in the inner detector [57].

4

Event Reconstruction and Selection

4.1 J/ψ reconstruction

In Chapter 2 the J/ψ particle is understood as a quarkonium state consisting of a charm and an anti-charm quark. After the pair is produced, it rapidly decays to either hadrons, a pair of electrons or a pair of muons (see Table 4.1) [47]. In order to decay to pairs of leptons, the quark pairs must decay through a virtual photon (electromagnetically). If the final state is a parton, the pair can decay through a gluon (via the strong interaction) or a virtual photon. This leads to the relative size of the electron and muon contribution to the decay modes.

J/ψ Decay Mode	Fraction
hadrons	87.7 ± 0.5 %
e^+e^-	5.971 ± 0.032 %
$\mu^+\mu^-$	5.961 ± 0.033 %

Table 4.1: Summary of J/ψ decay modes [47]

While the rate of J/ψ decaying to muons is around 6%, it represents a very clean experimental signal. One of the major design requirements of ATLAS is the accurate reconstruction of muons across a wide momentum range.

Events which contain a high p_T muon are inspected for J/ψ candidates by checking for additional muons in the event. If there are two oppositely charged muons in the event, they are considered as a J/ψ candidate by refitting the tracks to a common vertex. This process modifies the track momentum slightly to more accurately reflect the hypothesis that the pair originated as a J/ψ. Figure 4.1 illustrates this process. When a pair of muons is identified as a J/ψ candidate, those muons are removed from the inner detector track collection considered by the jet reconstruction algorithm. After event reconstruction, the J/ψ candidate is required to have $p_T > 45$ GeV, and an absolute rapidity $|y| < 2.0$. Each muon must be central to the detector with $|\eta| < 2.5$. Finally, the invariant mass of the dimuon pair is required to be greater than 2.6 GeV and less than 4 GeV.

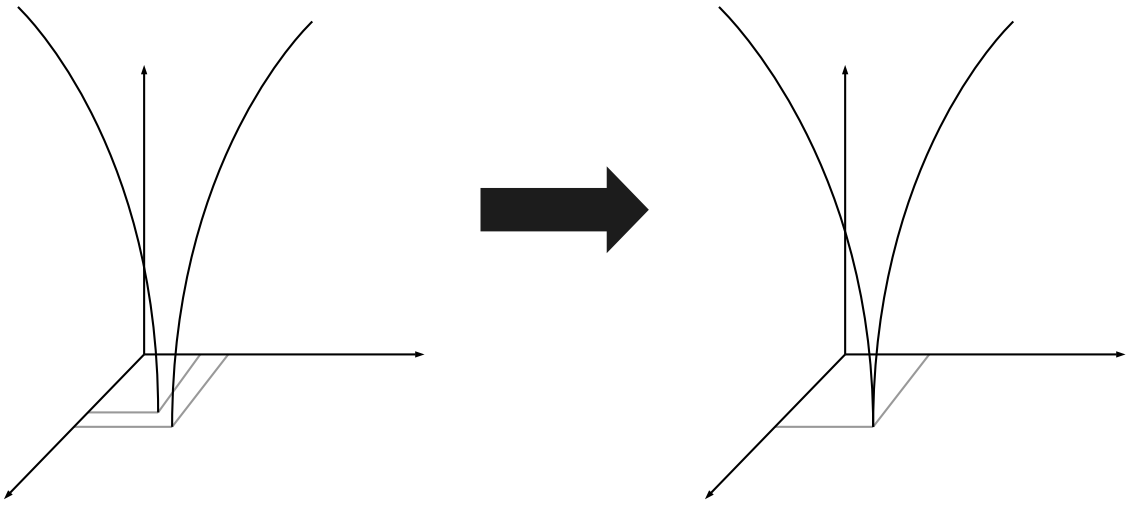

FIGURE 4.1: Illustration of how refitting oppositely charged tracks to a common vertex changes the track.

When a meson containing a b quark is produced, the b quark may change flavor to a c quark through the weak force. The time it takes to complete this process is quite long which allows the experimental discrimination of events containing a b quark. The long lifetime of b flavored mesons means that the decay vertex is displaced from the primary vertex. By measuring the distance between the refitted vertex and the

primary vertex of the event, an estimate of the lifetime of the particle can be made. Events which are displaced are referred to as non-prompt, while events which are not displaced are referred to as prompt. The lifetime can be estimated by measuring the displacement vector from the primary vertex ($\mathbf{L}$) and projecting it on the transverse momentum vector ($\mathbf{p}_T$). This quantity is referred to as L_{xy} [1]. Determining the pseudo-proper lifetime is then a matter of scaling this quantity by the ratio of the mass and transverse momentum of the particle[2]:

$$L_{xy} = \frac{\mathbf{L} \cdot \mathbf{p}_T}{p_T} \tag{4.1}$$

$$c\tau = \frac{M_{J/\psi}}{p_T(\mu\mu)} L_{xy} \tag{4.2}$$

Figure 4.2 shows the geometric definition of these quantities.

The lifetime distribution breaks down as follows:

- A large fraction of signal events will be centered around $c\tau = 0$
- A small fraction of events will contribute to a non-coherent component with an exponential decay positive and negative in $c\tau$
- A large fraction of background events will follow an exponential decay with a lifetime equal to the geometric mean of the B hadron lifetimes that contribute to the overall background.

It is possible that two oppositely charged muons are produced near enough to each other that they are refit as a J/ψ candidate without originating from a $c\bar{c}$ pair. Since these events come from the wrong combination of muons, they are referred to as the combinatoric background. The invariant mass of these muon pairs does

[1] Recall the transverse plane (T) is the $x - y$ plane in the cartesian coordinates used by ATLAS where the beam line is the z axis.

[2] In the high energy limit, the relativistic gamma factor is proportional to the ratio p_T/m.

not produce a resonance near the mass of the J/ψ the way muons from J/ψ decays do. This makes the invariant mass $M_{\mu\mu}$ the variable which discriminates true J/ψ candidates from the wrong combination of muons.

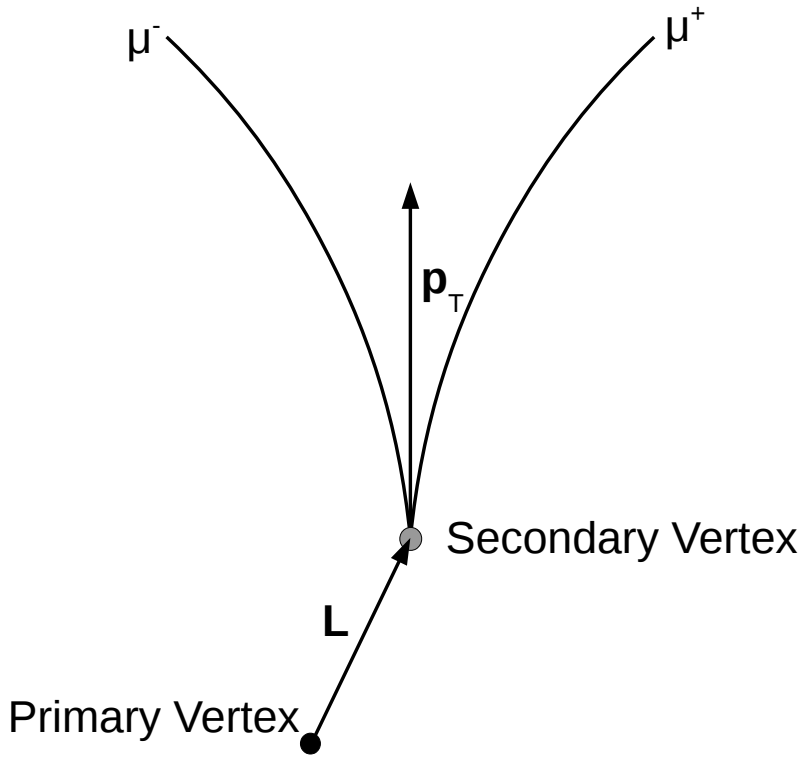

FIGURE 4.2: The definition of the pseudo-proper lifetime is derived from the signed projection of the distance between the primary vertex and the secondary vertex.

4.2 Jet definitions

In Chapter 2 the discussion of jets ended with the hadronization of partons to be reconstructed by the detector. This section describes how the detector level objects are grouped together to form candidates which represent the originating parton in those interactions. When a single hard parton showers and subsequently hadronizes, the QCD radiation emitted is typically collinear with the parton. This results in hadrons which are collimated in the detector.

A rigorous jet definition simultaneously captures the momentum of the parton before the parton shower and has a well-defined prescription for associating detector level objects to the jet [56]. Two critical properties of such an algorithm are infrared safety and collinear safety. Infrared safety means that adding soft (low momentum) radiation to the event doesn't change the reconstructed jets. This is illustrated in Figure 4.4. Collinear safety means that if a single hard particle is split into a collinear pair, the reconstructed jets remain the same as illustrated in Figure 4.3 [56].

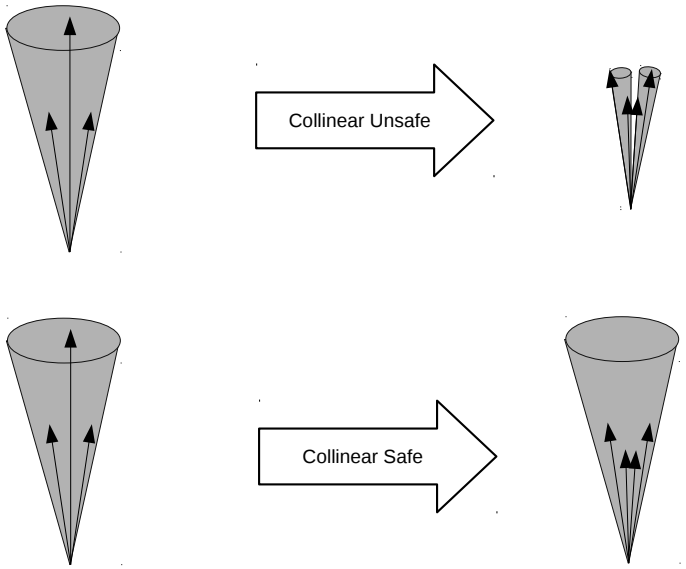

FIGURE 4.3: Collinear safety means splitting one hard momentum vector into two does not change the jets reconstructed by the algorithm.

4.2.1 Jet Reconstruction

There are many reconstruction algorithms that satisfy the conditions outlined above. The algorithm used in this work is the anti-k_t algorithm, a sequential recombination algorithm widely used in modern high energy physics experiments. Sequential recombination algorithms operate in the following steps:

1. A list of the pseudo-jet's momentum are provided as input (on the first step

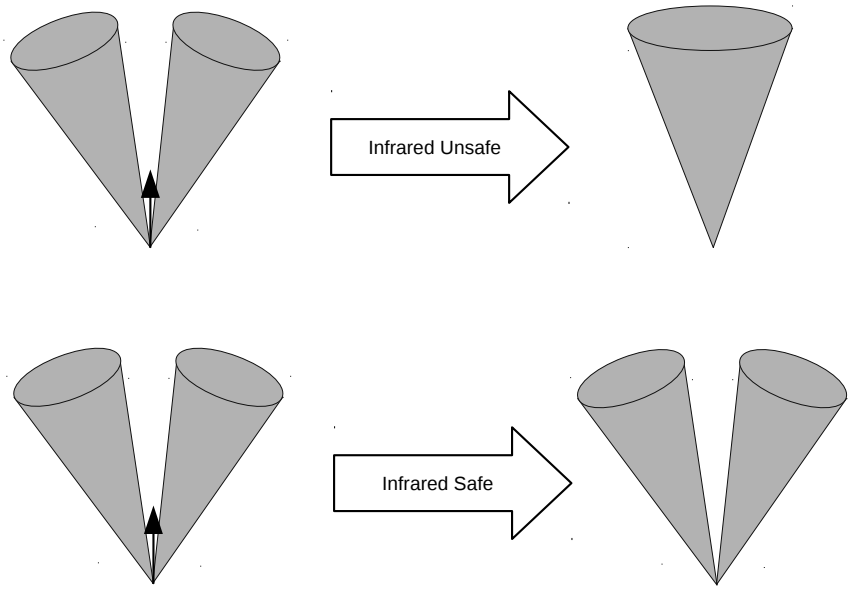

FIGURE 4.4: Infrared safety means adding a soft particle to the list of particles does not change the jets reconstructed by the algorithm.

this is a list of the reconstructed particle's momentum)

2. For each pseudo-jet i a quantity d_{ij} and d_{iB} is calculated where d_{ij} is a distance measure between the pseudo-jet i and another pseudo-jet j. The quantity d_{iB} is the distance between the pseudo-jet and the beam.

3. The minimum of d_{ij} and $\mathrm{d_{iB}}$ is determined. If d_{ij} is smaller, the two momenta i and j are combined to form a new pseudo-jet. If d_{iB} is smaller, this pseudo-jet is considered as a jet and removed from the list of pseudo-jets.

4. Steps 1-3 are repeated until no pseudo-jets remain.

In the anti-k_t algorithm the distance measure is defined as:

$$d_{ij} = \min(k_{ti}^{-2}, k_{tj}^{-2}) \frac{\Delta_{ij}^2}{R^2} \tag{4.3}$$

$$d_{iB} = k_{ti}^{-2} \tag{4.4}$$

Here $\Delta_{ij}^2 = (y_i - y_j)^2 + (\phi_i - \phi_j)^2$, k_t, ϕ, and y being the transverse momentum, azimuthal angle and rapidity of the pseudo-jet four vector respectively [24]. The parameter R is the predetermined radius of the jets. For this work $R = 0.4$ is used. Anti-k_t produces circular jets as opposed to other sequential recombination algorithms. Figure 4.5 shows the anti-k_t clustering for a three-jet event.

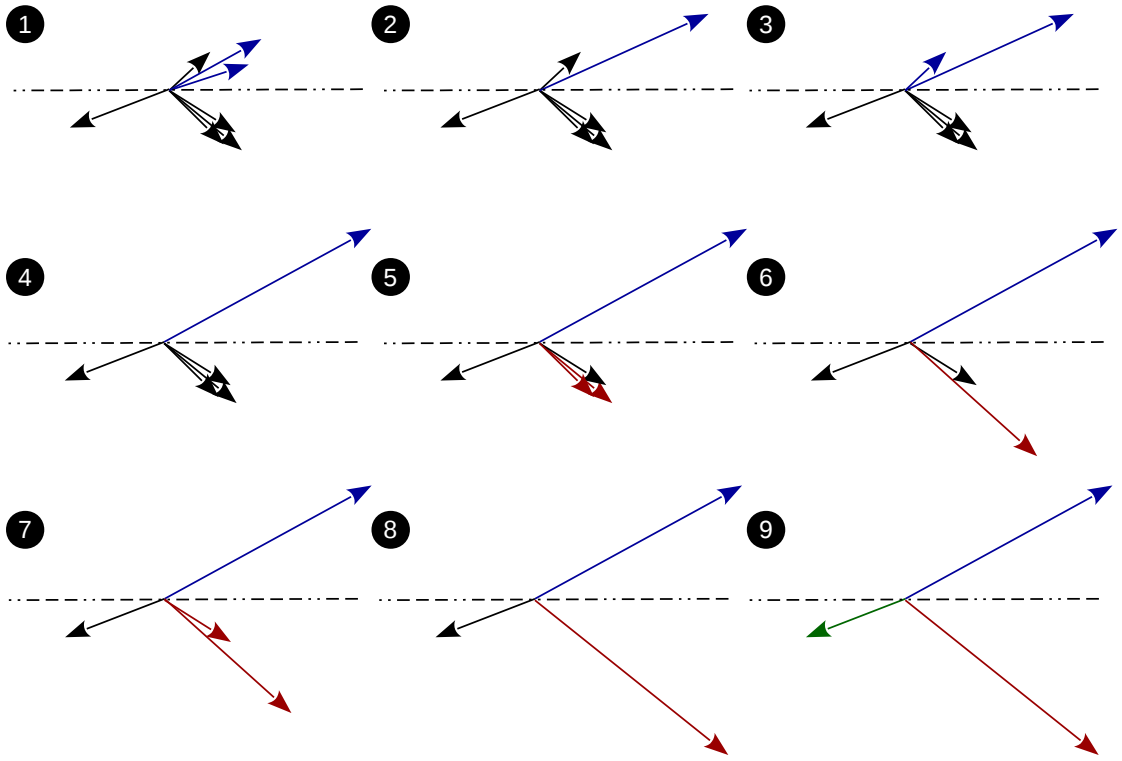

FIGURE 4.5: Illustration of the anti-k_t algorithm. Each step clusters a new particle until a jet is formed and clustering continues until no pseudo-jets remain.

Jets in this analysis are reconstructed with the anti-k_t clustering scheme using inner detector tracks as the pseudo-jets. In order to correctly capture the dynamics of the radiation environment around the J/ψ, the muons associated with the reconstructed J/ψ are removed from the list of tracks considered for jet reconstruction. In place of these tracks, the J/ψ four vector is added. This provides as accurate a representation of the charmonium and the embedded radiation as possible. The

tracks considered in reconstruction must be high quality. In order to achieve this, they must have a minimum p_T of 500 MeV, a maximum absolute pseudo-rapidity, $|\eta| < 2.5$, at least one hit in the pixel detector and 6 SCT hits. Finally, the fit χ^2 must be at most 3. Impact parameter cuts (see Figure 3.26) $z_0 \sin(\theta) < 1.5$ mm and $d_0 < 1.0$ mm are also applied. These cuts increase the quality of the selected tracks. The final set of jets that are reconstructed must be central to the detector $|\eta| < 2.5$ and must have high transverse momentum $p_T > 45$ GeV. Finally, the J/ψ and the jet must be within $\Delta R < 0.4$ (the reconstructed jet radius).

4.3 Observables

At this point, it is useful to introduce the observables used in this analysis. There are two: z and ΔR. The first, z is the momentum fraction shared between the J/ψ and the reconstructed jet. The momentum fraction is defined as:

$$z = \frac{p_T(J/\psi)}{p_T(\text{Jet})}. \tag{4.5}$$

As a reminder, the jet is clustered to include the J/ψ four-vector. As a result, the momentum fraction exists in $0 < z \leq 1$. This fraction directly probes the energy carried by the J/ψ compared to the surrounding radiation which is assumed to result from the parton shower. A value around $z = 0.5$ indicates that the p_T of the J/ψ and the $\mathrm{p_T}$ of the surrounding radiation are equal. A value of $z \simeq 1$ indicate that all the momentum is carried by the J/ψ and very little in surrounding radiation. Similarly a z value near zero indicates all the is momentum carried in the radiation within an $R = 0.4$ cone of the reconstructed J/ψ[3].

The second variable examined by this analysis is the angular separation between

[3] This is very unlikely to happen due to the high p_T requirement of the J/ψ.

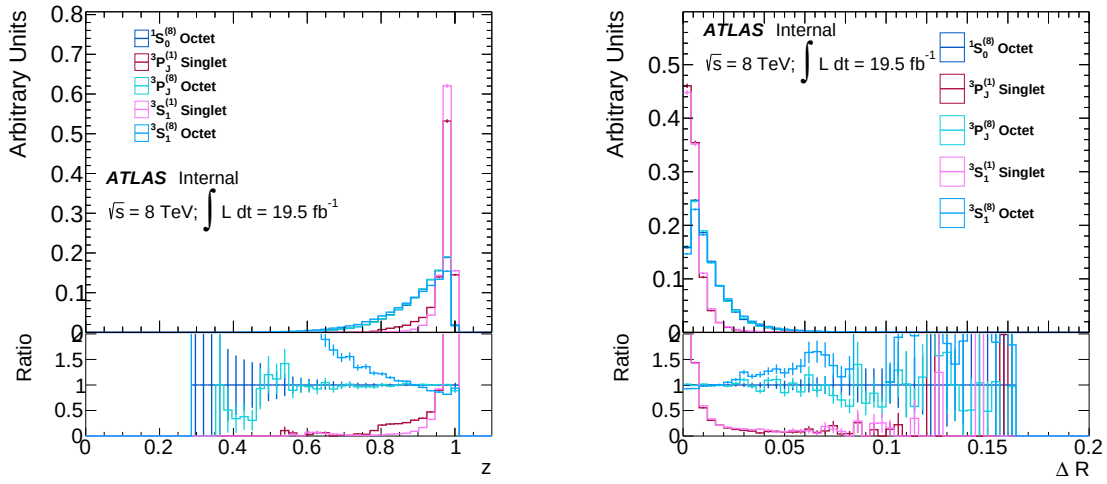

(a) z (b) ΔR

FIGURE 4.6: Pythia 8 prediction of each production mechanism for z and ΔR observables. The lower panel shows the ratio of each sample to the ${}^1S_0^{(8)}$ process in order to show the similarity between the other octet processes and the difference between the singlet processes.

the J/ψ and the reconstructed jet. This quantity, denoted ΔR, is defined as:

$$\Delta R = \sqrt{\Delta\phi^2 + \Delta\eta^2}. \tag{4.6}$$

If the radiation emitted around the J/ψ is isotropic in $\phi - \eta$, then the ΔR between the J/ψ and the reconstructed jet should be $\Delta R = 0$. The more the production of the $c\bar{c}$ system depends on the fragmentation of partons, the more likely the ΔR measurement will be peaked away from $\Delta R = 0$. Put another way, no radiation activity around the J/ψ will correspond to $\Delta R = 0$. A large amount of radiation around the J/ψ increases the chance that hard emissions change the alignment of the J/ψ to the surrounding radiation. Figure 4.6 shows Pythia's prediction of z and ΔR for the singlet and octet components available for simulation [58].

5

Analysis Methods

5.1 Likelihood Formalism

The maximum likelihood (ML) fit method is a statistical method for estimating parameters which describe the probability density function (PDF)[1]. The PDF can be motivated by physical first principles or empirically. The likelihood function is defined as the probability of a set of parameters given observed data. Maximizing the likelihood function with respect to these parameters provides a best estimate of the parameters. The likelihood function is constructed as a product over probability functions for observing a random variable x [19]

$$\mathcal{L} = \prod_{i=1}^{N} p(x_i|\boldsymbol{\theta}). \tag{5.1}$$

Here N is the number of observed events and $\boldsymbol{\theta}$ is a vector of parameters which describe the PDF[2]. It is important to note that the parameters θ_i do not represent a conditional probability. Instead, they are parameters of a function describing the

[1] This section follows the notation in [41] which differs slightly from the notation used in literature.

[2] For example, in the function of a line $p(x|m,b) = mx + b$, the slope (m) and intercept of a line (b) are parameters of the variable x.

PDF, independent of the random variable observed (x_i). Each probability function $p(x|\boldsymbol{\theta})$ is normalized [19]:

$$\int p(x|\boldsymbol{\theta})dx = 1. \tag{5.2}$$

Rather than maximizing the likelihood directly, it is easier to maximize (minimize) the (negative) logarithm of the likelihood,

$$-\log \mathcal{L} = -\sum_{i=1}^{N} \log(p(x_i|\boldsymbol{\theta})). \tag{5.3}$$

Equation 5.3 is minimized over the parameters θ_j. The value of these parameters represent the estimation of the PDF that most likely describes the observed data, hence the name "maximum likelihood fit." The computational framework that allows the use of the ML fit is RooFit, a general purpose statistical tool for performing and evaluating fits to data [63]. The algorithm used by RooFit to perform the minimization is a gradient descent called Minuit [40].

5.1.1 Extracting the Signal

The likelihood method provides a powerful tool for assessing the likelihood that a particular event is signal or background depending on the parameters extracted from the fit. The technique used for this purpose is called sPlot [50]. This method utilizes properties of the extended likelihood formalism to derive a set of weights representing categories parametrized by the PDFs used in the ML fit. SPlot requires that the normalization condition of equation 5.3 be relaxed such that for a given component of the likelihood function [19],

$$\int P(x|\boldsymbol{\theta})dx = N(\boldsymbol{\theta}). \tag{5.4}$$

This allows the re-expression of the negative log-likelihood function as [50]

$$-\log\mathcal{L} = -\sum_{i=1}^{N}\log(\sum_{j=1}^{\mathcal{N}_s} N_j p_j(x_i|\boldsymbol{\theta})). \tag{5.5}$$

In this expression $\mathcal{N}_s$ is the number of species (in this case, signal or background) to be separated, N_j is the number of the j^{th} species and p_j is the PDF describing the j^{th} species. SPlot also requires knowledge of the covariance matrix. This is can be estimated from the likelihood function by [50]

$$V^{-1}(\hat{\boldsymbol{\theta}})_{ij} = \frac{\partial^2(-\mathcal{L}(x|\boldsymbol{\theta}_0))}{\partial N_i \partial N_j}, \tag{5.6}$$

here $\boldsymbol{\theta}_0$ are the parameters estimated from the ML fit. With these ingredients it is possible to derive the weights required to reconstruct a histogram of the estimated signal. The expression obtained is

$$W_S(x) = \frac{\sum_{j=1}^{N_s} V_{Sj} p_j(x)}{\sum_{k=1}^{N_s} N_k p_k(x)}. \tag{5.7}$$

The matrix V_{ij} is obtained from the likelihood function by numerically inverting equation 5.6. It is informative to expand this expression for the case of two species, signal and background as used in this analysis. For the case of signal the weight is

$$W_S(x) = \frac{V_{SS} p_S(x) + V_{SB} p_B(x)}{N_S p_S(x) + N_B p_B(x)}. \tag{5.8}$$

In this expression it is clear that the weight depends on the PDF for the signal and background and is weighted by the covariance of these two components. In the extreme case where signal and background are perfectly separated the covariance matrix is diagonal and the weight reduces to

$$W_S(x) = \frac{\sigma_S}{N_S p_S(x) + N_B \frac{p_B(x)}{p_S(x)}}, \tag{5.9}$$

where σ_S is the variance of the signal PDF. In this reduced case, a small probability of signal leads to a small weight. Conversely, a large probability of being signal (and a small probability of being background) gives a large weight. This weight is applied per event and on average it reproduces the signal histogram.

5.2 Empirical Model

In Section 4.1 the two sources of background were introduced: non-prompt decays from B hadrons distinguished by the $c\tau$ distribution and combinatoric events from the wrong pair of muons distinguished by the invariant mass of the di-muon pair $M_{\mu\mu}$. The fit to the data is parameterized by a joint PDF in $M_{\mu\mu}$ and $c\tau$. The specific parameterization has been used previously to extract J/ψ events [46]. It is defined as:

$$PDF(m,t) = \sum_i f_i(m) \cdot h_i(t) \otimes g(t). \tag{5.10}$$

Here $\otimes$ is convolution while $\cdot$ is PDF multiplication. In the following $\oplus$ refers to a weighted sum of two PDF components such that the result remains properly normalized. The individual fit components are listed in Table 5.1. The function $g(t)$ is resolution function of the lifetime distribution. It is a double-gaussian and is convolved with each lifetime component. The choice of these specific functions and the

i	Source	$f_i(m)$	$h_i(t)$
1	Prompt J/ψ	$CB_1(m) \oplus G_1(m)$	$\delta(t)$
2	Non-prompt J/ψ	$CB_1(m) \oplus G_1(m)$	$E_1(t)$
3	Prompt Background	$P^0(m)$	$\delta(t)$
4	Non-prompt Background	$P^1(m)$	$E_2(t)$
5	Non-coherent Background	$E_3(m)$	$E_4(\|t\|)$

Table 5.1: Individual components of simultaneous fit to data. Functions are notated as follows: $\delta(x)$, the dirac delta function; $CB_k(x)$, the kth Crystal Ball function; $G_k(x)$ a Gaussian function; $E_k(x)$, the kth exponential decay; $P^n(x)$ a polynomial of degree n. A function with the same k index shares the same free parameters.

components they model deserve explanation. The constructed PDF is a joint PDF

in $M_{\mu\mu}$ (denoted m in the fit) and $c\tau$ (denoted t in the fit). This means that each component must have a mass component and a lifetime component. The shape used for the J/ψ resonance in m is the sum of a Gaussian and a Crystal Ball function. The Crystal Ball has the shape of a Gaussian, but is asymmetric and allows the correct modeling of losses that give the resonance a low mass tail. The function is defined as:

$$f(m;\alpha,n,\mu,\sigma) = N \cdot \begin{cases} \exp\left(-\frac{(x-\mu)^2}{2\sigma^2}\right) & \text{for } \frac{x-\mu}{\sigma} > -\alpha \\ A \cdot \left(B - \frac{x-\mu}{\sigma}\right)^{-n} & \text{for } \frac{x-\mu}{\sigma} \leq -\alpha \end{cases}, \tag{5.11}$$

$$A = \left(\frac{n}{|\alpha|}\right)^n \exp\left(-\frac{|\alpha|^2}{2}\right), \tag{5.12}$$

$$B = \frac{n}{|\alpha|} - |\alpha|. \tag{5.13}$$

Here N is the normalization factor, μ is the mean and σ the width of the Gaussian portion. The parameters $n = 1$ and $\alpha = 10$ are fixed in the fit but varied in separate fits to assess their impact on the systematic uncertainty.

The signal component is defined as the prompt J/ψ component; the remainder is background. The non-prompt component shares the same mass signal PDF but has an exponential distribution in t. The remaining components of the PDF do not contribute to the estimate of real J/ψ events. The portion of events which appear prompt but are from the wrong combination of muons, a constant function in mass and a delta function in t are used. There is a portion of events which appear to have a negative lifetime depending on the measurement of L_{xy}. This component is modeled as a double-sided exponential in t and an exponential in m. The combinatoric background component is linear in m and exponential in t. Including fractions which float to ensure the PDF is normalized, the fit includes fourteen free parameters.

Figure 5.1a and Figure 5.1b shows the result of the simultaneous fit to the 2012

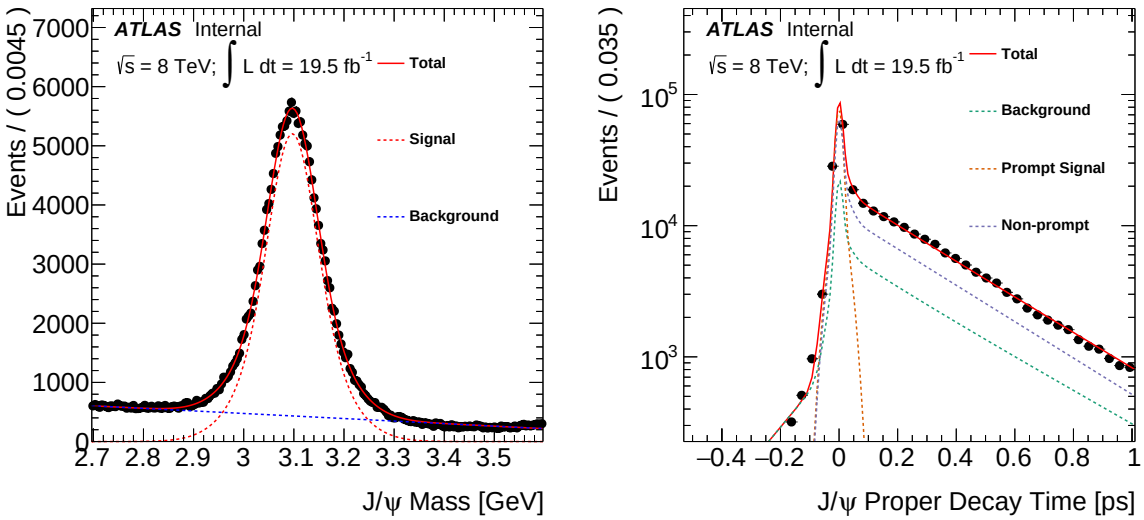

(a) $M_{\mu\mu}$ fit result

(b) $c\tau$ fit result

FIGURE 5.1: Result of unbinned likelihood fit to invariant mass distribution of dimuon pairs in data and pseudo-proper lifetime distribution. See 5.1 for a list of the fit components.

data set for the dimuon invariant mass distribution and pseudo-proper lifetime distribution respectively. Selected fitted values of the PDF are summarized in Table 5.2.

Parameter Name	Fitted Value
J/ψ Mass	3.0969 $\pm$ 0.0002 GeV
J/ψ Width	(0.82 $\pm$ 0.01)$\times$ 10^{-1} GeV
Lifetime	0.313 $\pm$ 0.001 mm
Non-coherent Lifetime	0.161 $\pm$ 0.003 mm
Non-prompt Lifetime	0.344 $\pm$ 0.002 mm
Resolution Width	(0.109 $\pm$ 0.001)$\times$ 10^{-1} mm
Second Resolution Width	(0.308 $\pm$ 0.005)$\times$ 10^{-1} mm
Non-Coherent Mass c_1	-0.2640 $\pm$ 0.0004 1/GeV

Table 5.2: Summary of fit to dataset with nominal parameterization. Estimated distance to minimum of negative log likelihood minimization: 0.84577$\times$ 10^{-3}.

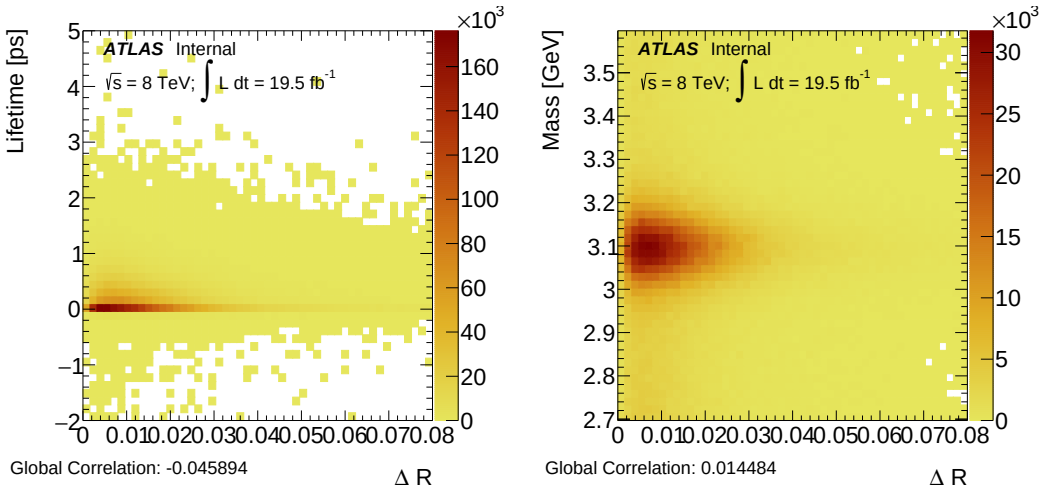

(a) ΔR vs lifetime (b) ΔR vs $M_{\mu\mu}$

FIGURE 5.2: Two-dimensional histogram of ΔR vs discriminating variables used to extract background component from sPlot method

5.2.1 Validating signal extraction

A fundamental assumption of sPlot is that the variable of interest (ΔR and z) is uncorrelated with the discriminating variables ($c\tau$ and $M_{\mu\mu}$). The 2D histograms of the interest variables versus the discriminating variables and their global correlation is shown in Figure 5.2 and 5.3.

In order to ensure the background extraction procedure is correctly estimating the shape, sideband regions are defined and compared to the sPlot estimate. Sideband regions are intervals of $c\tau$ and $M_{\mu\mu}$ where the background is expected to dominate the distribution. If these shapes roughly agree, then there is confidence that sPlot is correctly estimating the shape in the signal region. The non-prompt background region is defined as $3\sigma_{c\tau} < ct < 50$ mm where $\sigma_{c\tau}$ is determined from the simultaneous fit. The combinatoric background region is defined as more than $3\sigma_m$ where σ_m is the width of the fitted mass peak. Figure 5.4 shows the result of this comparison.

While this gives confidence that the background shape is estimated properly, it is useful to compare the signal shape of the transverse momentum distribution to

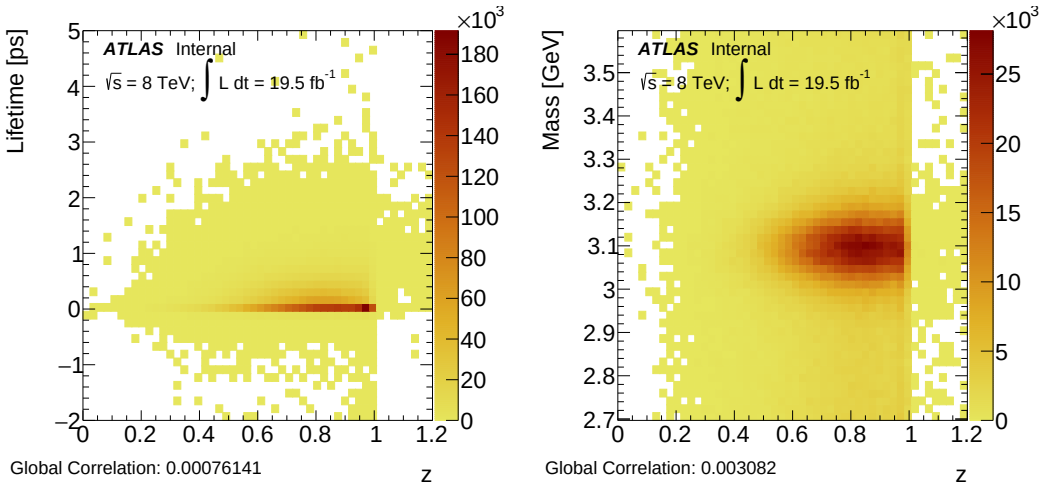

(a) Jet z vs lifetime (b) Jet z vs $M_{\mu\mu}$

FIGURE 5.3: Two-dimensional histogram of Jet z vs discriminating variables used to extract background component from sPlot method

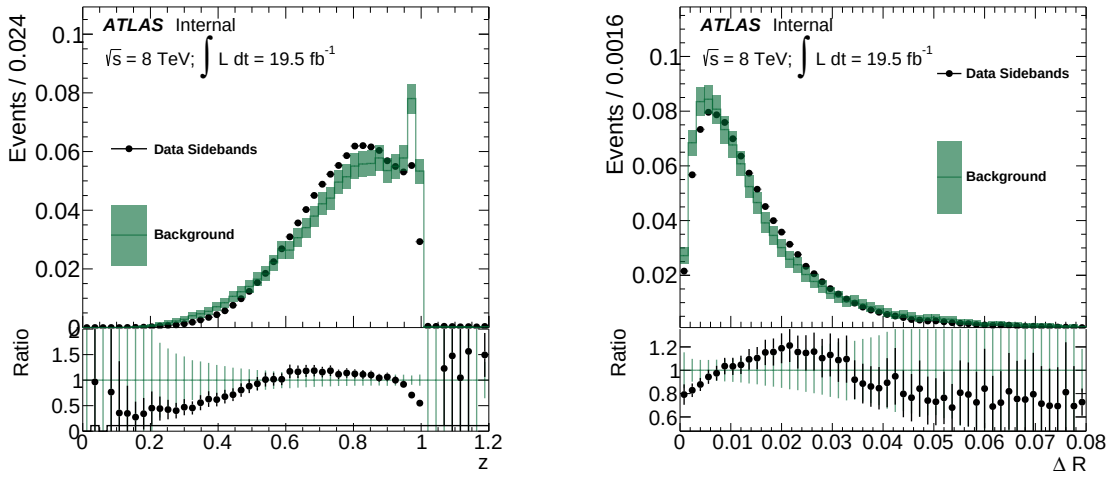

(a) z (b) ΔR

FIGURE 5.4: Background extracted from the sPlot method compared to the sideband regions for the jet momentum fraction z and the J/ψ jet separation ΔR

ensure that the Monte Carlo is correctly modeling this shape. The comparison of the reconstructed jet p_T and J/ψ p_T are shown in Figures 5.5a and 5.5c. In addition, Figure 5.5b and 5.5d show the sPlot estimations of the signal and background. It is expected that the non-prompt fraction increases with the J/ψ's p_T [46] which is observed in Figure 5.5d.

5.3 Unfolding

Implicit in the measurement of any quantity is the uncertainty associated with the measurement. There are systematic effects which may distort the true value of the quantity measured. The size of these effects is estimated through the assessment of systematic errors by varying the input and taking the difference from the nominal result. The finite resolution of the detector will distort the measured value relative to the true value in a random but consistent way [29]. It is the goal of unfolding to remove these types of effects. This problem goes under different names in different fields such as deconvolution or unsmearing [29].

In the case of a perfect detector, the number of events observed in a particular bin of a histogram will be given by a continuous probability distribution [29]

$$T_i = N \int_{x \in \text{bin}(i)} f(x) dx. \tag{5.14}$$

Here T is referred to as the truth histogram and $f(x)$ as the true probability distribution function. The factor N is the number of events observed in a particular experiment. The function bin(i) is a function which gives the interval in x for the given bin i. In reality the detector is not perfect, and the measurement will be distorted. If an event can occur without being detected, the efficiency of detection is less than one. This efficiency may vary with the observable, and so it is assigned a function $\epsilon(x)$. In this form the efficiency represents the probability of detection.

Incorporating the efficiency is a matter of multiplying the probability an event occurs by the probability of detecting it [29]

$$H_i = N \int_{x \in \text{bin}(i)} \epsilon(x) f(x) dx. \tag{5.15}$$

The label H is used to refer to what is actually observed as a result of an experiment with an efficiency. One final possibility remains: an event has a true value x and the detector measures its value to be y. This can be cast in terms of conditional probability as $P(y|x)$, which is read as "the probability of observing y given that the true value was x." The observed histogram becomes [29]

$$H_i = N \int_{y \in \text{bin}(i)} \int P(y|x) \epsilon(x) f(x) dx dy. \tag{5.16}$$

Note here the slight change in integration: the number of events observed in the i^{th} bin is given by the integral over all possible truth values multiplied by the probability to detect them, and the conditional probability that they are miss-measured with a value y.

It is useful to combine the detection efficiency and the probability the detector changes a measurement from its true value in one function, the response function [29],

$$r(y|x) = P(y|x) \epsilon(x). \tag{5.17}$$

In practice the integral over x in equation 5.16 is a sum over the bins in a truth histogram obtained from Monte Carlo simulations of the detector. In this case it is useful to consider the discrete case by applying the same method to determine the

truth histogram as in equation 5.14

$$H_i = \sum_{j=1}^{M} \frac{\int_{x\in \text{bin}(i)} \int_{y\in \text{bin}(j)} r(y|x) f(x) dy dx}{T_j/N} T_j, \tag{5.18}$$

$$= \sum_{j=1}^{M} R_{ij} T_j, \tag{5.19}$$

$$R_{ij} = \frac{\int_{x\in \text{bin}(i)} \int_{y\in \text{bin}(j)} r(y|x) f(x) dy dx}{T_j/N}. \tag{5.20}$$

The response[3] matrix R_{ij} is the conditional probability of observing an event in bin i given the true value was in bin j. When a true value is modified by the response function, it is "folded" to give the expected result of the experiment. The inverse process of determining the true value given the result of the experiment is referred to as "unfolding."

With the response matrix in hand, it is tempting to invert it and obtain a direct estimate of the truth

$$H_i = R_{ij} T_j,$$

$$T_i = R_{ij}^{-1} H_j.$$

The issue with this approach lies in the fact that the response matrix is estimated from Monte Carlo simulation and applied to the result of a measurement. The result of the measurement are subject to statistical fluctuations independent of those given in the estimate of the response. When the inverse response matrix is applied, these fluctuations are enhanced and overwhelm any physically meaningful shape that is recovered from the inversion [29].

It is the goal of any unfolding method to estimate the inverse of R_{ij} in a way that regularizes the fluctuations in the estimate of the truth caused by the statistical fluctuations in the experimental measurement. Bayes' theorem provides one way of

[3] The name response is given in the sense of how the detector "responds" to a given truth input.

performing an iterative procedure that allows an estimate of the truth distribution before the fluctuations grow too large to make conclusions useless.

5.3.1 Iterative Bayesian Unfolding

Bayes' theorem provides a way of "inverting" the conditions for a conditional probability. Using the notation above and assuming $\epsilon(y) \equiv 1$ [12][4], Bayes theorem is given as

$$P(x|y) = \frac{P(y|x)f(x)}{\int f(x)p(y|x)dx} \equiv \frac{P(y|x)f(x)}{g(y)}, \tag{5.21}$$

$$g(y) = \int f(x)p(y|x)dx. \tag{5.22}$$

here the correspondence that x is the true value and y is the measured value is made more explicit. This allows $f(x)$, the true distribution, to be estimated as

$$f(x) = \int g(y)P(x|y)dx. \tag{5.23}$$

The issue is that in plugging equation 5.21 into this definition of $f(x)$, shows the explicit dependence of $P(x|y)$ on $f(x)$. The way forward is to determine a first estimate of $f(x)$ and iteratively update it based on the estimate of $P(y|x)$ from simulations. If one starts after $k+1$ steps, the following can be written by iteratively applying Bayes' theorem,

$$f^{k+1}(x) = \int f^k(x)\frac{g_{\text{exp}}(y)}{g^k(y)}P(y|x)dy. \tag{5.24}$$

Here $g_{\text{exp}}(y)$ is the distribution obtained by the experiment. The denominator, $g^k(y)$, is the result of folding the k^{th} estimate of $f(x)$ with the response function $P(y|x)$. On each successive iteration, $g^k(y)$ will approach $g_{\text{exp}}(y)$ as long as $f^k(x)$ approaches the true value $f(x)$.

[4] This section follows the steps in [12] which is internal to ATLAS. The references therein are included here as well to allow access to the primary sources without access to the internal document.

The procedure can be stopped according to different criteria. In the case of this analysis, the number of iterations is determined ahead of time by unfolding a known truth distribution that has been folded with the estimated response matrix. When the value of Pearson's χ^2 between a known truth distribution and each iteration reaches a minimum, the procedure is halted and that number of iterations is used to unfold the data.

Estimating the Response Matrix

The response matrix is estimated from the truth information contained in Monte Carlo simulations of the signal process. For the purposes of estimating the detector's response to the signal process, all sub-processes are considered as signal (no distinction is made between singlet or octet in estimating the matrix). For a given set of events that pass the selection criteria at the detector level, a plot is made of the measured value by the simulated detector (referred to as "reconstructed"), and the value that was generated by the particles that were input to the detector simulation (referred to as "truth"). The result is a two-dimensional histogram whose axes range across the physical range of the variable. The ordered pair (truth, reconstructed) are plotted and the histogram bin these values fall into are accumulated. The resulting distribution is an estimate of the response matrix as defined in equation 5.20. In the limit of infinite simulated events, this histogram will converge to the PDF in equation 5.20.

Validating the Method

The crux of unfolding is to estimate an unknown truth distribution as accurately as possible using the incomplete description provided by the detector. In order to have confidence in the results, it is important to assess the method using controlled inputs. This is achieved by using a known truth distribution (a single gaussian

centered at the physical range) and folding it with the estimated response matrix to create a pseudo-reconstructed distribution. The unfolding procedure is applied to the pseudo-reconstructed distribution and it is compared to the truth distribution. If the truth distribution falls outside the physical range of the response matrix it is truncated. Therefore, the range of validity of the unfolded pseudo-reconstructed distribution is the physical range covered by the response matrix. Figures 5.6 and 5.7 show the estimated response matrix and the unfolding validation test for the z and ΔR distributions respectively.

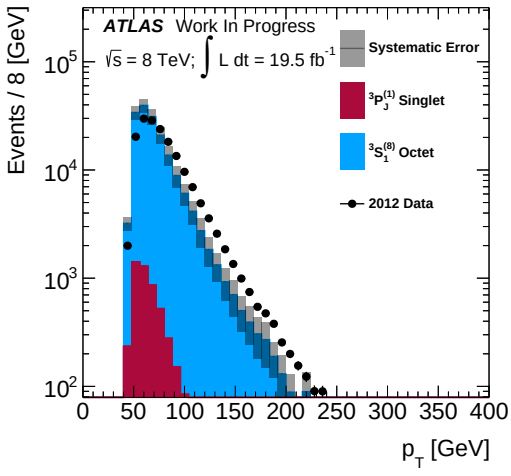

(a) Data vs Pythia Jet p_T

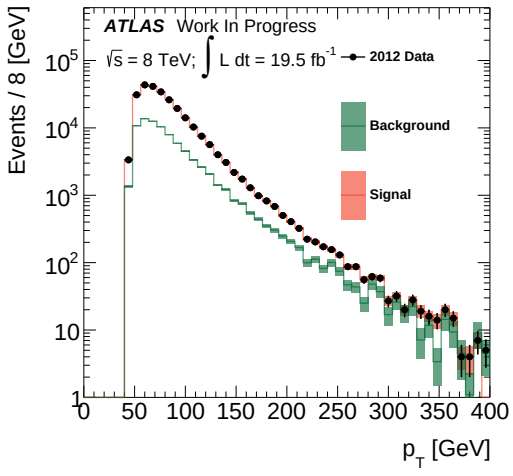

(b) Signal and Background, Jet p_T

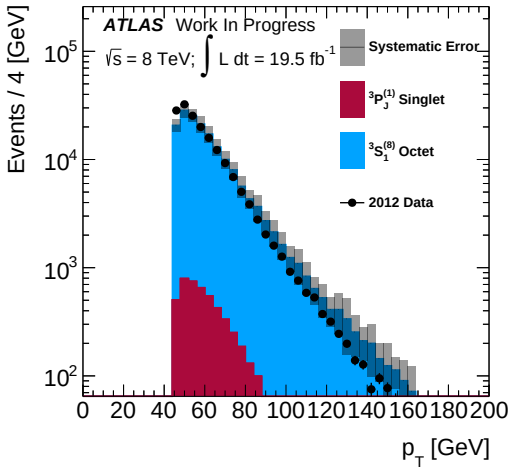

(c) J/ψ p_T

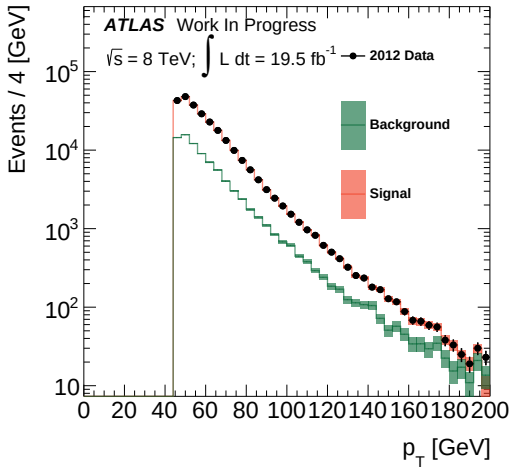

(d) Signal and Background J/ψ p_T

FIGURE 5.5: Transverse momentum distributions of the J/ψ and matched jet compared to the Pythia prediction (red for singlet, blue for octet, left panel). Signal (orange) and background (green) compared to data (right panel).

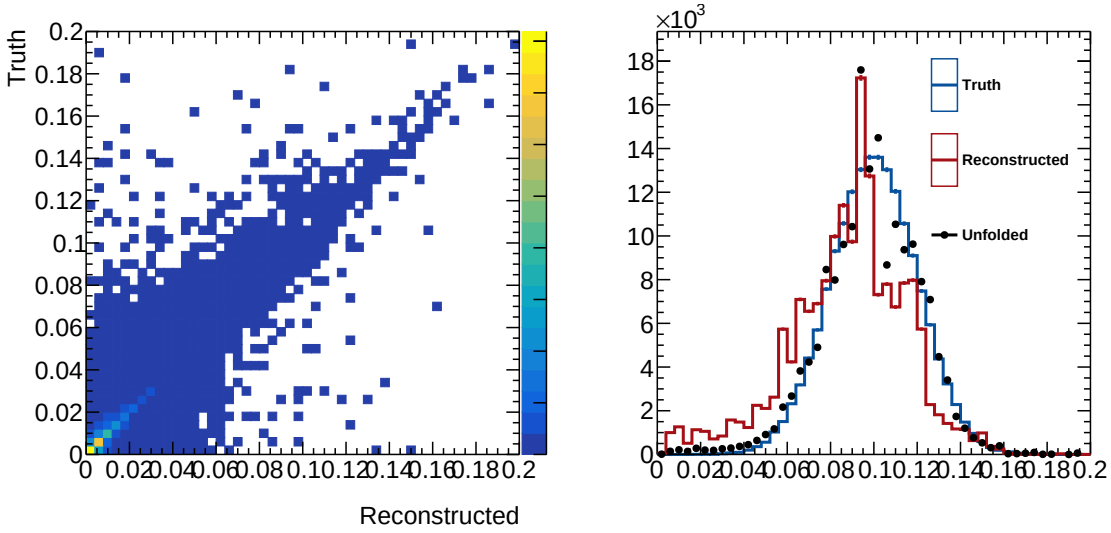

FIGURE 5.6: Double gaussian unfolding test of ΔR response matrix

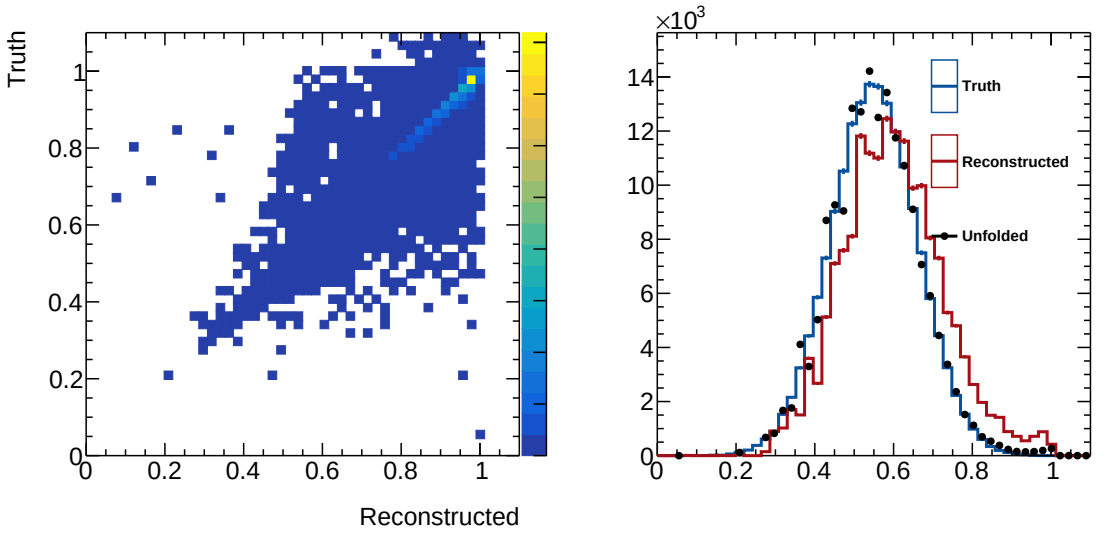

FIGURE 5.7: Double gaussian unfolding test of z response matrix

6

Measurement of prompt J/ψ particles

6.1 Data sets

Monte Carlo samples are used to validate the fit to data, estimate the response matrix, and derive the systematic errors for comparing to data. The samples used to model the signal and non-prompt background sources are listed in Table 6.1.

Process	Cross Section [fb]
$c\bar{c}(^3S_1^{(8)}) \to J/\psi$	8260
$c\bar{c}(^3P_J^{(1)}) \to J/\psi$	587
$c\bar{c}(^3P_J^{(8)}) \to J/\psi$	15.6
$c\bar{c}(^1S_0^{(8)}) \to J/\psi$	12.5
$c\bar{c}(^3S_1^{(1)}) \to J/\psi$	0.307

Table 6.1: Monte Carlo samples used and their simulated cross section. Each $c\bar{c}$ sample consists of 10^5 events.

Data is collected at the LHC in units called periods. Each period is given an alphabetic designation. During the 2012 data taking there were ten distinct periods which amounted to a combined luminosity of 19.5 ± 0.6 fb^{-1}. The luminosity for each data period is summarized in Table 6.2.

Period	Luminosity (pb^{-1})
A	707.237
B	5000.60
C	1220.05
D	3219.76
E	2355.36
G	1278.50
H	1378.68
I	1012.50
J	2516.94
L	839.218
Total	19528.845

Table 6.2: Dataset periods during 2012 data taking used in this analysis and their processed luminosity

6.2 Systematic Uncertainties

A systematic error in an experiment is an error introduced by the method of measurement. This is in contrast to a statistical error which arises due to the finite number of events in the analysis. In theory, statistical errors can be made arbitrarily small by collecting arbitrarily large amounts of data. Systematic errors, which are intrinsic to the measurement, cannot be made smaller by collecting more data. If a systematic error is found to be too large, more sophisticated methods must be used to reduce the error. In this analysis, the systematic errors are assessed on the Monte Carlo simulation, the unfolding procedure, and the background subtraction. In each case, the source of the systematic error is assessed by applying a change to the procedure and taking the difference from the nominal result as the symmetric error. These errors are added in quadrature with the statistical error to produce the final error band.

6.2.1 Trigger shape

As mentioned previously, the trigger choice presents the possibility of significantly biasing the result if care is not taken. This analysis could use either an isolated

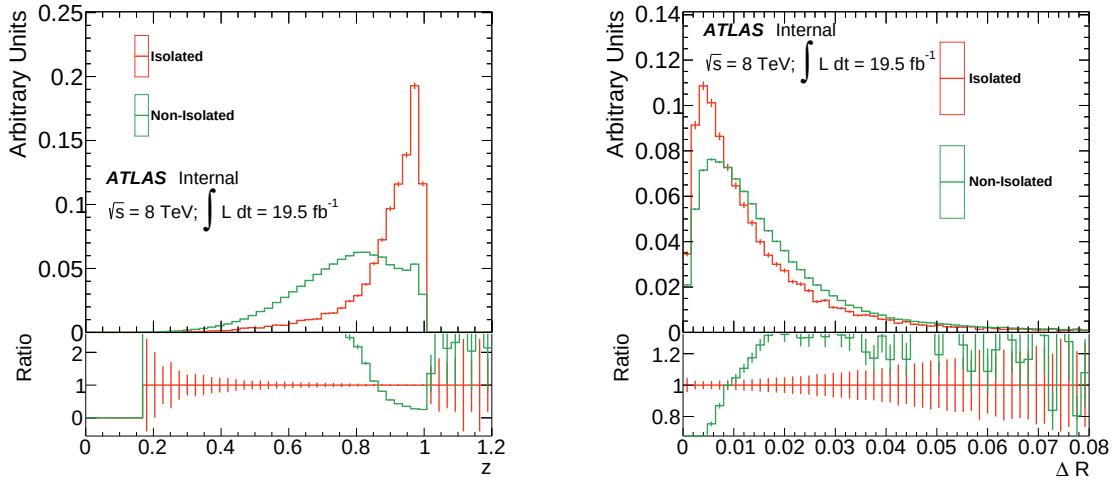

(a) z (b) ΔR

FIGURE 6.1: Comparison of isolated an non-isolated trigger for the variables of interest, z and ΔR.

muon trigger or the non-isolated trigger used by this analysis. In the former case, an isolation requirement is applied in order to increase the quality of the reconstructed muon. An isolation requirement ensures that there is no extraneous radiation in the vicinity of the reconstructed muon. This is counterproductive to the goal of this analysis. Figure 6.1 shoes the interest variables broken down by trigger choice and demonstrates the bias of using an isolated trigger.

6.2.2 Monte Carlo

The Monte Carlo samples are used in the response matrix estimation, as well as in comparing the shape to data. They contain the best description of the detector available. There are three main effects that can systematically change the estimate of the four vector of the track based observables: the scale of the track (i.e. a shift in the mean of the distribution), the resolution of the track and the efficiency to reconstruct the track (i.e. a shift in the width of the distribution). Muons are further complicated by the fact that they are the estimate of two detector subsystems, the inner detector and the muon spectrometer. Therefore there are systematic effects

associated with each of these contributions to the momentum measurement.

Previous measurements of the inclusive tracking efficiency for muons using the tag-and-probe method allow an efficiency scale factor to be applied to simulated data [4]. The uncertainty on the energy scale of the muon is found by varying the energy up and down depending on the p_T and η of the muon. As mentioned above, muons consist of an ID and an MS track, leading to resolution terms from each part of the detector. These are assessed separately and added in quadrature with the rest of the systematic errors.

Similar to muons, the track jets also have efficiency, scale, and resolution uncertainties. In order to assess their overall impact on substructure variables, the jet reconstruction is run on each variation. Previous measurements of the tracking efficiency allow tracks to be dropped randomly according to this distribution to assess the effect of missing a track during reconstruction [2]. This is the largest source of systematic error on the Monte Carlo samples used. Modifying the momentum scale of each track by 2% is shown to adequately cover this uncertainty [5]. The resolution (how well two tracks of slightly different momentum can be resolved) is found by varying the four vector of each track according to a gaussian with width 10% of the nominal momentum [60].

6.2.3 Unfolding

The largest source of uncertainty in unfolding is the estimation of the response matrix. This is assessed by estimating a new response matrix for each variation described in the previous section on Monte Carlo uncertainties. The resulting matrix is used to unfold the data, and the difference from the nominal result is added in quadrature with the remaining errors. In addition to this source of error, there are the statistical errors which are propagated through the method as part of the algorithm. The final source of error is on the method itself. This is assessed by filling a pseudo-truth dis-

tribution, folding it with the response matrix, and unfolding the result. The error is the difference between the unfolded pseudo-truth and the pseudo-truth distribution.

6.2.4 Background Subtraction

Correct estimation of the background depends on the empirical parameterization of the signal and background processes. In order to assess the effect that each component has on the overall estimate of the background, a different model is assumed for each component. The background subtraction technique is applied with this variation, and the difference from the nominal result is taken as the error for that part of the parametric model.

Resolution: The resolution of the lifetime distribution is modeled with a double-gaussian. This allows two widths to float as well as their relative normalization to better capture the distribution observed in data. In order to assess the impact of this choice, a single gaussian is used.

Combinatoric Mass: The combinatoric component of the mass background is modeled as the sum of an exponential term and a first degree polynomial. The effect of this choice is assessed by separately making the exponential term a constant, and varying the degree of the polynomial between one and three.

Mismeasured L_{xy} background: There is a fraction of events whose L_{xy} values are mismeasured. This is parametrized by symmetric exponential centered at $c\tau = 0$. The choice of this parameterization is assessed by restricting the exponential to be one-sided for negative lifetimes.

Crystal Ball parameters: The Crystal Ball function (equation 5.11) models radiative losses through asymmetric tails in the gaussian distribution. The parameters α and n control the strength of this effect. The α parameter is set to $\alpha = 1$ from its nominal value of $\alpha = 10$. The n parameter is set to $n = 5$ from its nominal value of $n = 1$.

6.3 Results

This analysis produces three distributions: the inclusive distribution of signal and background (Figures 6.3b and 6.3d), the background subtracted detector level distribution, and the unfolded distributions (Figures 6.4a and 6.4b). The background subtracted distribution is compared to Pythia's prediction which also has event reconstruction applied (Figures 6.3a and 6.3c). The inclusive distributions and the unfolded distributions are presented on their own.

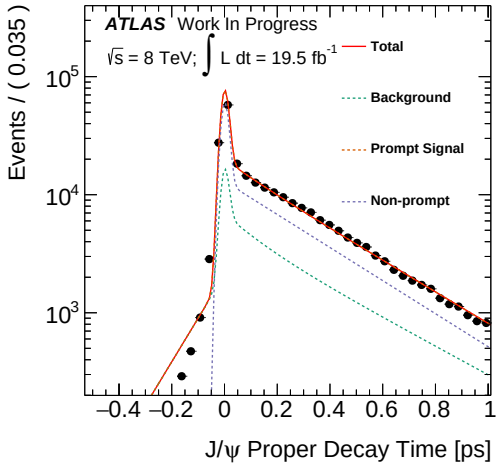

(a) Resolution

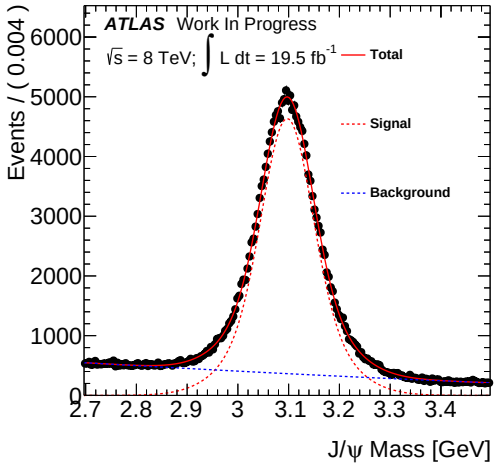

(b) Combinatoric Mass

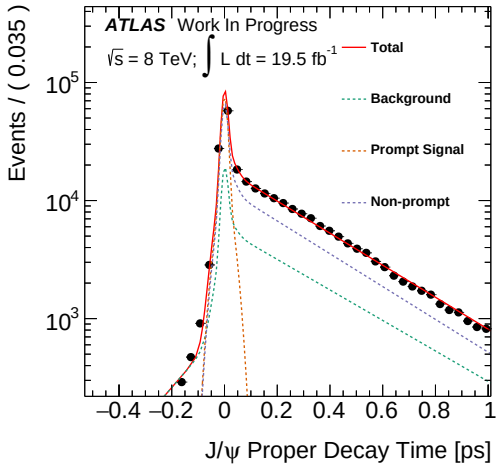

(c) Mismeasured L_{xy}

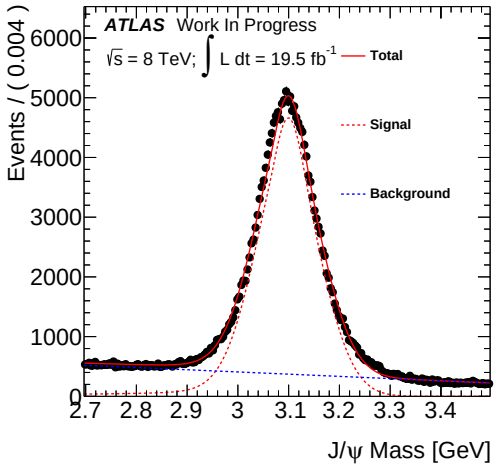

(d) Crystal Ball

FIGURE 6.2: Fit variations for each source of parameterization in the ML fit. In 6.2a the resolution function is switched with a gaussian. In 6.2b the mass background polynomial is varied. In 6.2c the symmetric lifetime component is made asymmetric. In 6.2d the Crystal Ball parameters that are fixed are varied.

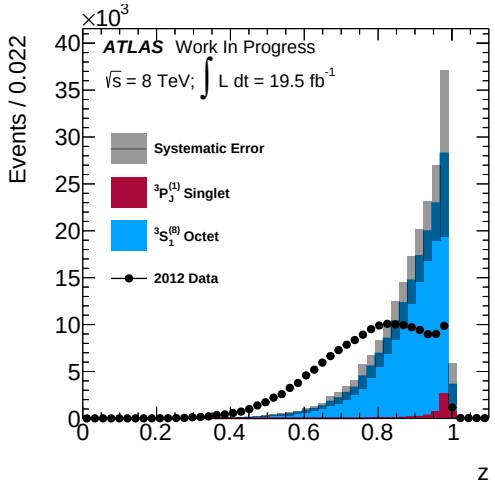

(a) Signal vs Pythia 8, z

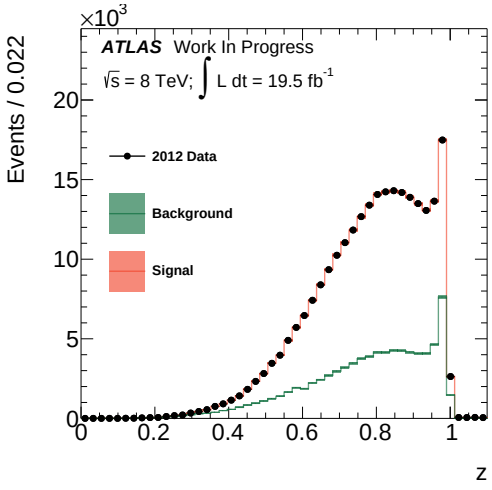

(b) Signal and background vs data, z

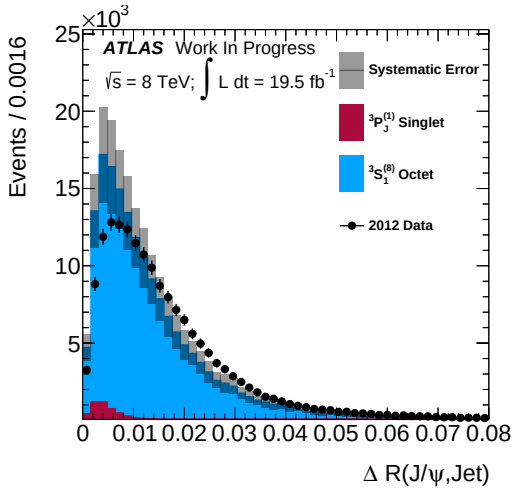

(c) Signal vs Pythia 8, ΔR

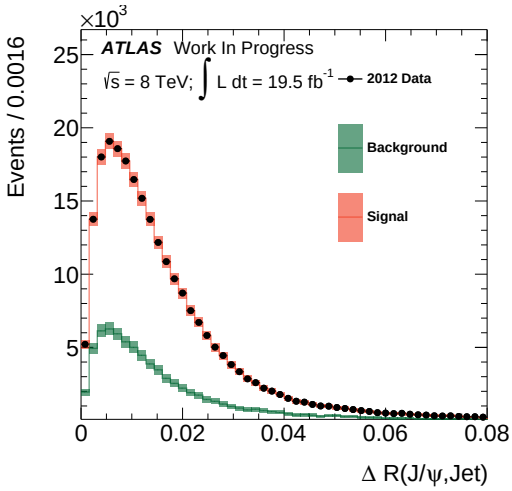

(d) Signal and background vs data, ΔR

FIGURE 6.3: In 6.3a and 6.3c Pythia's prediction compared to subtracted data for z and ΔR observables. The stack shows each component of prompt J/ψ production in Pythia. The grey error band is the quadrature sum of all systematic error sources across all MC samples. The dominant components are ${}^3P_J^{(1)}$ and ${}^3S_1^{(8)}$ due to the relative size of their cross sections based on the default parameters. In 6.3b and 6.3d the estimated signal and background components estimated from sPlot. The signal is added to the background to show closure with the observed data. Error bars are the statistical errors on the method.

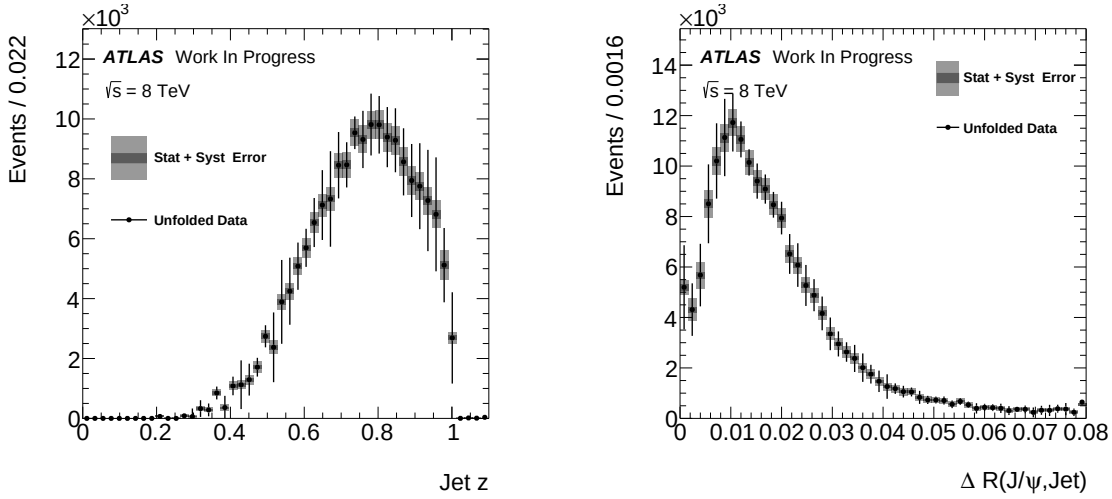

(a) z (b) ΔR

FIGURE 6.4: Unfolded signal distributions for z and ΔR observables. The shaded error band is the statistical (dark grey) and fit systematic (light grey). The error lines represent the quadrature sum of all error sources.

7

Conclusion

7.1 Discussion

This analysis has identified two variables for describing the production of J/ψ particles in hadronic collisions that have previously been poorly explored and can discriminate between models of J/ψ production. The ΔR distribution in Figure 6.3c shows that the data peaks in a slightly different place and has a longer tail than the combination of singlet and octet components provided by Pythia. Cross-checks of the muon p_T in data compared to Monte Carlo indicate that this effect may be due to the asymmetry in muon momentum due to the trigger requirement of one high momentum muon. The momentum fraction z (Figure 6.3a) has the most significant disagreement between the Pythia prediction and the observed data. The data seems to indicate that more momentum is carried by the jet than the J/ψ candidate (mean z before unfolding is $z \approx 0.7$, Pythia predicts $z \approx 0.9$).

The momentum fraction z directly probes the parton shower splitting leading up to the production of the J/ψ. Pythia models this process by allowing the $c\bar{c}$ state to radiate gluons until the state falls below a threshold at which point it emits as soft gluon and produces a J/ψ. The fact that the splitting function used is

$q \to qg$ leads to a z distribution that is sharply peaked at $z \simeq 1$. If instead, the J/ψ is produced during the fragmentation of an energetic gluon, the proper splitting function is $g \to gg$ until the gluon reaches an energy favorable for J/ψ production. This would influence the z distribution, causing it to peak at lower values of z as observed in the data. A recent measurement at the LHCb [6] of the momentum fraction, z at $|\eta| > 2.5$ and $\sqrt{s} = 13$ TeV shows a similar discrepancy between Pythia's description and the observed data. A recent analysis of the data [18] supports the gluon fragmentation interpretation of the data. If this is borne out by further analysis of the unfolded data presented in this work, a solution to the polarization puzzle may be found by examining the surrounding radiation in which J/ψ production is embedded.

The shape of the data and the differences between how the J/ψ is produced in the Fragmenting Jet Function (FJF) framework compared to Pythia suggest that modifying Pythia's treatment of the octet state shower may reduce disagreement between the data and the simulation. Pythia is the only general purpose Monte Carlo generator currently available that produces J/ψ using the NRQCD description of J/ψ production. This work indicates the need for more robust Monte Carlo simulations which better describe J/ψ production in hadronic collisions. Work has been done to implement the partonic cross sections for NRQCD quarkonium states in Sherpa by the author of this thesis. If this work is published, Sherpa may provide a valuable cross-check to Pythia's prediction. In addition, Sherpa is well placed to modify its treatment of the parton shower of the quarkonium state from the outset.

This work provides new observables that may constrain the predictions from NRQCD in interesting ways. It may be possible to use the z distribution to extract new LDMEs and subsequently compare to the p_T spectrum (or vice versa). In the original incarnation of this work, other substructure variables[1] were shown to dis-

[1] N-subjettiness moments and their ratios [61].

criminate between the singlet and octet processes as simulated by Pythia. It may be possible to extend this work to include those and other substructure variables in a way that further illuminates the exact production mechanism. In addition, the J/ψ system is used extensively in heavy ion collisions as a probe of the quark-gluon plasma produced in those interactions. Having a new understanding of how the quarkonium bound state is produced may require reinterpreting many results that extend beyond J/ψ production in hadron collisions.

In closing, this work demonstrates the need to study the hadronic environment that a quarkonium state is embedded in. It is the first measurement of ultra-high p_T J/ψ particles and has demonstrated techniques for robust background subtraction and the removal of non-linear detector effects. The resulting data will be immediately useful to theorists in further understanding how J/ψ particles are produced in hadron collisions. Finally, this work may provide the first hints at a way to reinterpret J/ψ production so that the spin-alignment problem, or polarization puzzle, can be solved definitively.

Bibliography

[1] G. Aad et al. "ATLAS pixel detector electronics and sensors". In: *JINST* 3 (2008), P07007. DOI: 10.1088/1748-0221/3/07/P07007.

[2] G. Aad et al. "Charged-particle multiplicities in pp interactions measured with the ATLAS detector at the LHC". In: *New J. Phys.* 13 (2011), p. 053033. DOI: 10.1088/1367-2630/13/5/053033. arXiv: 1012.5104 [hep-ex].

[3] Georges Aad et al. "Measurement of jet charge in dijet events from $\sqrt{s}$=8TeV pp collisions with the ATLAS detector". In: *Phys. Rev.* D93.5 (2016), p. 052003. DOI: 10.1103/PhysRevD.93.052003. arXiv: 1509.05190 [hep-ex].

[4] Georges Aad et al. "Measurement of the muon reconstruction performance of the ATLAS detector using 2011 and 2012 LHC proton–proton collision data". In: *Eur.Phys.J.* C74.11 (2014), p. 3130. DOI: 10.1140/epjc/s10052-014-3130-x. arXiv: 1407.3935 [hep-ex].

[5] Georges Aad et al. "Measurement of the Z/γ^* boson transverse momentum distribution in pp collisions at $\sqrt{s} = 7$ TeV with the ATLAS detector". In: *JHEP* 09 (2014), p. 145. DOI: 10.1007/JHEP09(2014)145. arXiv: 1406.3660 [hep-ex].

[6] Roel Aaij et al. "Study of J/ψ production in jets". In: (2017). arXiv: 1701.05116 [hep-ex].

[7] et al. Abe F. "J/ψ and $\psi(2S)$ Production in $p\bar{p}$ Collisions at $\sqrt{s} = 1.8$ TeV". In: *Phys. Rev. Lett.* 79 (4 1997), pp. 572–577. DOI: 10.1103/PhysRevLett.79.572. URL: http://link.aps.org/doi/10.1103/PhysRevLett.79.572.

[8] F. Abe et al. "Inclusive J/ψ, $\psi(2S)$ and b quark production in $\bar{p}p$ collisions at $\sqrt{s} = 1.8$ TeV". In: *Phys. Rev. Lett.* 69 (1992), pp. 3704–3708. DOI: 10.1103/PhysRevLett.69.3704.

[9] T. Affolder et al. "Measurement of J/ψ and $\psi(2S)$ Polarization in $p\bar{p}$ Collisions at $\sqrt{s} = 1.8$ TeV". In: *Phys. Rev. Lett.* 85 (14 2000), pp. 2886–2891. DOI: 10.1103/PhysRevLett.85.2886. URL: http://link.aps.org/doi/10.1103/PhysRevLett.85.2886.

[10] *Alignment of the ATLAS Inner Detector Tracking System with 2010 LHC proton-proton collisions at $\sqrt{s} = 7$ TeV*. Tech. rep. ATLAS-CONF-2011-012. Geneva: CERN, Mar. 2011. URL: https://cds.cern.ch/record/1334582.

[11] A. Altheimer et al. "Boosted objects and jet substructure at the LHC. Report of BOOST2012, held at IFIC Valencia, 23rd-27th of July 2012". In: *Eur. Phys. J.* C74.3 (2014), p. 2792. DOI: 10.1140/epjc/s10052-014-2792-8. arXiv: 1311.2708 [hep-ex].

[12] A Armbruster et al. *Practical considerations for unfolding.* Tech. rep. ATL-COM-PHYS-2014-277. Geneva: CERN, Apr. 2014. URL: https://cds.cern.ch/record/1694351.

[13] X. Artru, G. B. Yodh, and G. Mennessier. "Practical theory of the multilayered transition radiation detector". In: *Phys. Rev. D* 12 (5 Sept. 1975), pp. 1289–1306. DOI: 10.1103/PhysRevD.12.1289. URL: http://link.aps.org/doi/10.1103/PhysRevD.12.1289.

[14] J. J. Aubert et al. "Experimental Observation of a Heavy Particle J". In: *Phys. Rev. Lett.* 33 (23 1974), pp. 1404–1406. DOI: 10.1103/PhysRevLett.33.1404. URL: http://link.aps.org/doi/10.1103/PhysRevLett.33.1404.

[15] J. -E. et al. Augustin. "Discovery of a Narrow Resonance in e^+e^- Annihilation". In: *Phys. Rev. Lett.* 33 (23 1974), pp. 1406–1408. DOI: 10.1103/PhysRevLett.33.1406. URL: http://link.aps.org/doi/10.1103/PhysRevLett.33.1406.

[16] R. Baier and R. Ruckl. "Hadronic Collisions: A Quarkonium Factory". In: *Z. Phys.* C19 (1983), p. 251. DOI: 10.1007/BF01572254.

[17] Reggie Bain et al. "Analytic and Monte Carlo Studies of Jets with Heavy Mesons and Quarkonia". In: *JHEP* 06 (2016), p. 121. DOI: 10.1007/JHEP06(2016)121. arXiv: 1603.06981 [hep-ph].

[18] Reggie Bain et al. "NRQCD Confronts LHCb Data on Quarkonium Production within Jets". In: (2017). arXiv: 1702.05525 [hep-ph].

[19] Roger J. Barlow. "Extended maximum likelihood". In: *Nucl. Instrum. Meth.* A297 (1990), pp. 496–506. DOI: 10.1016/0168-9002(90)91334-8.

[20] Martin Beneke and Michael Kramer. "Direct J/ψ and ψ' polarization and cross sections at the Fermilab Tevatron". In: *Phys. Rev. D* 55 (9 1997), R5269–R5272. DOI: 10.1103/PhysRevD.55.R5269. URL: http://link.aps.org/doi/10.1103/PhysRevD.55.R5269.

[21] Geoffrey T. Bodwin, Eric Braaten, and G. Peter Lepage. "Rigorous QCD analysis of inclusive annihilation and production of heavy quarkonium". In: *Phys. Rev.* D51 (1995). [Erratum: Phys. Rev.D55,5853(1997)], pp. 1125–1171. DOI: 10.1103/PhysRevD.55.5853,10.1103/PhysRevD.51.1125. arXiv: hep-ph/9407339 [hep-ph].

[22] Bill Bryson. *A short history of nearly everything.* 1st ed. New York: Broadway Books, 2003.

[23] Mathias Butenschoen and Bernd A. Kniehl. "Next-to-leading-order tests of NRQCD factorization with J/ψ yield and polarization". In: *Mod. Phys. Lett.* A28 (2013), p. 1350027. DOI: 10.1142/S0217732313500272. arXiv: 1212.2037.

[24] Matteo Cacciari, Gavin P. Salam, and Gregory Soyez. "The anti- k t jet clustering algorithm". In: *Journal of High Energy Physics* 2008.04 (2008), p. 063. URL: http://stacks.iop.org/1126-6708/2008/i=04/a=063.

[25] Kuang-Ta Chao et al. "J/ψ Polarization at Hadron Colliders in Nonrelativistic QCD". In: *Phys.Rev.Lett.* 108 (2012), p. 242004. DOI: 10.1103/PhysRevLett.108.242004. arXiv: 1201.2675 [hep-ph].

[26] The ATLAS Collaboration et al. "The ATLAS Experiment at the CERN Large Hadron Collider". In: *Journal of Instrumentation* 3.08 (2008), S08003. URL: http://stacks.iop.org/1748-0221/3/i=08/a=S08003.

[27] The ATLAS TRT collaboration et al. "The ATLAS TRT Barrel Detector". In: *Journal of Instrumentation* 3.02 (2008), P02014. URL: http://stacks.iop.org/1748-0221/3/i=02/a=P02014.

[28] T. Cornelissen et al. "The new ATLAS track reconstruction (NEWT)". In: *J. Phys. Conf. Ser.* 119 (2008), p. 032014. DOI: 10.1088/1742-6596/119/3/032014.

[29] G. Cowan. *Statistical data analysis*. 1998.

[30] R. Keith Ellis, W. James Stirling, and B. R. Webber. "QCD and collider physics". In: *Camb. Monogr. Part. Phys. Nucl. Phys. Cosmol.* 8 (1996), pp. 1–435.

[31] Lyndon Evans and Philip Bryant. "LHC Machine". In: *Journal of Instrumentation* 3.08 (2008), S08001. URL: http://stacks.iop.org/1748-0221/3/i=08/a=S08001.

[32] Pietro Faccioli et al. "Quarkonium production in the LHC era: a polarized perspective". In: *Phys. Lett.* B736 (2014), pp. 98–109. DOI: 10.1016/j.physletb.2014.07.006. arXiv: 1403.3970 [hep-ph].

[33] R. P. Feynman, M. Kislinger, and F. Ravndal. "Current Matrix Elements from a Relativistic Quark Model". In: *Phys. Rev. D* 3 (11 1971), pp. 2706–2732. DOI: 10.1103/PhysRevD.3.2706. URL: http://link.aps.org/doi/10.1103/PhysRevD.3.2706.

[34] R. Fruhwirth. "Application of Kalman filtering to track and vertex fitting". In: *Nucl. Instrum. Meth.* A262 (1987), pp. 444–450. DOI: 10.1016/0168-9002(87)90887-4.

[35] Murray Gell-Mann. "Symmetries of Baryons and Mesons". In: *Phys. Rev.* 125 (3 1962), pp. 1067–1084. DOI: 10.1103/PhysRev.125.1067. URL: http://link.aps.org/doi/10.1103/PhysRev.125.1067.

[36] Bin Gong et al. "Polarization for Prompt J/ψ and ψ(2s) Production at the Tevatron and LHC". In: *Phys. Rev. Lett.* 110.4 (2013), p. 042002. DOI: 10.1103/PhysRevLett.110.042002. arXiv: 1205.6682 [hep-ph].

[37] David Griffiths. *Introduction to elementary particles*. 2008.

[38] David J. Gross and Frank Wilczek. "Asymptotically Free Gauge Theories. I". In: *Phys. Rev. D* 8 (10 1973), pp. 3633–3652. DOI: 10.1103/PhysRevD.8.3633. URL: http://link.aps.org/doi/10.1103/PhysRevD.8.3633.

[39] H. Haberzettl and J.P. Lansberg. "Possible solution of the J/ψ production puzzle". In: *Phys.Rev.Lett.* 100 (2008), p. 032006. DOI: 10.1103/PhysRevLett.100.032006. arXiv: 0709.3471 [hep-ph].

[40] Fred James and Matthias Winkler. "MINUIT User's Guide". In: (2004).

[41] Frederick James. *Statistical methods in experimental physics*. 2006.

[42] J.P. Lansberg and C. Lorce. "Reassessing the importance of the colour-singlet contributions to direct $J/\psi+W$ production at the LHC and the Tevatron". In: *Phys.Lett.* B726 (2013), pp. 218–222. DOI: 10.1016/j.physletb.2013.07.059. arXiv: 1303.5327 [hep-ph].

[43] Phillipe Lebrun. *Interim Summary Report on the analysis of the 19 September 2008 incident at the LHC*. Available at https://edms5.cern.ch/document/973073/1.

[44] Yan-Qing Ma, Kai Wang, and Kuang-Ta Chao. "$J/\psi(\psi')$ production at the Tevatron and LHC at $\mathcal{O}(\alpha_s^4 v^4)$ in nonrelativistic QCD". In: *Phys.Rev.Lett.* 106 (2011), p. 042002. DOI: 10.1103/PhysRevLett.106.042002. arXiv: 1009.3655 [hep-ph].

[45] Narai Lorenzo Martinez and Andrew Beddall. *TRT Definitions of common quantities*. Available at https://twiki.cern.ch/twiki/bin/viewauth/Atlas/TrtSoftwareDefinitions.

[46] *Measurement of the differential cross-sections of prompt and non-prompt production of J/ψ and $\psi(2S)$ in pp collisions at $\sqrt{s} = 7$ and 8 TeV with the ATLAS detector*. Tech. rep. ATLAS-CONF-2015-024. Geneva: CERN, July 2015.

[47] K. A. Olive et al. "Review of Particle Physics". In: *Chin. Phys.* C38 (2014), p. 090001. DOI: 10.1088/1674-1137/38/9/090001.

[48] Michael E. Peskin and Daniel V. Schroeder. *An Introduction to quantum field theory*. 1995. ISBN: 9780201503975, 0201503972. URL: http://www.slac.stanford.edu/spires/find/books/www?cl=QC174.45:P4.

[49] A Picazio. *A Measurement of the ATLAS Di-Muon Trigger Efficiency in Proton-Proton Collision at $\sqrt{s} = 7TeV$*. Tech. rep. ATL-DAQ-PROC-2012-002. Geneva: CERN, Jan. 2012. URL: https://cds.cern.ch/record/1419765.

[50] Muriel Pivk and Francois R. Le Diberder. "SPlot: A Statistical tool to unfold data distributions". In: *Nucl. Instrum. Meth.* A555 (2005), pp. 356–369. DOI: 10.1016/j.nima.2005.08.106. arXiv: physics/0402083 [physics.data-an].

[51] H. David Politzer. "Reliable Perturbative Results for Strong Interactions?" In: *Phys. Rev. Lett.* 30 (26 June 1973), pp. 1346–1349. DOI: 10.1103/PhysRevLett.30.1346. URL: http://link.aps.org/doi/10.1103/PhysRevLett.30.1346.

[52] Massimiliano Procura and Iain W. Stewart. "Quark Fragmentation within an Identified Jet". In: *Phys. Rev.* D81 (2010). [Erratum: Phys. Rev.D83,039902(2011)], p. 074009. DOI: 10.1103/PhysRevD.81.074009,10.1103/PhysRevD.83.039902. arXiv: 0911.4980 [hep-ph].

[53] Daniel Richter. "Energy Loss Measurements with the ATLAS Transition Radiation Tracker Using Test Beam Data". PhD thesis. Berlin: Humboldt Universitat zu Berlin, Jan. 2008.

[54] Anatoli Romaniouk et al. *Performance of the ATLAS Transition Radiation Tracker in Run 1 of the LHC: tracker properties*. Tech. rep. ATL-COM-INDET-2015-041. Geneva: CERN, June 2015. URL: https://cds.cern.ch/record/2021497.

[55] Russ Rowlett. *Unites of Measurement*. Available at http://www.unc.edu/~rowlett/units/index.html.

[56] Gavin P. Salam. "Towards Jetography". In: *Eur.Phys.J.* C67 (2010), pp. 637–686. DOI: 10.1140/epjc/s10052-010-1314-6. arXiv: 0906.1833 [hep-ph].

[57] A Salzburger. *The ATLAS Track Extrapolation Package*. Tech. rep. ATL-SOFT-PUB-2007-005. ATL-COM-SOFT-2007-010. Geneva: CERN, June 2007. URL: https://cds.cern.ch/record/1038100.

[58] Torbjorn Sjostrand, Stephen Mrenna, and Peter Z. Skands. "A Brief Introduction to PYTHIA 8.1". In: *Comput.Phys.Commun.* 178 (2008), pp. 852–867. DOI: 10.1016/j.cpc.2008.01.036. arXiv: 0710.3820 [hep-ph].

[59] Ewa Stanecka. "The ATLAS Inner Detector operation, data quality and tracking performance". In: arXiv:1303.3630 (Mar. 2013). Comments: Physics in Collision, Slovakia, 2012. URL: https://cds.cern.ch/record/1529765.

[60] *Study of alignment-related systematic effects on the ATLAS Inner Detector tracking*. Tech. rep. ATLAS-CONF-2012-141. Geneva: CERN, Oct. 2012. URL: https://cds.cern.ch/record/1483518.

[61] Jesse Thaler and Ken Van Tilburg. "Identifying Boosted Objects with N-subjettiness". In: *JHEP* 1103 (2011), p. 015. DOI: 10.1007/JHEP03(2011)015. arXiv: 1011.2268 [hep-ph].

[62] J.S. Townsend. *A Modern Approach to Quantum Mechanics*. International series in pure and applied physics. University Science Books, 2000. ISBN: 9781891389139. URL: https://books.google.com/books?id=3%5C_7uriPX028C.

[63] Wouter Verkerke and David P. Kirkby. "The RooFit toolkit for data modeling". In: *eConf* C0303241 (2003). [,186(2003)], MOLT007. arXiv: physics/0306116 [physics].

Biography

David Bjergaard was born on October 7, 1988, in Dickinson North Dakota. He earned his B.S. Physics with honors from Johns Hopkins University in 2011. He completed his Ph.D. in Physics at Duke University in 2017. He enjoys digital photography, brewing beer, and writing and maintaining open source software projects.